Numerical methods for axisymmetric equilibrium magnetic-fluid shapes

Dissertation
zur Erlangung des akademischen Grades

doctor rerum naturalium
(Dr.rer.nat.)

von **Dipl.-Math. Olga Lavrova**
geb. am 24. April 1979 in Minsk, Weißrussland

genehmigt durch die Fakultät für Mathematik
der Otto-von-Guericke-Universität Magdeburg

Gutachter:
    Prof. Dr. rer. nat. habil. Lutz Tobiska
    Prof. Dr. Viktor Polevikov
    Prof. Dr. rer. nat. habil. Eberhard Bänsch

eingereicht am: 01. März 2006

Verteidigung am: 03. Juli 2006

Zusammenfassung

Die vorliegende Arbeit leistet einen Beitrag zur Modellierung und Numerik freier Randwert-
probleme mit kapillaren Oberflächen. Die Problematik, die in der Arbeit betrachtet wird, ist die
Entwicklung, Untersuchung und Umsetzung numerischer Methoden zur Berechnung von in der
Gleichgewichtslage eingestellten axialsymmetrischen Oberflächenformen von Ferrofluiden unter
dem Einfluß eines stationären äußeren Magnetfeldes. Die entwickelten mathematischen Mod-
elle und numerischen Lösungsmethoden werden an konkreten Beispielen erprobt und verifiziert.
Als Beispiele betrachten wir die Oberflächenform eines Ferrofluidtropfens, die Oberflächenform
einer Luftblase in magnetischen Flüssigkeit und die Entstehung von einzelnen Stacheln auf der
Oberfläche einer horizontal unendlich ausgedehnten Ferrofluidschicht.

Die axialsymmetrischen statischen Oberflächenformen von Ferrofluiden lassen sich mathema-
tisch mit Hilfe eines gekoppelten Modells beschreiben. Das Modell besteht aus den Maxwell-
Gleichungen im Gebiet, das vom Ferrofluid und der umgebenden Luft eingenommen wird,
sowie der Young-Laplace-Gleichung auf der freien Grenzfläche. Die Grenzfläche zwischen Fer-
rofluid und Luft ist a-priori unbekannt und wird durch die Wechselwirkung von Magnetfeld und
Oberflächenform bestimmt. Es wird eine iterative teilproblem-orientierte Entkopplungsstrate-
gie angegeben, mit deren Hilfe das Gesamtproblem in ein magnetostatisches Problem in einem
Gebiet mit bekannter Grenzfläche und ein Oberflächenproblem mit bekanntem Magnetfeld zer-
legt wird. Die unterschiedliche Struktur der beiden Teilprobleme setzt verschiedene numerische
Approximationstechniken voraus.

Die entwickelte gekoppelte BEM-FEM-Strategie ist gut für die Untersuchung und Berech-
nung der Maxwell-Gleichungen geeignet. Aufgrund der Fernfeld-Randbedingung wird eine
Randelement-Methode (BEM) zur Diskretisierung der Maxwell-Gleichungen im Gebiet der
umgebenden Luft bevorzugt. Die Nichtlinearität des magnetostatischen Problem im Gebiet, das
vom Ferrofluid eingenommen wird, erfordert den Einsatz der Finite-Elemente-Methode (FEM).
Eine direkte Darstellung von Randintegralgleichungen und ihre Diskretisierung mit Hilfe der
Kollokationsmethode bieten ein geeignetes numerisches Verfahren zur Laplace-Gleichung an, die
die Maxwell-Gleichungen im Gebiet der umgebenden Luft in Form eines Potenzials beschreibt.
Die Konvergenz der stückweise konstanten Kollokation-Randelementmethode für exakt darge-
stelltem Rand sowie für Approximationen des Randes mit stückweise linearen Funktionen und
kubischen Splines wird untersucht. Die Kopplung der Kollokation-Randelementmethode im Ge-
biet der umgebenden Luft und der Galerkin-Finite-Elemente-Methode im Gebiet, das vom Fer-
rofluid eingenommen wird, wird programmtechnisch umgesetzt. Eine Approximation des Poten-
zials mittels stückweise linearer Funktionen und eine Approximation der Normalenableitung des
Potenzials auf der freien Grenzfläche mittels stückweise konstanter Funktionen werden verwen-
det. Die Untersuchung der numerischen Konvergenz des magnetostatischen Problems auf einer
Sphäre liefert die Abschätzung in der r-gewichteten L^2-Norm mit der Konvergenzrate h^2.
Die Anwendung von Finite-Elemente-Methoden erfordert die Konstruktion geeigneter Gitter.
Bei der Konstruktion der Gitter werden eine Delaunay-Technik sowie ein Verfahren der har-
monischen Erweiterung eingesetzt. Beide Vorgehensweisen werden im Hinblick auf die Qualität

der generierten Gitter sowie auf die Rechenzeiten zur Gittergenerierung verglichen.

Die Oberflächenformen werden bezüglich der Bogenlänge parametrisiert. Aufgrund der parametrischen Darstellung der freien Oberflächen wird die Young-Laplace-Gleichung in ein System von gewöhnlichen Differentialgleichungen umgeschrieben. Dieses System wird mit einer Finite-Differenzen-Methode oder mit der Spline-Methode diskretisiert. Beide Diskretisierungsmethoden führen auf algebraische Gleichungssysteme. Die Stabilität der iterativen Verfahren zur Lösung der algebraischen Gleichungssysteme wird im Hinsicht auf eine Unter-Relaxation-Technik numerisch untersucht.

Eine spezielle Methode zur Konstruktion der Gitter auf der Grenzfläche wird dargestellt. Die Methode basiert sich auf Daten für die Oberflächenkrümmung und erlaubt eine gute Approximation der Grenzflächeform, falls starke Deformationen auftreten.

Numerische Ergebnisse zum gekoppelten Modellproblem der Berechnung von in der Gleichgewichtslage eingestellten axialsymmetrischen Oberflächenformen von Ferrofluidtropfen unter dem Einfluß eines stationären Magnetfeldes werden gezeigt und diskutiert. Die numerischen Ergebnisse werden insbesondere mit elliptischen Oberflächenformen aus der Literatur verglichen, die analytisch durch Minimierung der Energie bestimmt wurden. Statische Oberflächenformen mit gespitzten Endpunkten werden bei der numerischen Testrechnungen beobachtet. Das führt auf wesentlichen Abweichungen von der elliptischen Form. Der Übergang zwischen Oberflächen mit abgerundeten Endpunkten und kegelförmigen Formen wird numerisch gezeigt. Die Oberflächenformen von Ferrofluidtropfen werden in einem breiten Bereich der Magnetfeldstärke numerisch berechnet. Aufgrund der Randelementmethode zur Diskretisierung des axialsymmetrischen Potenzialproblems treten Schwierigkeiten bei der numerischen Berechnung in der Nähe der Symmetrieachse auf.

Numerische Ergebnisse zum Modellproblem der Berechnung der Oberflächenform einer Luftblase in magnetischer Flüssigkeit unter dem Einfluß eines stationären äußen Magnetfeldes werden gezeigt und diskutiert. Das Verhalten eines Ferrofluidtropfens wird mit dem Verhalten einer Luftblase in magnetischer Flüssigkeit verglichen.

Numerische Ergebnisse zum Modellproblem der Berechnung einzelner Stachel auf der Oberfläche einer horizontal unendlich ausgedehnten Ferrofluidschicht werden gezeigt und diskutiert. Die Ergebnisse werden mit den mit der linearen Stabilitätsanalyse hergeleiteten theoretischen Aussagen verglichen. Die statische Oberflächenformen werden für verschiedene Werte der Magnetfeldstärke und für verschiedene Typen von Ferrofluiden numerisch berechnet. Die axialsymmetrischen numerischen Ergebnisse werden mit Ergebnissen für das dreidimensionalen Modell verglichen. Ein axialsymmetrisch einzelnes Obeflächenmuster, das sich von dem bei der Rosensweig-Instabilität bekanntem Muster unterscheidet, wird numerisch bestimmt.

Acknowledgement

Contents

Chapter 1

Introduction

Magnetic fluids are stable colloidal suspensions of ferromagnetic or ferrimagnetic nano-particles (of size 3-15 nm) in a carrier liquid (water, oil, bio-compatible liquid). On macroscopic level magnetic fluids can be considered as incompressible and nonconducting continuous media. Magnetic fluids are not found in nature and they were at first synthesised in the middle of the 1960th. For a detailed overview on magnetic fluids and their properties see [14, 15, 63].

The unique properties of magnetic fluids, namely the combination of their fluidity with strong interaction with magnetic field provides nowadays an increasing number of their technical applications. For a general overview on applications see [14, 15].

A special interest is the use of magnetic fluids with free surfaces, in particular, in mass-exchange apparatus, for hydraulic resistance reduction and heat transfer enhancement [14]. It gives rise to numerous investigations of shapes and stability control of magnetic fluid surfaces.

One of the classical problems in ferrohydrostatics is an equilibrium of a free magnetic fluid drop in an external magnetic field. The freely suspended magnetic fluid drop, initially held spheroidal by surface tension, elongates in the direction of the uniform applied magnetic field and takes stable equilibrium shapes. The same effect is presented for a dielectric drop subjected to a uniform electric field, see [9, 79]. A number of experimental [8, 10, 14, 18], theoretical [8, 14, 17, 18, 60, 71, 72] and numerical [9, 20, 48, 66, 67, 69, 79] studies are concerned with the problem on equilibrium magnetic-fluid drop shapes.

Theoretical investigations

There are different approaches for the theoretical description of a behaviour of a drop in a field [8, 14, 17, 72]. All solutions of the theoretical studies are approximative due to the assumption for the drop shape to be spheroidal. The theoretical approach presented in [8] is based on the minimisation of the magnetic energy and the interfacial energy in respect to the aspect ratio between major and minor spheroid semi-axes. In [14] the free surface equation is required to be satisfied only at the top and the equator of a spheroid. The drop behaviour is analysed by using a virial method in [17, 72]. The comparative analysis of all mentioned theoretical approaches, see [17], concludes that all theoretical studies yield identical results for small drop deformations. Moreover, the energy approach [8] and the virial technique [17, 72] give identical results for any field, despite the fact that the solutions of both methods have different analytical representations. Nevertheless, the authors in [8, 10] recognized the limitation of spheroidal approximation: the drop shapes they observed experimentally became conical at the drop tips in the region of large drop deformations. The experimental study in [10] has revealed that the magnetic fluid drop can be considered as a spheroid up to a length-to-width ratio equals to 7. Agreement between theory and experiment may be considered only qualitatively successful.

Hysteresis effect

At sufficiently large values of the magnetic permeability μ ($\mu > 20$) the drop deformation can exhibit hysteresis. Modestly deformed prolate drops jump to much more elongated shapes when the magnetic field increases above a threshold. These large elongations persist even when the magnetic field decreases below the critical value. For decreasing magnetic field a jump from the upper branch of solutions with large elongated shapes to the lower branch of solutions appear at the second threshold. A limited range of the magnetic field strength values exists (hysteretic regime), where two equilibrium configurations of a drop are allowed, one of which occurs upon increasing the strength of a magnetic field, another - upon its decrease.

The occurrence of the hysteresis effect was observed in the experimental measurements, where the deformation of agglomerate microdrops of colloidal ferromagnetics (2 to 20 μm) of high magnetic susceptibility was investigated [8]. The hysteresis was also predicted in theoretical studies [8, 14, 17].

Numerical investigations

Several attempts were made to model the problem on equilibrium drop surfaces numerically [9, 20, 48, 66, 67, 79].

One of the first works, where the equilibrium drop shapes were studied numerically, was made at the beginning of the 1980th by Miksis, see [48]. According to results of numerical calculations it was concluded that for the magnetic permeability μ exceeding some critical value there is a maximum value of drop deformation at which families of equilibrium shapes terminate. Such a conclusion was confirmed neither experimentally nor theoretically and was a consequence of numerical instability.

The time-dependent low-Reynolds-number problem for the drop deformation was studied in [67] by means of a boundary integral technique. In the work it is reported that for the permeability $\mu = 25$ it proved impossible to follow the jump to the upper branch of the deformation curve. A pointed tip was developed and the numerical scheme broke down. The hysteretic behaviour was not in general reproduced in numerical simulations, suggesting that the viscosity of the two fluids can play an important role.

In [79] a finite element method was applied to model the behaviour of the linear magnetisable fluid drop. Composite cylindrical/spherical coordinates were used for accurate calculation of drop shapes with strong elongated surfaces. It was reported that the hysteresis effect can occur only in a quite narrow range of values of μ. Such an observation indicated qualitative difference with the experimental results in [8]. To resolve this discrepancy their numerical analysis was extended to the case of nonlinear magnetisable fluids in [9]. The hysteresis effect was found numerically for $\mu = 41$ but quantitative comparison with experimental results was not presented. All shapes found numerically in [8] have rounded ends, whereas in the experiment [8] shapes close to conical were observed.

Equilibrium shapes of nonlinear magnetisable fluids were modeled numerically in [20] till length-to-width ratio equals 5. Numerical instability occurred for further drop elongations.

The method based on the minimisation of the energy with respect to the axisymmetric shape of the drop was applied in [66]. The dynamic problem was considered under assumption that the velocity field is potential. Numerically drop shapes for the permeability $\mu \in [1, 5]$ were resolved till length-to-width ratio equals 4. According to the experimental results in [14] for such parameters the drop shape is close to a spheroid.

It follows that all previously done numerical calculations of equilibrium drop shapes have run into troubles because of numerical instability in regions of strong shape elongations.

Conical interfaces

Several investigations were made to study appearance of conical interfaces as equilibrium shapes of a magnetic fluid drop [18, 44, 60, 69, 71].

It is known that the curvature of a cone is inversely proportional to the distance from the cone tip ρ. From a balance between magnetostatic and surface tension forces we can get that the magnetic pressure is also inversely proportional to ρ in a cone region. It allows to define the approximation for the magnetostatic potential and using Maxwell's equations inside and outside a cone to construct a dependence of a cone angle as a function of the fluid permeability, see [18, 60, 71]. At first such an idea to analyse the problem was presented in [71] for the case of a perfectly conducting drop ($\mu = \infty$). The authors in [18, 60] extended this analysis to the case of two fluids with arbitrary values of μ. An open question of such analysis is how a local conical solution may be joined with the rest of the shape of the drop.

In [69] a slender-body theory was used to determine the approximate static shape of a conically ended magnetic fluid drop. The governing equations were simplified using the assumption that width-to-length ratio of the drop shape is much smaller than one and neglecting the effect of the normal component of the magnetic field to the free surface. The model equations were reduced to an ordinary differential equation for the field intensity, coupled to an algebraic equation for the pressure balance at the interface.

A semi-analytical approach was applied in [44] to analyse static singular shapes of a fluid drop. A drop surface was approximated by matching a spheroid with two cones in a tip region of a relative size 10^{-4}. The resulting integral equations were solved numerically. The authors found that a stable drop with conical tips exists only above a threshold field and that such a drop is energetically favoured compared to the spheroidal shape at a sufficiently high field.

The analyses in [44, 69] are applicable to the case of large drop deformations and pointed ends, but are inappropriate for the case of rounded ends and small deformations.

All previously done numerical studies [9, 48, 67, 79], except theoretical approaches in [18, 60, 71] and semi-analytical investigations in [44, 69], could not resolve the structure of the solution in the neighbourhood of nearly pointed ends.

Structure of the thesis

A major goal of the thesis is to develop a numerical solution strategy for calculating axisymmetric equilibrium magnetic-fluid shapes subjected to a uniform applied magnetic field. The second important subject of the thesis is on the base of the developed numerical strategy to fulfil an accurate numerical modeling and simulation of problems on magnetic-fluid drop shapes, bubble configurations in a bulk of the magnetic fluid and on single peak formations on the surface of a magnetic-fluid layer.

In Chapter 2 we formulate the mathematical model on equilibrium magnetic-fluid shapes. In order to be specific in this Chapter and Chapters 3 and 4 we concentrate on the model problem of magnetic-fluid drop shapes in a uniform magnetic field. We make several assumptions for the model statement. We suppose that the magnetic fluid stays homogeneous under the influence of the magnetic field so that the concentration of the magnetic nanoparticles at the regions of high surface deformations is not significant higher than in the bulk of the fluid. We assume that the magnetic fluid is at rest so that a static model analysis is appropriate. The free surface is defined to stay axisymmetric in the field direction as it deforms with changing field strength. Our mathematical model excludes conical surface shapes with the curvature taking an infinite value.

The mathematical model is governed by a coupled system of Maxwell's equations for the magnetic field distribution and the Young-Laplace equation for the free surface shape.

Maxwell's equations are formulated in the domain with *a-priori* unknown fluid-air interface. Governing model equations for a full three dimensional case and its axisymmetric version are presented in Sections 2.1-2.2 and 2.3, respectively. An iterative decoupling strategy for a coupled system of nonlinear partial differential equations is formulated in Section 2.4. For the approximation of the separated subproblems (the magnetostatic problem and the free-surface problem) different numerical techniques are required.

An application of boundary and finite element methods to the magnetostatic problem is discussed in Chapter 3. To solve Maxwell's equations both inside and outside of the magnetic fluid we use the finite element method or a coupled strategy of boundary and finite element methods. A boundary element method is used in an unbounded air domain to fulfil the boundary condition for the magnetic field at infinity while with a finite element method we resolve the non-linearity of the magnetostatic equations inside a magnetic fluid. In Section 3.1 we present some common aspects about using a boundary element method for the solution of the Laplace equation in bounded and unbounded domains. Direct formulation of boundary integral equations is given for 3D and axisymmetric problems. A special attention is made to the boundary condition at infinity. The collocation method is applied for the discretisation of the integral equations. Kernel functions approximation and their asymptotic behaviour for axisymmetric problems are discussed. The boundary element method for the magnetostatic problem formulation inside of the linear magnetisable fluid and outside it is described in Section 3.2. We apply a piecewise-constant collocation for the magnetostatic problem on a sphere. We show how an inexact representation of the boundary influences the convergence of the collocation method. Numerical convergence for the problem with the exact representation of the boundary and its piecewise linear and cubic spline approximations are analysed. Grid configurations with uniform and nonuniform point distribution on the boundary are considered.

   Section 3.3 presents the finite-element discretisation for the magnetostatic problem with nonlinear fluid properties. The solvability of the nonlinear problem in weighted Sobolev spaces is studied. In Section 3.4 we apply the coupling of the collocation boundary element method in the exterior air domain and the Galerkin finite element method in the interior fluid domain. Piecewise linears for the potential and piecewise constants for the normal derivative of the potential on the free boundary are taken. The numerical convergence of the second order for r-weighted L^2-norm is shown for the magnetostatic problem on a sphere. An application of finite element methods requires a grid construction in a computational domain. In Section 3.5 two methods for the grid generation, a harmonic extension approach and a Delaunay technique, are presented. They are compared with respect to the quality of the generated grids and the computational efficiency of the underlying algorithms in application to the coupled magnetostatic and free surface problem. We found that the harmonic extension approach is computationally more effective than the Delaunay approach. But the loss in quality of the grid, generated by the harmonic extension approach in contrast to those by the Delaunay technique, can be crucial for its further application for the numerical solution of differential equations.

In Chapter 4 a special approach to handle the balance equation on the fluid-air interface [56, 58] is presented. Surface shapes are parametrised with respect to the arc length. For the discretisation of the equations a finite-difference method in Section 4.2 and a spline-method in Section 4.3 are presented. A special algorithm of the surface grid generation [54], based on the information about a surface curvature, allows us to produce an accurate approximation for the shapes with high deformations. Section 4.4 contains a test example, intended to examine the influence of a successive under-relaxation technique to the stability of the iterative algorithms resulting from the finite-difference and the spline schemes. We observed that the spline scheme

shows a better stability property. Additionally we found that for axisymmetric problems at least one boundary condition should necessarily be specified at the "non-axis" end point. Otherwise, the scheme shows no convergence at all.

Chapter 5 contains numerical results for the problem on axisymmetric equilibrium surface shapes of a magnetic-fluid drop under the influence of an external uniform magnetic field. A comparison of numerical results with spheroidal equilibrium shapes, predicted theoretically in [8], is presented. We found that the difference between theory and numerics lies within 1 % for the lower branch of the solution, but shows more that 15 % for the upper branch of the hysteretic curve. Equilibrium shapes with pointed ends were resolved numerically, resulting in the strong deviation from spheroidal shapes of the theory. The transition from shapes with rounded ends to shapes close to conical were for the first time realised numerically. We measured the cone angle of the numerically obtained conical shapes and compared it with the theoretical predictions in [18, 60]. Equilibrium drop shapes were resolved in a wide range of field intensities till the saturation of magnetic fluids. We found that in the region of strong fields, where no surface changes are presented, the computational process becomes unstable. Numerical difficulties near the symmetry axis, due to the boundary-element discretisation of the axisymmetric potential problem, become pronounced in the region of strong fields. Adaptive integration methods, suggested in [50], did not improve the accuracy of the numerical results. According to our calculations, we report an advantage of using a finite element technique over the boundary element discretisation in application to the axisymmetric magnetostatic problem in the region of strong fields.

In Chapter 6 we consider the problem on axisymmetric equilibrium surface shape of a bubble inside a magnetic-fluid layer under the influence of an external uniform magnetic field. Governing model equations, numerical strategy and numerical results are presented. The behaviour of magnetic-fluid drops and bubbles in the magnetic fluid is compared.

In Chapter 7 we consider the problem on axisymmetric equilibrium surface shape of a magnetic-fluid layer under the influence of an external uniform magnetic field. Governing model equations, numerical strategy and numerical results are presented. Numerical results are compared with theoretical ones obtained by the linear stability analysis in [63]. Equilibrium surfaces are calculated for different magnetic intensities and magnetic-fluid parameters. A comparison of axisymmetric and three-dimensional numerical results is discussed. Section 7.4 contains numerical results on a solitary surface configurations of a magnetic-fluid layer. It is a novel effect of the Rosensweig instability, recently observed experimentally in [61].

Finally in Chapter 8 we summarise the main results of the thesis.

Chapter 2

Mathematical model

We consider an isolated magnetic fluid drop of a prescribed volume surrounded by a nonmagnetic gas media (air) under the action of a uniform magnetic field. The field intensity vector $\mathbf{H_0}$ applied at infinity is assumed to be parallel to the z-axis, i.e. $\mathbf{H_0} = (0, 0, -H_0)$. Away from the magnetic fluid the field is uniform. Close to the fluid the magnetic field uniformity is disturbed due to a self-field, created by the fluid itself.

We are interested in the equilibrium shapes of the free surface between the magnetic fluid and the surrounding air. The equilibrium shapes are investigated for different values of the applied magnetic field H_0 and for fluids with different magnetic properties.

The free boundary value problem is governed by a coupled system of Maxwell's equations for the magnetic field distribution and Young-Laplace equation for the free surface shape. Maxwell's equations are formulated in the domain with *a-priori* unknown fluid-air interface. On the other side, the interface position is determined by the solution of Maxwell's equations. The mathematical model of this problem has a coupled nonlinear statement.

We remark that all equations of this and the following Chapters are expressed in SI-units.

2.1 Maxwell's equations for magnetostatic field

Let D_1 be a domain externally bounded by a closed surface S and D_2 be a domain internally bounded by the same surface which satisfy $D = \bar{D}_1 \cup \bar{D}_2 = \mathrm{I\!R}^3$ and $D_1 \cap D_2 = \emptyset$. We assume that the domain D_1 is filled with a magnetic fluid, whereas D_2 is an air domain. In the absence of the applied field interfacial tension holds the drop spherical. Initially we define the fluid domain D_1 as a sphere with a center, placed at the origin of the coordinate system. The geometry of a computational domain is presented in Fig. 2.1.

Maxwell's equations for a nonconducting media in the stationary case are given by, see [63]

$$\nabla \times \mathbf{H} = \mathbf{0}, \quad \nabla \cdot \mathbf{B} = 0 \quad \text{in } D, \tag{2.1}$$

where $\mathbf{H}$ and $\mathbf{B}$ denote the magnetic field strength and the magnetic induction, respectively. The magnetic induction $\mathbf{B}$ is related to the magnetic field $\mathbf{H}$ and the magnetisation vector $\mathbf{M}$ by the expression

$$\mathbf{B} = \mu_0(\mathbf{H} + \mathbf{M}), \tag{2.2}$$

where μ_0 is the permeability constant. The magnetisation vector $\mathbf{M}$ of a magnetic fluid is parallel to the magnetic field $\mathbf{H}$, see [63]

$$\mathbf{M} = M(H)\frac{\mathbf{H}}{H}, \tag{2.3}$$
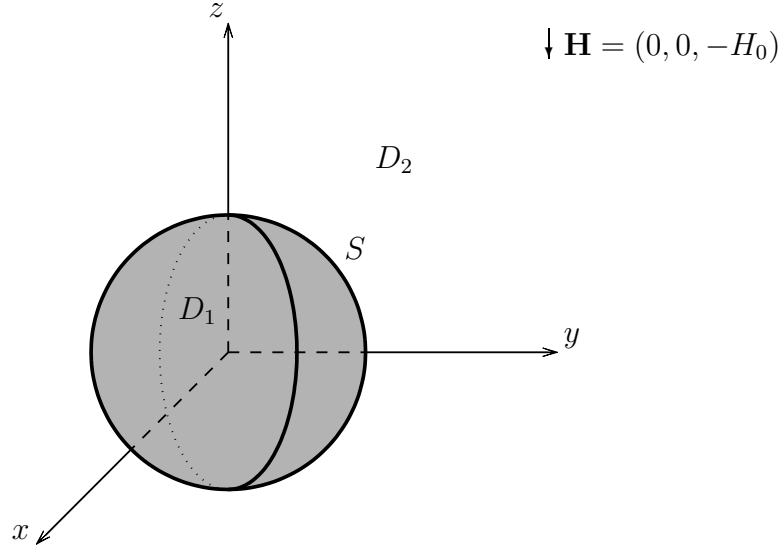
Figure 2.1: The computational domain at the moment when the magnetic field is to be applied.

where $M(H)$ is the magnetisation law and $H = |\mathbf{H}|$. The magnetisation in the air equals 0.

Due to the fact that magnetic fluids are non-conducting, there is no current flow such that $\nabla \times \mathbf{H} = \mathbf{0}$. The magnetic field $\mathbf{H}$ can be expressed in terms of a magnetostatic potential u by the expression $\mathbf{H} = -\nabla u$ both inside and outside the fluid domain. From equations (2.1)–(2.3) it follows that the magnetostatic potential satisfies the equations

$$-\nabla \cdot (\mu_i(|\nabla u_i|)\nabla u_i) = 0, \quad \text{in } D_i; \qquad \begin{aligned} \mu_1 &= \mu_0\left(1 + \frac{M(|\nabla u_1|)}{|\nabla u_1|}\right) && \text{in } D_1, \\ \mu_2 &= \mu_0 && \text{in } D_2, \end{aligned} \qquad (2.4)$$

where the subscripts 1 and 2 denote variables in the fluid and the air domains, respectively. To complete the formulation of equations (2.4) we define a relation between M and H. The magnetisation M of the magnetic fluid can be presented by different magnetisation laws. In the region of weak magnetic fields when the magnetisation M is much smaller then the saturated magnetisation M_s the linear magnetisation law applies for a magnetic fluid

$$M(H) = \chi H, \qquad (2.5)$$

where χ denotes the magnetic susceptibility. Small concentrated magnetic fluids behaves as a paramagnetic medium and its magnetisation follows the Langevin equation, see [63]

$$M(H) = M_s P(\gamma H), \quad P(t) = \coth t - \frac{1}{t}, \quad \gamma = \frac{3\chi}{M_s}. \qquad (2.6)$$

Let us define boundary conditions for equations (2.4). The boundary conditions on the interface S between two media with different magnetic properties satisfy, see [63]

$$u_1 = u_2, \quad \mu_1\frac{\partial u_1}{\partial n} = \mu_2\frac{\partial u_2}{\partial n} \qquad \text{on } S, \qquad (2.7)$$

where n is a unit normal vector. Conditions (2.7) are the statement of the continuity of the tangential component of the magnetic field and of the normal component of the magnetic induction across the interface. Far from the drop the magnetic field approaches a vertically directed uniform field with the intensity H_0. It follows that we have a condition at infinity

$$\lim_{(x,y,z)\to\infty} (u_2 - H_0 z) = 0. \qquad (2.8)$$

The magnetostatic field inside and outside the magnetic fluid drop is described by equations (2.4) with boundary conditions (2.7) and (2.8) for the magnetisation, expressed in one of the form (2.5) or (2.6).

Remark 2.1.1 *We cancel a factor μ_0 in equations (2.4). It results that*

$$\mu_1 = 1 + \frac{M(|\nabla u_1|)}{|\nabla u_1|} \quad in \ D_1,$$

$$\mu_2 = 1 \quad\quad\quad\quad in \ D_2,$$

and as a consequence conditions (2.7) take form

$$u_1 = u_2, \quad \mu_1 \frac{\partial u_1}{\partial n} = \frac{\partial u_2}{\partial n} \quad\quad on \ S.$$

Remark 2.1.2 *In the air domain D_2 equation (2.4) corresponds to the Laplace equation and for the case of a linear magnetisation law ($\mu_1 = const$) also in the fluid domain D_1.*

In the numerical study of surface instabilities it would be desirable to restrict the computational domain to the region of the magnetic fluid. However, we do not know the boundary conditions for the magnetostatic potential at the interface. Thus we have to determine the potential inside and outside of the magnetic fluid region.

2.2 Young-Laplace equation for magnetic fluids

We consider an equilibrium surface S of an isolated magnetic fluid drop.

The magnetically augmented Young-Laplace equation for the isothermal magnetic fluid, which is at rest, see [14, 63], presents the balance equation on the free surface

$$p - p_0 = \sigma \mathcal{K} - \frac{\mu_0}{2} \left(M \frac{H_n}{H} \right)^2 \quad on \ S, \tag{2.9}$$

where p is the fluid pressure, $p_0 = const$ the external pressure, σ the surface tension coefficient, $\mathcal{K}$ the sum of principal curvatures, H_n the normal component of the magnetic field intensity H. Equation (2.9) is a balance of capillary and magnetostatic forces along the interface S between the magnetic fluid and the surrounding air. The balance equation (2.9) states that magnetic stresses on the interface deform the interface in the direction of the applied magnetic field, competing against capillary forces.

The fluid pressure p is defined from the Navier-Stokes equations. In the absence of the fluid motion ($\mathbf{u} \equiv \mathbf{0}$) the Navier-Stokes equations reduce to

$$\nabla p = -\rho g \mathbf{e}_z + \mu_0 M \nabla H,$$

where p is the sum of the hydrostatic and the fluid-magnetic pressure. Integrating the last equation we get

$$p = -\rho g z + \mu_0 \int_0^H M dH + p_1, \tag{2.10}$$

where p_1 is a constant reference pressure.

Equation (2.10) together with no-gravity assumption allow us to write the Young-Laplace (2.9) in the form

$$\sigma \mathcal{K} = \mu_0 \int_0^H M dH + \frac{\mu_0}{2} \left(M \frac{H_n}{H} \right)^2 + C \quad on \ S, \tag{2.11}$$

where $C = p_1 - p_0$ is the hydrostatic pressure difference.

2.3   Cylindrical coordinates

Let us assume that the domains D_1 and D_2 are invariant by rotation around the z-axis and generated by rotating two-dimensional meridian domains Ω_1 and Ω_2

$$D_1 = \{(r, \theta, z) \mid (r, z) \in \Omega_1, \ 0 \le \theta < 2\pi\}, \quad D_2 = \{(r, \theta, z) \mid (r, z) \in \Omega_2, \ 0 \le \theta < 2\pi\}.$$

Here (r, θ, z) denote cylindrical coordinates. The surface S is produced by rotating some plane contour Γ around z-axis.

Under assumption of the axial symmetry around z-axis and symmetry in respect to the plane $z = 0$ the three-dimensional computational domain, see Fig. 2.1, can be considered as two-dimensional in cylindrical coordinates (r, z), see Fig. 2.2.
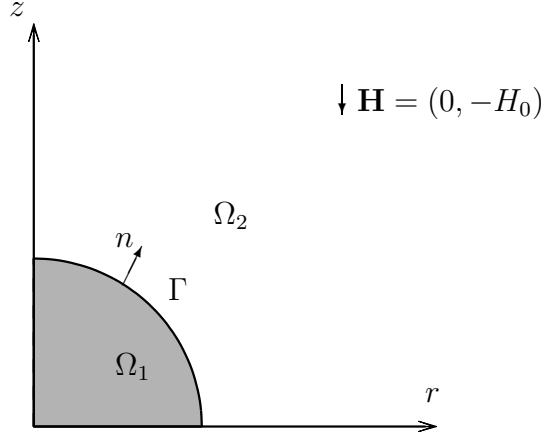
Figure 2.2: An initial computational domain in cylindrical coordinates.

We reformulate the model equations (2.4) and (2.11) and conditions (2.7), (2.8) in dimensionless variables using the cylindrical coordinates. We choose the radius R_0 of the initially spherical drop as a characteristic length and the strength H_0 as a characteristic field strength. Then we define

$$\tilde{r} = \frac{r}{R_0}, \ \tilde{z} = \frac{z}{R_0}, \ \tilde{H} = \frac{H}{H_0}; \quad \tilde{\mathcal{K}} = R_0 \mathcal{K}, \ \tilde{\nabla} = R_0 \nabla, \ \tilde{u} = \frac{u}{H_0 R_0},$$

where a tilde denotes dimensionless variables.

The governing equations take a dimensionless form for the magnetostatic problem (we drop the tildes for convenience)

$$-\nabla \cdot (\mu_i(|\nabla u_i|)\nabla u_i) = 0, \quad \text{in } \Omega_i; \quad
\begin{aligned}
\mu_1 &= 1 + \frac{M(H_0|\nabla u_1|)}{H_0|\nabla u_1|} & \text{in } \Omega_1, \\
\mu_2 &= 1 & \text{in } \Omega_2.
\end{aligned}
\qquad (2.12)$$

The gradient and divergence operators are in cylindrical coordinates under the axial symmetry assumption for the potential u. The boundary conditions (2.7) and (2.8) and the symmetry conditions in respect to the z-axis and the plane $z = 0$ are given by

$$u_1 = u_2, \quad \mu_1 \frac{\partial u_1}{\partial n} = \frac{\partial u_2}{\partial n} \qquad \text{on } \Gamma, \qquad (2.13)$$

$$\lim_{(r,z)\to\infty} (u_2 - z) = 0, \qquad (2.14)$$

$$\frac{\partial u_1}{\partial n} = 0, \quad \frac{\partial u_2}{\partial n} = 0 \quad \text{for } r = 0; \tag{2.15}$$

$$u_1 = 0, \quad u_2 = 0 \quad \text{for } z = 0. \tag{2.16}$$

Boundary conditions (2.16) follow from the symmetry requirement at the plane $z = 0$ and the asymptotic behaviour of the potential at infinity

$$\frac{\partial u}{\partial z} = 0 \quad \text{and} \quad \lim_{r \to \infty} u_2 = 0 \quad \text{for } z = 0.$$

The model is closed by the Young-Laplace equation in the dimensionless form

$$\frac{\sigma}{R_0} \mathcal{K} = \mu_0 H_0 \int\limits_0^H M(H_0 H) dH + \frac{\mu_0}{2} \left(M(H_0 H) \frac{H_n}{H} \right)^2 + C \quad \text{on } \Gamma. \tag{2.17}$$

The expression for the function $\mu_1 = \mu_1(t)$ of the magnetostatic equation (2.12) depends either we use the magnetisation law in the form of (2.5) or (2.6). For the linear magnetised fluid with the magnetisation (2.5) we obtain

$$\mu_1(t) = 1 + \chi. \tag{2.18}$$

It means, the fluid has a constant material property. For the nonlinear magnetised fluid we get

$$\mu_1(t) = 1 + 3\chi \frac{P(\tilde{\gamma}t)}{\tilde{\gamma}t}, \quad P(t) = \coth t - \frac{1}{t}, \quad \tilde{\gamma} = \frac{3\chi H_0}{M_s}. \tag{2.19}$$

Let us mention the properties of the function μ_1 in the nonlinear form (2.19)

$$1 \le \mu_1(t) \le 1 + \chi \quad \text{for } t \ge 0; \quad P(t) \ge 0 \text{ and } P'(t) \ge 0 \quad \text{for } t \ge 0, \tag{2.20}$$

which are important for the analysis of the magnetostatic problem (2.12)-(2.16).

The problem (2.12)-(2.17) are solved for the magnetostatic potential inside and outside the fluid, for the free surface location and the unknown constant C at different values of the applied magnetic field H_0.

2.4 Decoupling strategy

The model (2.12)-(2.17) is a coupled system of nonlinear differential equations. For solving the coupled system of equations we apply an iterative decoupling strategy. It consists of two steps. A first step is to solve the magnetostatic problem (2.12)-(2.16) for a fixed boundary Γ. A second one is to solve the Young-Laplace equation (2.17) for the new calculated field.

Let us assume that all parameters $(R_0, H_0, \sigma, \mu_0, \chi, \tilde{\gamma})$ and the free surface boundary Γ are given at the k-th iteration. At the first step we solve the magnetostatic problem (2.12)-(2.16) for a fixed boundary Γ^k

$$-\nabla \cdot (\mu_i(|\nabla u_i^{k+1}|)\nabla u_i^{k+1}) = 0, \quad \text{in } \Omega_i^k; \quad \begin{aligned} \mu_1 &= 1 + \frac{M(H_0|\nabla u_1^{k+1}|)}{H_0|\nabla u_1^{k+1}|} \quad \text{in } \Omega_1^k, \\ \mu_2 &= 1 \quad\quad\quad\quad\quad\quad \text{in } \Omega_2^k, \end{aligned} \tag{2.21}$$

$$u_1^{k+1} = u_2^{k+1}, \quad \mu_1 \frac{\partial u_1^{k+1}}{\partial n} = \frac{\partial u_2^{k+1}}{\partial n} \quad \text{on } \Gamma^k, \tag{2.22}$$

$$\lim_{(r,z)\to\infty} \left(u_2^{k+1} - z\right) = 0, \tag{2.23}$$

$$\frac{\partial u_1^{k+1}}{\partial n} = 0, \quad \frac{\partial u_2^{k+1}}{\partial n} = 0 \quad \text{for } r = 0; \tag{2.24}$$

$$u_1^{k+1} = 0, \quad u_2^{k+1} = 0 \quad \text{for } z = 0. \tag{2.25}$$

Here the domain Ω_1^k is bounded by Γ^k and coordinate axes, the domain Ω_2^k is external to Ω_1^k and restricted to the first quadrant, see Fig. 2.2.

At the second step of the iterative process we define a new boundary position $\Gamma^{k+1'}$ as a solution of the Young-Laplace equation (2.17) for the new calculated field

$$\frac{\sigma}{R_0}\mathcal{K} = \mu_0 H_0 \int\limits_0^{H^{k+1}} M(H_0 H)dH + \frac{\mu_0}{2}\left(M(H_0 H^{k+1})\frac{H_n^{k+1}}{H^{k+1}}\right)^2 + C \quad \text{on } \Gamma^{k+1'}. \tag{2.26}$$

To improve numerical stability of the iterative algorithm we apply an under-relaxation technique

$$\Gamma^{k+1} = \Gamma^k + \tau(\Gamma^{k+1'} - \Gamma^k) \tag{2.27}$$

with $0 < \tau < 1$. The efficiency of the relaxation technique was discussed in [13, 52] for the coupled equations of temperature, stream function and vorticity in a wide range of Rayleigh parameters. The authors suggested algorithms for stabilisation based on numerical study of test examples. An efficient stabilisation of iterative processes by relaxation was presented for a wide class of convective problems. From the above reasoning, we apply the relaxation technique but for the coupled free boundary value problem of this Chapter, combining the magnetostatic equations and the Young-Laplace equation.

For calculations we took $\tau = 0.1$. In the case of strong shape changes the parameter τ was decreased till $\tau = 0.05$ or $\tau = 0.01$.

We solve alternately the magnetostatic problem (2.21)-(2.25) and the Young-Laplace equation (2.26). The iterative process continues unless the change in the drop shape is smaller than a prescribed threshold ε (generally 10^{-6})

$$||\Gamma^{k+1'} - \Gamma^k|| < \varepsilon. \tag{2.28}$$

Relations (2.27) and (2.28) are written formally and should be understood in a coordinate-wise manner. Here $\Gamma^\ell = \{(r^\ell, z^\ell) \mid r^\ell = r^\ell(t), \ z^\ell = z^\ell(t), \ t \in [0, L]\}$, $\ell = \{k, k+1', k+1\}$.

$$||\Gamma^{k+1'} - \Gamma^k|| = \max_{t \in T_n}\left(|r^{k+1'}(t) - r^k(t)|, |z^{k+1'}(t) - z^k(t)|\right),$$

where $T_n = \{t_j \mid 0 = t_0 < t_1 < ... < t_n = L, \ j = \overline{0, n}\}$ is a partition of the parameter interval.

If the drop equilibrium is achieved, the applied magnetic field H_0 is slowly increased and the whole computational process repeated. The initial drop shape Γ^0 for the calculations with the new value of H_0 is the calculated equilibrium shape corresponding to the preceding H_0.

For the approximation of the separated subproblems (2.21)-(2.25) and (2.26) different numerical techniques are used. An application of boundary element and finite element methods to the magnetostatic problem (2.21)-(2.25) is discussed in Chapter 3. A finite-difference and spline discretisation for the free surface equation (2.26) are presented in Chapter 4.

Chapter 3

Boundary element and finite element methods for the magnetostatic problem

An application of boundary and finite element methods to the magnetostatic problem (2.12)-(2.16) is discussed in Chapter 3. To solve Maxwell's equations both inside and outside of the magnetic fluid we use the finite element method or a coupled strategy of boundary and finite element methods. A boundary element method is used in an unbounded air domain to fulfil the boundary condition for the magnetic field at infinity while with a finite element method we resolve the non-linearity of the magnetostatic equations inside a magnetic fluid.

In Section 3.1 we present some common aspects about using a boundary element method for the solution of the Laplace equation in bounded and unbounded domains. The direct formulation of boundary integral equations is given for 3D and axisymmetric problems. A special attention is made to the boundary condition at infinity. The collocation method is applied for the discretisation of the integral equations. Kernel functions approximation and their asymptotic behaviour for axisymmetric problems are discussed.

The collocation boundary element method for the magnetostatic problem (2.12)-(2.16) inside of the linear magnetisable fluid and outside it is described in Section 3.2. As a test example, we apply a piecewise-constant collocation for the magnetostatic problem on a sphere. We show how an inexact representation of the boundary influences the convergence of the collocation method. Numerical convergence for the problem with the exact representation of the boundary and its piecewise linear and cubic spline approximations are analysed. Grid configurations with uniform and nonuniform point distribution on the boundary are considered.

Nonlinear fluid properties no longer allow to use a boundary element method inside of the fluid domain. Section 3.3 present the finite-element discretisation for the magnetostatic problem (2.12)-(2.16). The solvability of the weak formulation in weighted Sobolev spaces is studied.

In Section 3.4 we apply the coupling of the collocation boundary element method in the exterior air domain and the Galerkin finite element method in the interior fluid domain. Piecewise linears for the potential and piecewise constants for the normal derivative of the potential on the free boundary are taken.

An application of finite element methods requires a grid construction in a computational domain. In Section 3.5 two methods for the grid generation, a harmonic extension approach and a Delaunay technique, are presented. They are compared with respect to the quality of the generated grids and the computational efficiency of the underlying algorithms in application to the coupled magnetostatic and free surface problem.

3.1 Boundary element method for the Laplace equation

A boundary element method transforms a partial differential equation defined on a d-dimensional domain to an integral equation defined on $(d-1)$-dimensional boundary of the domain. The solution of a boundary value problem is sought as a solution of an equivalent boundary integral equation containing one or more unknown functions as well as a known fundamental solution of the differential equation to be solved.

The formulation of a boundary element method for the given boundary value problem depends on the availability of an explicit fundamental solution of this problem. It restricts the method mainly to linear differential equations with constant coefficients. One of the important applications of a boundary element method is the solution of Laplace equations, see [19].

The reduction of boundary value problems to equivalent boundary integral equations can be done with many different methods. The two most popular methods are the direct method and the indirect method or method of layer potentials. Standard approaches to solve boundary integral equations are the collocation method, the Galerkin method and the Nyström method. For more detailed information we refer to [22, 31, 76].

In the thesis we use a direct formulation of boundary integral equations based upon the Green's representation formula. Further discretisation of the boundary integral equations are realised by the collocation method.

At the beginning let us introduce the fundamental solution for the Laplace operator and define the surface potentials.

The fundamental solution of the Laplace operator

The fundamental solution $u^*(\xi^0, \xi)$ of a differential operator L satisfy

$$Lu^* = \begin{cases} 0 & \text{for } \xi \neq \xi^0, \\ \delta_{\xi^0} & \text{for } \xi = \xi^0. \end{cases}$$

Here $\xi^0, \xi \in \mathbb{R}^d$ and δ_{ξ^0} is the delta function concentrated at the point ξ^0.

The fundamental solution for the Laplace operator in $\mathbb{R}^3$ has the form

$$u^*_{3D}(\xi^0, \xi) = \frac{1}{4\pi\rho(\xi^0, \xi)}, \quad \rho(\xi^0, \xi) = |\xi^0 - \xi|,$$

where $\rho(\xi^0, \xi)$ is the distance between the source point $\xi^0 = (x^0, y^0, z^0)$ and the point $\xi = (x, y, z)$. The three-dimensional fundamental solution in cylindrical coordinates (r, θ, z) gives

$$u^*_{3D}(\xi^0, \xi) = \frac{1}{4\pi\sqrt{r^2 + (r^0)^2 - 2rr^0\cos(\theta - \theta^0) + (z - z^0)^2}},$$

where $\xi^0 = (r^0, \theta^0, z^0)$, $\xi = (r, \theta, z)$.

Surface potentials

The domain D_1 is a bounded open domain in $\mathbb{R}^3$ with the boundary S. The surface integrals for a given function u on S define the single-layer $\tilde{\mathbf{V}}_1$ and the double-layer potentials $\tilde{\mathbf{V}}_2$

$$(\tilde{\mathbf{V}}_1 u)(\xi^0) = \int_S u^*_{3D}(\xi^0, \xi)u(\xi)dS \quad \text{for } \xi^0 \in \mathbb{R}^3 \tag{3.1}$$

$$(\tilde{\mathbf{V}}_2 u)(\xi^0) = \int_S q^*_{3D}(\xi^0, \xi)u(\xi)dS \quad \text{for } \xi^0 \in \mathbb{R}^3, \quad q^*_{3D} = \frac{\partial u^*_{3D}}{\partial n}. \tag{3.2}$$

The derivative q_{3D}^* is in respect to ξ.

Let $(\mathbf{V}_1 u)(\xi^0)$ and $(\mathbf{V}_2 u)(\xi^0)$ be boundary operators corresponding to the restriction of the single-layer and double-layer potentials to the boundary S

$$(\mathbf{V}_1 u)(\xi^0) = \int_S u_{3D}^*(\xi^0, \xi) u(\xi) dS \quad \text{for } \xi^0 \in S, \tag{3.3}$$

$$(\mathbf{V}_2 u)(\xi^0) = \int_S q_{3D}^*(\xi^0, \xi) u(\xi) dS \quad \text{for } \xi^0 \in S. \tag{3.4}$$

An important feature of the surface potentials is their behaviour when a point ξ_0 tends to the boundary S from the interior or the exterior of the domain D_1. The next theorem states regularity of the surface potentials (3.1)-(3.2) and their jump properties.

Theorem 3.1.1 (Theorem 6.5.1 in [22]) *Let $D_1 \subset \mathbb{R}^3$ be bounded with the boundary $S \in C^\infty$. Let $u \in H^\alpha(S)$, $\alpha \in \mathbb{R}$, then $\mathbf{V}_1 : H^\alpha(S) \to H^{\alpha+1}(S)$, $\mathbf{V}_2 : H^\alpha(S) \to H^\alpha(S)$. Denote*

$$(\tilde{\mathbf{V}}_i u)^-(\xi^0) = \begin{cases} (\tilde{\mathbf{V}}_i u)(\xi^0) & \text{if } \xi^0 \in D_1, \\ \lim_{\eta \to \xi^0, \, \eta \in D_1} (\tilde{\mathbf{V}}_i u)(\eta) & \text{if } \xi^0 \in S, \end{cases} \tag{3.5}$$

$$(\tilde{\mathbf{V}}_i u)^+(\xi^0) = \begin{cases} (\tilde{\mathbf{V}}_i u)(\xi^0) & \text{if } \xi^0 \in D_2, \\ \lim_{\eta \to \xi^0, \, \eta \in D_2} (\tilde{\mathbf{V}}_i u)(\eta) & \text{if } \xi^0 \in S, \end{cases} \tag{3.6}$$

where the limits are taken in the pointwise sense, $i = 1, 2$. Then for the restriction of operators (3.5) and (3.6) to the boundary S, we have

$$\mathbf{V}_1^- : H^\alpha(S) \to H^{\alpha+1}(S) \quad \text{such that} \quad \mathbf{V}_1^- u = \mathbf{V}_1 u, \tag{3.7}$$
$$\mathbf{V}_1^+ : H^\alpha(S) \to H^{\alpha+1}(S) \quad \text{such that} \quad \mathbf{V}_1^+ u = \mathbf{V}_1 u, \tag{3.8}$$
$$\mathbf{V}_2^- : H^\alpha(S) \to H^\alpha(S) \quad \text{such that} \quad \mathbf{V}_2^- u = (-1/2\mathbf{I} + \mathbf{V}_2)u, \tag{3.9}$$
$$\mathbf{V}_2^+ : H^\alpha(S) \to H^\alpha(S) \quad \text{such that} \quad \mathbf{V}_2^+ u = (1/2\mathbf{I} + \mathbf{V}_2)u. \tag{3.10}$$

Furthermore, $\mathbf{V}_i, \mathbf{V}_i^-, \mathbf{V}_i^+$, $i = 1, 2$ are continuous linear operators.

3.1.1 Direct formulation of boundary integral equations

Representation formula for bounded domain

A solution of the Laplace equation in the interior domain $D_1 \subset \mathbb{R}^3$ with a boundary $S = \partial D_1$ satisfies the Green's representation formula, see [30]

$$u(\xi^0) + \int_S q_{3D}^*(\xi^0, \xi) u(\xi) dS - \int_S u_{3D}^*(\xi^0, \xi) q(\xi) dS = 0 \quad \text{for } \xi^0 \in D_1, \tag{3.11}$$

where $q = \partial u / \partial n$, $q_{3D}^* = \partial u_{3D}^* / \partial n$ with derivatives in respect to ξ and the unit normal vector n is the outward for the domain D_1.

Equation (3.11) can be written as a linear combination of the surface potentials

$$u(\xi^0) + (\tilde{\mathbf{V}}_2 u)(\xi^0) - (\tilde{\mathbf{V}}_1 q)(\xi^0) = 0 \quad \text{in } D_1.$$

Letting ξ^0 tends to a boundary point, by jump properties (3.7)-(3.10) we have

$$1/2 u(\xi^0) + (\mathbf{V}_2 u)(\xi^0) - (\mathbf{V}_1 q)(\xi^0) = 0 \quad \text{on } S.$$

It allows us to write the Green's representation formula as

$$k_1(\xi^0)u(\xi^0) + (\tilde{\mathbf{V}}_2 u)(\xi^0) - (\tilde{\mathbf{V}}_1 q)(\xi^0) = 0 \quad \text{in } \bar{D}_1, \tag{3.12}$$

where $k_1(\xi^0)$ is a geometric constant, equals 1 inside D_1 and $1/2$ on the boundary S.

Representation formula for an unbounded domain

Let u be a weak solution of the Laplace equation in the exterior domain D_2 such that

$$u \in H^1_{loc}(D_2) = \{u \mid u \in H^s(K) \text{ for every compact set } K \subset D_2\}$$

and for some constant c following conditions fulfil

$$u(\xi) = c + O(|\xi|^{-1}), \quad \nabla u(\xi) = O(|\xi|^{-2}) \quad \text{for } |\xi| \to \infty. \tag{3.13}$$

Conditions (3.13) guarantee the unique solvability of the Laplace equation in three-dimensional unbounded domains. The solution u then satisfies, see Lemma 6.9.1 in [22],

$$u(\xi^0) - \int_S q^*_{3D}(\xi^0, \xi)u(\xi)dS + \int_S u^*_{3D}(\xi^0, \xi)q(\xi)dS = c \quad \text{for } \xi^0 \in D_2. \tag{3.14}$$

The solution of the magnetostatic problem (2.12)-(2.16) should satisfy the condition at infinity

$$\lim_{(r,z)\to\infty} (u - z) = 0.$$

Let us introduce a new function

$$\tilde{u} = u - z.$$

The function $\tilde{u}$ satisfies conditions (3.13) hence from (3.14) we can write

$$\tilde{u}(\xi^0) - \int_S q^*_{3D}(\xi^0, \xi)\tilde{u}(\xi)dS + \int_S u^*_{3D}(\xi^0, \xi)\tilde{q}(\xi)dS = 0 \quad \text{for } \xi^0 \in D_2,$$

where $\tilde{q} = \partial\tilde{u}/\partial n$. It allows us to write

$$u(\xi^0) - \int_S q^*_{3D}(\xi^0, \xi)u(\xi)dS + \int_S u^*_{3D}(\xi^0, \xi)q(\xi)dS = \tag{3.15}$$
$$z^0 - \int_S q^*_{3D}(\xi^0, \xi)zdS \quad + \int_S u^*_{3D}(\xi^0, \xi)\frac{\partial z}{\partial n}dS,$$

where n is an inner normal vector for D_2.

Let $S_r(\xi^0)$ be the sphere with center ξ^0 and radius r. The domain D_2 can be considered as internally bounded by the surface S and externally by the surface S_r with $r \to \infty$. The Green's formula (3.11) allows to write for the harmonic function $u = z$ in the bounded domain D_2 that

$$z^0 + \int_{\partial D_2} q^*_{3D}(\xi^0, \xi)zdS - \int_{\partial D_2} u^*_{3D}(\xi^0, \xi)\frac{\partial z}{\partial n}dS = 0.$$

We have $\partial D_2 = S \cup S_r(\xi^0)$ and $\int_{\partial D_2} = \int_{\partial S} + \int_{\partial S_r(\xi^0)}$ with the normal vector outer for D_2. The right-hand side of equation (3.15) we can write then as

$$z^0 - \int_S q_{3D}^*(\xi^0, \xi) z \, dS \quad + \int_S u_{3D}^*(\xi^0, \xi) \frac{\partial z}{\partial n} dS =$$

$$- \int_{S_r(\xi^0)} q_{3D}^*(\xi^0, \xi) z \, dS + \int_{S_r(\xi^0)} u_{3D}^*(\xi^0, \xi) \frac{\partial z}{\partial n} dS.$$

To calculate integrals over the surface $S_r(\xi^0)$ we go to the spherical coordinates (ρ, θ, φ). Then

$$S_r(\theta, \varphi) = \begin{pmatrix} r \sin\theta \cos\varphi \\ r \sin\theta \sin\varphi \\ r \cos\theta \end{pmatrix}, \quad dS = r^2 \sin\theta \, d\theta \, d\varphi.$$

The normal direction is radial on the sphere, then it follows that

$$q^* = \frac{\partial u^*}{\partial r} = -\frac{1}{4\pi r^2} \quad \text{for } \xi \in S_r(\xi^0),$$

$$\frac{\partial z}{\partial n} = \cos\theta \quad \text{for } z = z^0 + r\cos\theta \text{ on } S_r(\xi^0).$$

We can write that

$$- \int_{S_r(\xi^0)} q_{3D}^*(\xi^0, \xi) z \, dS + \int_{S_r(\xi^0)} u_{3D}^*(\xi^0, \xi) \frac{\partial z}{\partial n} dS =$$

$$\int_0^\pi \int_0^{2\pi} \left(\frac{1}{4\pi r^2}(z^0 + r\cos\theta) + \frac{1}{4\pi r}\cos\theta \right) r^2 \sin\theta \, d\theta \, d\varphi =$$

$$2\pi \frac{1}{4\pi} \left(\int_0^\pi z^0 \sin\theta \, d\theta + 2 \int_0^\pi \rho \cos\theta \sin\theta \, d\theta \right) = \frac{1}{2}(2z^0 + 0) = z^0.$$

Finally we write equation (3.15) as

$$u(\xi^0) - \int_S q_{3D}^*(\xi^0, \xi) u(\xi) dS + \int_S u_{3D}^*(\xi^0, \xi) q(\xi) dS = z^0 \tag{3.16}$$

or in operator form as

$$u(\xi^0) - (\tilde{\mathbf{V}}_2 u)(\xi^0) + (\tilde{\mathbf{V}}_1 q)(\xi^0) = z^0 \quad \text{in } D_2. \tag{3.17}$$

The boundary equation (3.17) is the representation formula for the potential in the exterior domain D_2 with the condition $u = z$ at infinity.

Letting ξ^0 tends to a boundary point, from (3.17) by jump properties (3.7)-(3.10) we have

$$1/2 u(\xi^0) - (\mathbf{V}_2 u)(\xi^0) + (\mathbf{V}_1 q)(\xi^0) = z^0 \quad \text{on } S.$$

The final representation formula take the form, analogous to (3.12),

$$k_2(\xi^0) u(\xi^0) - (\bar{\tilde{\mathbf{V}}}_2 u)(\xi^0) + (\bar{\tilde{\mathbf{V}}}_1 q)(\xi^0) = z^0 \quad \text{in } \bar{D}_2, \tag{3.18}$$

where $k_2(\xi^0)$ is a geometric constant, equals 1 inside D_2 and $1/2$ on the boundary S.

Axisymmetric case

Assuming that the boundary S is a surface of revolution, we can rewrite the surface potentials (3.1) and (3.2) in cylindrical coordinates (r, θ, z) as

$$(\tilde{\mathbf{V}}_1 u)(x^0, y^0, z^0) = \int_\Gamma u(\xi) \int_0^{2\pi} u^*_{3D}(\xi^0, \xi) r d\theta d\Gamma,$$

$$(\tilde{\mathbf{V}}_2 u)(x^0, y^0, z^0) = \int_\Gamma u(\xi) \int_0^{2\pi} q^*_{3D}(\xi^0, \xi) r d\theta d\Gamma,$$

where $\xi^0 = (r^0, z^0)$ and $\xi = (r, z)$. Here, Γ is a meridian line of the domain D_1, see Fig. 2.2.

The fundamental solution u^*_{3D} can be analytically integrated over θ. We introduce the axisymmetric fundamental solution in the next form

$$u^*_{ax}(\xi^0, \xi) = \int_0^{2\pi} u^*_{3D}(\xi^0, \xi) d\theta = \frac{1}{2\pi} \int_0^\pi \frac{d\theta}{\sqrt{a - b \cos\theta}},$$

where $a = r^2 + (r^0)^2 + (z - z^0)^2$, $b = 2rr^0$. Now let us express the fundamental solution u^*_{ax} in the form of elliptic integrals

$$
\begin{aligned}
u^*_{ax}(\xi^0, \xi) &= \frac{1}{2\pi} \int_0^\pi \frac{d\theta}{\sqrt{a + b - 2b \cos^2(\theta/2)}} = \frac{1}{\pi} \int_0^{\pi/2} \frac{d\theta}{\sqrt{a + b - 2b \sin^2\theta}}, \\
&= \frac{1}{\pi\sqrt{a + b}} \int_0^{\pi/2} \frac{d\theta}{\sqrt{1 - \frac{2b}{a+b} \sin^2\theta}} = \frac{K(m)}{\pi\sqrt{a + b}}.
\end{aligned}
\tag{3.19}
$$

Here $K(m)$ is the complete elliptic integral of the first kind with $m = 2b/(a + b)$, $0 \le m \le 1$.

The normal derivative of the fundamental solution $q^*_{ax}(\xi^0, \xi)$ is given by

$$q^*_{ax}(\xi^0, \xi) = \frac{\partial u^*_{ax}(\xi^0, \xi)}{\partial r} n_r(\xi) + \frac{\partial u^*_{ax}(\xi^0, \xi)}{\partial z} n_z(\xi), \tag{3.20}$$

where $n = (n_r(\xi), n_z(\xi))$ is the unit normal vector and

$$\frac{\partial u^*_{ax}(\xi^0, \xi)}{\partial r} = \frac{1}{2\pi r\sqrt{a + b}} \left(-K(m) + \frac{(r^0)^2 - r^2 + (z - z^0)^2}{|\xi - \xi^0|^2} E(m) \right), \tag{3.21}$$

$$\frac{\partial u^*_{ax}(\xi^0, \xi)}{\partial z} = \frac{z^0 - z}{\pi |\xi - \xi^0|^2 \sqrt{a + b}} E(m). \tag{3.22}$$

Here $E(m)$ is the complete elliptic integral of the second kind. To get (3.22) the relation

$$\frac{dK(m)}{dm} = \frac{E(m) - (1 - m)K(m)}{2m(1 - m)}$$

was used, see [25]. Finally we can define the axisymmetric boundary operators $\tilde{\mathbf{V}}_{1,ax}$ and $\tilde{\mathbf{V}}_{2,ax}$

$$(\tilde{\mathbf{V}}_1 u)(x^0, y^0, z^0) = (\tilde{\mathbf{V}}_{1,ax} u)(\xi^0) = \int_\Gamma u_{ax}^*(\xi^0, \xi) u(\xi) r d\Gamma,$$

$$(\tilde{\mathbf{V}}_2 u)(x^0, y^0, z^0) = (\tilde{\mathbf{V}}_{2,ax} u)(\xi^0) = \int_\Gamma q_{ax}^*(\xi^0, \xi) u(\xi) r d\Gamma.$$

The representation formulas for the axisymmetric potential in bounded (3.12) and unbounded domains (3.18) take the following forms

$$k_1(\xi^0) u(\xi^0) + (\tilde{\mathbf{V}}_{2,ax} u)(\xi^0) - (\tilde{\mathbf{V}}_{1,ax} q)(\xi^0) = 0 \quad \text{in } \bar{\Omega}_1, \tag{3.23}$$

$$k_2(\xi^0) u(\xi^0) - (\tilde{\mathbf{V}}_{2,ax} u)(\xi^0) + (\tilde{\mathbf{V}}_{1,ax} q)(\xi^0) = z^0 \quad \text{in } \bar{\Omega}_2, \tag{3.24}$$

with

$$k_1 = \begin{cases} 1/2 & \text{on } \Gamma \\ 1 & \text{in } \Omega_1 \end{cases}, \quad k_2 = \begin{cases} 1/2 & \text{on } \Gamma \\ 1 & \text{in } \Omega_2 \end{cases}.$$

3.1.2 Boundary discretisation

The smooth curve Γ in $\mathbb{R}$ can be described by means of a real-valued differentiable parametrisation

$$\Gamma = \{\xi \mid \xi = \psi(t), \ t \in [0, L]\} \quad \text{or} \quad \Gamma = \{(r, z) \mid r = r(t), \ z = z(t), \ t \in [0, L]\}, \tag{3.25}$$

where $|\psi'(t)| > 0$ and $\sqrt{r'(t)^2 + z'(t)^2} > 0$.

Let us introduce a sequence of grid points

$$\Xi_n = \{\xi_j \mid \xi_j = \psi(t_j), \ t_j \in T_n\},$$

which corresponds to a partition of the parameter interval $[0, L]$

$$T_n = \{t_j \mid 0 = t_0 < t_1 < ... < t_n = L, \ j = \overline{0, n}\}.$$

The curve Γ can be considered as a union of finitely many plane curves or boundary elements

$$\Gamma = \cup \Gamma_j, \ j = \overline{1, n},$$

where grid points ξ_{j-1} and ξ_j are the end points of the boundary element Γ_j.

The boundary Γ can be approximated by Γ_h such that

$$\psi_h(t) : [0, L] \to \Gamma_h, \text{ where } \psi_h(t_j) = \xi_j \text{ for } j = \overline{0, n}. \tag{3.26}$$

The approximate boundary Γ_h can be defined in the polynomial spline spaces $S_{r,m}(\Xi_n)$. Following [22] the polynomial spline spaces in one dimension are defined as

$$S_{r,m}(T_n) = \begin{cases} \{u \in C^{m-1}(T_n) \mid u|_{(t_{j-1}, t_j)} \in P_{r-1}(t_{j-1}, t_j), \ j = \overline{1, n}\} & \text{for } 0 < m < r, \\ \{u \in L^2(T_n) \mid u|_{(t_{j-1}, t_j)} \in P_{r-1}(t_{j-1}, t_j), \ j = \overline{1, n}\} & \text{for } m = 0, \end{cases} \tag{3.27}$$

where r, m are integers. We have that

- $S_{1,0}(T_n)$ is a space of piecewise constant functions,

- $S_{r,1}(T_n)$ is a Lagrangian system, see for instance [78],

- if $m = r - 1$ then $S_{r,m}(T_n)$ is called the space of polynomial B-splines,

- if $m = r > 0$ then $S_{r,m}(T_n)$ can be defined as $P_{r-1}(0, L)$.

The simplest way to approximate the boundary is to connect boundary points ξ_j by line segments. Then $\psi_h(t) \in S_{2,1}(T_n)$ and

$$\psi_h(t) = \xi_{j-1} + (t - t_{j-1})\frac{\xi_j - \xi_{j-1}}{t_j - t_{j-1}} \quad \text{for } t \in [t_{j-1}, t_j]. \tag{3.28}$$

The boundary can be approximated by higher order polynomials, for instance, by a parametric cubic spline $\psi_h(t) \in S_{4,3}(T_n)$. Let $\ell_j = |\xi_j - \xi_{j-1}|$. Setting $t_j = \sum_{k=1}^{j} \ell_k$ for $j = \overline{1, n}$, every t_j represents the cumulative length of the piecewise line that joints the points from ξ_0 to ξ_j. Additionally, the conditions at the end points ξ_0 and ξ_n should be formulated for the complete definition of the spline approximation.

Remark 3.1.1 *A parametric spline for such a type of parametrisation is called the cumulative length spline and approximates satisfactorily even those curves with large curvature, see [59].*

In order to compare a solution $u(\xi)$ of a boundary integral equation on the exact boundary Γ with the solution $u_h(\xi)$ of the same integral equation but on the approximate boundary Γ_h, it is necessary to define a map F of Γ_h on Γ. Let the exact and approximate boundaries be given by parametrisations (3.25) and (3.26). Then one can use the mapping

$$F = \psi \circ \psi_h^{-1}. \tag{3.29}$$

Let us present now the collocation method for solving the boundary integral equations.

3.1.3 Collocation method

We summarise some results about collocation methods following [6, 7, 65]. Let

$$(Au)(\xi) = g(\xi), \quad \text{for } \xi \in \Gamma \tag{3.30}$$

be a boundary integral equation on the boundary Γ of a domain Ω for any continuous function $g(\xi)$. Let A be a strongly elliptic pseudodifferential operator of order α, see for instance [22]. Assume that

$$A : H^s \to H^{s-\alpha} \text{ is an isomorphism for any } s \in \mathbb{R}. \tag{3.31}$$

Let Γ be a smooth curve in $\mathbb{R}$ given by a parameterisation $\psi(t)$, see (3.25), which is additionally L-periodic, i.e. $\psi(t) = \psi(t + L)$. We consider the boundary Γ as a union of boundary elements Γ_j, $j = \overline{1, n}$ with a corresponding partition T_n of the parameter interval $[0, L]$.

Let us denote by $S_r(T_n)$ the space of all L-periodic $(r - 1)$ times continuously differentiable splines of order r subordinate to the partition T_n. This space corresponds to $S_{r+1,r}(T_n)$, see (3.27). Let us assume that the space $S_r(T_n)$ is a subspace of $H^\tau([0, L])$. For all $u \in S_r(T_n)$ the r-th derivative is a piecewise constant function. It follows that

$$S_r(T_n) \in H^{r+1/2-\epsilon}([0, L]) \quad \text{for any } \epsilon > 0,$$

see for instance in [22]. Finally we can conclude that

$$S_r(T_n) \in H^\tau([0, L]) \quad \text{for } \tau < r + 1/2. \tag{3.32}$$

We introduce a sequence of collocation points such that

$$\tilde{\Xi}_n = \begin{cases} \left\{ \tilde{\xi}_i \mid \tilde{\xi}_i = \psi\left(\dfrac{t_{i-1} + t_i}{2}\right), \ i = \overline{1,n} \right\} & \text{for } r \text{ even,} \\[2mm] \left\{ \tilde{\xi}_i \mid \tilde{\xi}_i = \psi(t_i), \ i = \overline{0,n} \right\} & \text{for } r \text{ odd.} \end{cases} \tag{3.33}$$

Such a choice of collocation points is called *naive collocation*, see [6, 7].

The collocation problem is to find $u_h \in S_r(\Xi_n)$ such that

$$(Au_h)(\tilde{\xi}_i) = g(\tilde{\xi}_i) \quad \text{for } \tilde{\xi} \in \tilde{\Xi}_n. \tag{3.34}$$

In order the collocation problem (3.34) to be well defined, $(Au_h)(\xi)$ and $g(\xi)$ should be continuous at the collocation points $\tilde{\xi}_i \in \tilde{\Xi}_n$. From assumption (3.31) we have $Au_h \in H^{\tau-\alpha}(\Gamma)$ for any $u_h \in H^\tau(\Gamma)$. From the Sobolev imbedding theorem, see [2, Theorem 5.4], we have that

$$H^{\tau-\alpha+1/2}(\Omega) \rightarrow C^0(\bar{\Omega}) \quad \text{for } \tau - \alpha > 1/2.$$

It follows that

$$H^{\tau-\alpha}(\Gamma) \rightarrow C^0(\Gamma) \quad \text{for } \tau - \alpha > 1/2.$$

Finally with condition (3.32) we get

$$Au_h \in C^0(\Gamma) \quad \text{for } \alpha < r. \tag{3.35}$$

Remark 3.1.2 *In the even degree case condition (3.35) can be relaxed, see [7]*

$$Au_h \in C^0(\Gamma) \quad \text{for } \alpha < r + 1/2. \tag{3.36}$$

In the same manner we get a condition for the continuity of the function $g(\xi)$

$$g \in C^0(\Gamma) \quad \text{for any } u \in H^\beta(\Gamma) \text{ and for } \beta - \alpha > 1/2. \tag{3.37}$$

The best asymptotic convergence results of the collocation method applied to a strongly elliptic pseudo-differential equation (3.30) using polynomial splines $S_r(T_n)$ were obtained in [7], improving earlier results in [6], [65]. The analysis in mentioned above papers is based on the reformulation of the collocation equations as equivalent Galerkin equations and further treatment of these equations by Fourier analysis techniques.

Theorem 3.1.2 ([7],[65]) *Let A be a strongly elliptic pseudodifferential operator of order α as defined in (3.31). Let $u_h \in S_r(T_n)$ be a solution of the collocation problem (3.34) for the uniform T_n, provided conditions (3.32), (3.35), (3.37) are satisfied.*
Then there exist a constant $C > 0$ independent of h such that for all $0 < h \leq h_0$ and any continuous function $g(\xi)$ the collocation equations (3.34) are uniquely solvable and the optimal error estimate

$$||u - u_h||_{H^\tau(\Gamma)} \leq Ch^{\beta-\tau}||u||_{H^\beta(\Gamma)} \tag{3.38}$$

holds, provided $\alpha \leq \tau \leq \beta \leq r + 1$.

Remark 3.1.3 *Let us assume that we are interested in the L_2-estimate for the error in the case of piecewise-constant collocation. From Theorem 3.1.2 we have*

$$||u - u_h||_{L^2(\Gamma)} \leq Ch^\beta||u||_{H^\beta(\Gamma)} \quad \text{for } \beta - \alpha > 1/2, \ 0 \leq \beta \leq 1.$$

It follows that for the piecewise-constant collocation method the first order of convergence is the maximum order, predicted by the theory.

Remark 3.1.4 *The collocation method converges at most with the order $h^{r+1-\alpha}$, whereas the Galerkin method for the same spline approximation converges at most with the order $h^{2r+2-\alpha}$, see [77].*

Discrete system

The collocation problem (3.34) is equivalent to the quadratic system of linear equations

$$\sum_{j=1}^{n}(A\Phi_j)(\tilde{\xi}_i)\alpha_j = g(\tilde{\xi}_i), \quad i = \overline{1, n} \tag{3.39}$$

for unknowns $\alpha_1, \ldots, \alpha_n$, where $\{\Phi_j\}_{j=1}^{n}$ denote a basis of the space $S_r(T_n)$. The set of linear algebraic equations (3.39) can be expressed in the matrix form

$$\mathbf{H}\alpha = f$$

with the matrix $\mathbf{H} = (H_{ij})$ being the results of integration for the collocation points $\tilde{\xi}_i$ (row) and the basis function Φ_j (column)

$$H_{ij} = (A\Phi_j)(\tilde{\xi}_i), \quad i, j = \overline{1, n}.$$

Let us assume that the boundary Γ is described by a parametrisation $\psi(t)$, see (3.25). For the boundary, presented as a union of boundary elements, we can write

$$
\begin{aligned}
H_{ij} &= \sum_{k=1}^{n} \int_{\Gamma_k} a(\tilde{\xi}_i, \xi)\Phi_j(\xi)d\xi \\
&= \sum_{k=1}^{n} \int_{t_{k-1}}^{t_k} (a \circ \psi)(\tilde{t}_i, t)(\Phi_j \circ \psi)(t)|\psi'(t)|dt, \quad i, j = \overline{1, n}.
\end{aligned}
$$

Here $a(\tilde{\xi}_i, \xi)$ is a kernel of the integral operator A and $\tilde{\xi}_i = \psi(\tilde{t}_i)$.

Remark 3.1.5 *For the piecewise-constant collocation we have*

$$H_{ij} = \int_{t_{j-1}}^{t_j} (a \circ \psi)(\tilde{t}_i, t)|\psi'(t)|dt \quad \text{for } u_h \in S_0(T_n).$$

Numerical integration

In numerical calculations with a boundary element method the final error has mainly two reasons, the error is due to the applied discretisation approach and due to the numerical integration.

Depending on the nature of the kernel $a(\tilde{\xi}_i, \xi)$ and the relative position of the collocation point $\tilde{\xi}_i$ with respect to the boundary element Γ_k on which integration is being carried out, we can have regular, weakly singular, strongly singular and hypersingular integrals for the entries of the matrix $\mathbf{H}$.

Regular integrals appear when the collocation point $\tilde{\xi}_i$ does not belong to the boundary element Γ_k $(i \neq k)$. Evaluation of the regular integrals can be carried out by n-point Gaussian quadrature formulas which integrates exactly a polynomial of degree $2n - 1$. The weights and abscissas for these formulas can be found in [1].

Weakly singular integrals occur when the collocation point $\tilde{\xi}_i$ lies within the boundary element Γ_k $(i = k)$ and additionally

$$a(\tilde{\xi}_i, \xi) = O\left(\ln \frac{1}{|\xi - \tilde{\xi}_i|}\right) \quad \text{for } \xi \in \Gamma_i.$$

A possible approach to handle weakly singular integrals is to apply logarithmically weighted Gaussian quadrature formulas. The weights and abscissas for these formulas with $\ln(1/t)$ as the weighting function can be found in [70] to evaluate integrals over $t \in [0, 1]$.

Strongly singular integrals appear when the collocation point $\tilde{\xi}_i$ lies within the boundary element Γ_k $(i = k)$ and the kernel is a singular function of the following order

$$a(\tilde{\xi}_i, \xi) = O\left(\frac{1}{|\xi - \tilde{\xi}_i|}\right) \quad \text{for } \xi \in \Gamma_i.$$

In such situations the integrals only exist in the sense of their Cauchy principal values, see [31]. Kutt's quadrature can be used for the computation of Cauchy principal value integrals, see for instance Chapter 11 in [80].

Hypersingular integrals occur when the collocation point $\tilde{\xi}_i$ lies within the boundary element Γ_k $(i = k)$ and the kernel function satisfies

$$a(\tilde{\xi}_i, \xi) = O\left(\frac{1}{|\xi - \tilde{\xi}_i|^2}\right) \quad \text{for } \xi \in \Gamma_i.$$

Such integrals exist in the sense of the Hadamard principal values, see [31].

Let us denote by $\tilde{H}_{ij}$ the numerically integrated analog of H_{ij} such that

$$|H_{ij} - \tilde{H}_{ij}| \leq ch^\rho.$$

Let d denote the degree of precision of the numerical integration formula. According to results in Chapter 6.2 in [76] we can get that for regular integrals

$$|H_{ij} - \tilde{H}_{ij}| \leq ch^\rho, \quad \rho = d + 2 - r. \tag{3.40}$$

An application of numerical integration for calculating entries of the matrix $\mathbf{H}$ gives additional error to the estimate (3.38). The complete error of the collocation problem (3.34), according to Theorem 6.2 in [76], is given by

$$||u - u_h||_{H^\tau(\Gamma)} \leq Ch^{\beta-\tau}||u||_{H^\beta(\Gamma)} + ch^s||u||_{H^{\max\{0,\alpha\}}}, \tag{3.41}$$

provided the partition T_n is quasiuniform, $s = \rho + \min\{0, -\tau\} - 1 + \min\{0, \alpha\}$.

Let us assume that we are interested in the L^2-estimate for the error, when the exact solution $u \in H^1(\Gamma)$. Then from (3.40) and (3.41) we have

$$||u - u_h||_{L^2(\Gamma)} \leq Ch||u||_{H^1(\Gamma)} + ch^s||u||_{H^{\max\{0,\alpha\}}}, \tag{3.42}$$

for $s = d + 1 - r + \min\{0, \alpha\}$. It is natural to require for the second term of the upper bound in the estimate (3.42) not to worse the common order, i.e. to satisfy

$$s \geq 1. \tag{3.43}$$

It is known that for Gaussian quadrature formulas

$$d = 2n - 1, \tag{3.44}$$

where n is a number of integration points. From (3.42)-(3.44) we can get

$$n \geq \frac{r - \min\{0, \alpha\} + 1}{2}. \tag{3.45}$$

Condition (3.45) it is necessary to fulfil for calculating regular integrals by Gaussian formulas not to worse the common error (3.42).

Asymptotic behaviour of kernel functions for $\xi \to \xi^0$

The integral operators $\tilde{\mathbf{V}}_{1,ax}$ and $\tilde{\mathbf{V}}_{2,ax}$ for the axisymmetric potential problem

$$(\tilde{\mathbf{V}}_{1,ax} u)(\xi^0) = \int_\Gamma u_{ax}^*(\xi^0, \xi) u(\xi) r d\Gamma, \quad (\tilde{\mathbf{V}}_{2,ax} u)(\xi^0) = \int_\Gamma q_{ax}^*(\xi^0, \xi) u(\xi) r d\Gamma$$

contain the following kernel functions

$$a_1(\xi^0, \xi) = u_{ax}^*(\xi^0, \xi) r, \quad a_2(\xi^0, \xi) = q_{ax}^*(\xi^0, \xi) r.$$

The axisymmetric fundamental solution u_{ax}^* and its normal derivative q_{ax}^* include in their expressions the complete elliptic integrals of the first kind $K(m)$ and the second kind $E(m)$. Using relations (3.19)-(3.22), we get

$$
\begin{aligned}
a_1(\xi^0, \xi) &= \frac{K(m)}{\pi\sqrt{a+b}} r, \\
a_2(\xi^0, \xi) &= \frac{1}{2\pi\sqrt{a+b}} \left(-K(m) + \frac{(r^0)^2 - r^2 + (z - z^0)^2}{|\xi - \xi^0|^2} E(m) \right) n_r(\xi) + \\
&\quad \frac{1}{\pi\sqrt{a+b}} \frac{r(z^0 - z)}{|\xi - \xi^0|^2} E(m) n_z(\xi).
\end{aligned}
\tag{3.46}
$$

Here $m = 2b/(a+b)$, $a = r^2 + (r^0)^2 + (z - z^0)^2$, $b = 2rr^0$.

The elliptic integrals can not be calculated exactly. The widely-used technique is to approximate them by polynomials for $0 \leq m \leq 1$, see [1]

$$
\begin{aligned}
K(m) &= \tilde{K}(m) + \varepsilon(m), \quad \tilde{K}(m) = p_1(m) + p_2(m) \ln \frac{1}{1-m}, \quad |\varepsilon(m)| \leq 2 \cdot 10^{-8}; \\
E(m) &= \tilde{E}(m) + \varepsilon(m), \quad \tilde{E}(m) = p_3(m) + p_4(m) \ln \frac{1}{1-m}, \quad |\varepsilon(m)| \leq 2 \cdot 10^{-8}.
\end{aligned}
$$

Here functions $p_i(m)$, $i = \overline{1,4}$ are fourth-order polynomials with given coefficients such that

$$p_i(m) = p_i^0 + p_i^1(1-m) + p_i^2(1-m)^2 + p_i^3(1-m)^3 + p_i^4(1-m)^4,$$

	$i = 1$	$i = 2$	$i = 3$	$i = 4$
p_i^0	1.38629436112	0.5	1	0
p_i^1	0.09666344259	0.12498593597	0.44325141463	0.24998368310
p_i^2	0.03590092383	0.06880248576	0.06260601220	0.09200180037
p_i^3	0.03742563713	0.03328355346	0.04757383546	0.04069697526
p_i^4	0.01451196212	0.00441787012	0.01736506451	0.00526449639

The function $K(m)$ contains a singularity for $m \to 1$

$$\lim_{m \to 1} K(m) = \int_0^{\pi/2} \frac{d\theta}{\sqrt{1 - \sin^2 \theta}} = \int_0^1 \frac{dt}{t^2 - 1}.$$

By construction, therefore, the approximate function $\tilde{K}(m)$ is also singular for $m = 1$ and

$$\tilde{K}(m) = O\left(\ln \frac{1}{1-m}\right) = O\left(\ln \frac{1}{|\xi - \xi^0|}\right).$$

The approximate function $\tilde{E}(m)$ is non-singular at $m = 1$ due to $p_4(1) = 0$.

The case $m = 1$ takes place when $\xi = (r, z) \rightarrow \xi^0 = (r^0, z^0)$ and ξ^0 does not lie on the symmetry axis. In fact,

$$m = \frac{2b}{a+b} = \frac{4rr^0}{(r+r^0)^2 + (z-z^0)^2}, \quad \lim_{\xi \to \xi^0, r^0 \neq 0} m = 1, \quad \lim_{\xi \to \xi^0, r^0 \to 0} m = 0.$$

For the realisation of accurate numerical integrations let us study now the nature of the singularities in the kernel functions $a_1(\xi^0, \xi)$ and $a_2(\xi^0, \xi)$ for $\xi \to \xi^0$ after the approximation of the elliptic integrals.

Let us assume that the collocation point $\xi^0 = (r^0, z^0)$ lies on the boundary element Γ_j. We introduce new functions $\tilde{r}(t)$ and $\tilde{z}(t)$ on the boundary element

$$\Gamma_j = \{(r, z) \mid r = r(t), z = z(t), t \in [t_{j-1}, t_j]\}$$

such that

$$\tilde{r}(t) = \frac{r(t) - r^0}{t - t^0}, \quad \tilde{z}(t) = \frac{z(t) - z^0}{t - t^0},$$

where $t_{j-1} \leq t_0 \leq t_j$, $r^0 = r(t^0)$, $z^0 = z(t^0)$. We have that

$$\lim_{t \to t_0} \tilde{r}(t) = r'(t_0) \quad \text{and} \quad \lim_{t \to t_0} \tilde{z}(t) = z'(t_0).$$

The parametrisation of Γ_j should satisfy the requirement $r'(t)^2 + z'(t)^2 > 0$, hence we get

$$\lim_{t \to t_0} (\tilde{r}(t)^2 + \tilde{z}(t)^2) = r'(t^0)^2 + z'(t^0)^2 > 0. \tag{3.47}$$

In terms of the functions $\tilde{r}(t)$ and $\tilde{z}(t)$ we can write

$$|\xi - \xi^0|^2 = (t - t^0)^2 (\tilde{r}^2(t) + \tilde{z}^2(t)),$$

$$n_r(\xi^0) = \frac{-z'(t_0)}{\sqrt{r'(t_0)^2 + z'(t_0)^2}} = \lim_{t \to t^0} \frac{-\tilde{z}(t)}{\sqrt{\tilde{r}(t)^2 + \tilde{z}(t)^2}},$$

$$n_z(\xi^0) = \frac{r'(t_0)}{\sqrt{r'(t_0)^2 + z'(t_0)^2}} = \lim_{t \to t^0} \frac{\tilde{r}(t)}{\sqrt{\tilde{r}(t)^2 + \tilde{z}(t)^2}}.$$

Here it is assumed that the parameter t changes clock-wise over the boundary element Γ_j.

It follows that the kernel functions exhibit the following asymptotic behaviour

$$
\lim_{\xi \to \xi^0, r^0 \neq 0} a_1(\xi^0, \xi) = \frac{1}{2\pi} \lim_{m \to 1} \tilde{K}(m) = O\left(\ln \frac{1}{|\xi - \xi^0|}\right)
$$

$$
\lim_{\xi \to \xi^0, r^0 \neq 0} a_2(\xi^0, \xi) = -\frac{n_r(\xi^0)}{4\pi r^0} \lim_{m \to 1} \tilde{K}(m) +
$$

$$
\frac{n_r(\xi^0)}{4\pi r^0} \tilde{E}(1) \lim_{t \to t^0} \left(\frac{-(r + r^0)\tilde{r}}{(t - t^0)(\tilde{r}^2 + \tilde{z}^2)} + \frac{\tilde{z}^2}{\tilde{r}^2 + \tilde{z}^2}\right) +
$$

$$
\frac{n_z(\xi^0)}{2\pi r^0} \tilde{E}(1) \lim_{t \to t^0} \frac{-r\tilde{z}}{(t - t^0)(\tilde{r}^2 + \tilde{z}^2)}
$$

$$
= O\left(\ln \frac{1}{|\xi - \xi^0|}\right) + \frac{n_r(\xi^0)}{4\pi r^0} \tilde{E}(1) \lim_{t \to t^0} \frac{\tilde{z}^2}{\tilde{r}^2 + \tilde{z}^2} +
$$

$$
\frac{\tilde{E}(1)}{4\pi r^0} \lim_{t \to t^0} \left(\frac{-(r + r^0)\tilde{r}}{(t - t^0)(\tilde{r}^2 + \tilde{z}^2)} \frac{-\tilde{z}}{\sqrt{\tilde{r}^2 + \tilde{z}^2}} + \frac{-2r\tilde{z}}{(t - t^0)(\tilde{r}^2 + \tilde{z}^2)} \frac{\tilde{r}}{\sqrt{\tilde{r}^2 + \tilde{z}^2}}\right)
$$

$$
= O\left(\ln \frac{1}{|\xi - \xi^0|}\right) + \frac{n_r(\xi^0)}{4\pi r^0} \tilde{E}(1) \lim_{t \to t^0} \frac{\tilde{z}^2}{\tilde{r}^2 + \tilde{z}^2} - \frac{n_z(\xi^0)}{4\pi r^0} \tilde{E}(1) \lim_{t \to t^0} \frac{\tilde{r}\tilde{z}}{\tilde{r}^2 + \tilde{z}^2}.
$$

Two last terms contain no singularities because of condition (3.47), hence

$$
\lim_{\xi \to \xi^0, r^0 \neq 0} a_1(\xi^0, \xi) = O\left(\ln \frac{1}{|\xi - \xi^0|}\right) \qquad \lim_{\xi \to \xi^0, r^0 \neq 0} a_2(\xi^0, \xi) = O\left(\ln \frac{1}{|\xi - \xi^0|}\right).
$$

Both kernel functions $a_1(\xi^0, \xi)$ and $a_2(\xi^0, \xi)$ are weakly singular.

The situation $\xi \to \xi^0$, $r^0 = 0$, when $m = 0$, requires a special attention. It is an other source of kernel singularities. Actually we have

$$
\lim_{\xi \to \xi^0, r^0 = 0} a_1(\xi^0, \xi) = \frac{K(0)}{2\pi},
$$

$$
\lim_{\xi \to \xi^0, r^0 = 0} a_2(\xi^0, \xi) = -\frac{K(0)}{4\pi} + O\left(\frac{1}{r^0}\right).
$$

For the even-order collocation method the point ξ^0 lies in the middle of the boundary element. It means that r^0 does not belong to the symmetry axis, but can lye very close to it. The quantity $1/r^0$ then grows unboundendly, resulting in strong variation for the kernel function $a_2(\xi^0, \xi)$. To overcome the loss of accuracy for the numerical integration near the symmetry axis adaptive integration methods for computing boundary integrals is suggested in [50]. An adaptive integration is proposed by means of the numerical integration software package **Quadpack**, see [51]. Regular integrals are calculated by Gauss-Kronrod quadratures. The $(2n + 1)$-point Gauss-Kronrod quadrature is an n-point Gaussian rule augmented by a set of $n + 1$ points. The resulting formula integrates exactly a polynomial of degree $3n + 1$ for n even and $3n + 2$ for n odd (Gaussian rule is exact for the polynomial degree $2n - 1$). The numerical integration is estimated by measuring the difference between n-point Gauss quadrature and $(2n+1)$-point Gauss-Kronrod quadrature. A globally adaptive strategy is to bisect the interval with the largest error until it is less than a prescribed tolerance.

3.2 Boundary element method for magnetostatic problem

In this section we assume a constant material property of the fluid, i.e. $\mu_1 = const$. We apply the boundary element method to the magnetostatic problem (2.12)–(2.16).

Boundary integral equations

The boundary value problem (2.12)–(2.16) can be formulated in the form of integral equations (3.23) and (3.24) where additionally the interface conditions (2.13) should be taken into consideration.

For points lying on the boundary Γ we have the following boundary integral equations

$$\frac{1}{2}u_1(\xi^0) + (\mathbf{V}_{2,ax}u_1)(\xi^0) - (\mathbf{V}_{1,ax}q_1)(\xi^0) = 0, \tag{3.48}$$

$$\frac{1}{2}u_2(\xi^0) - (\mathbf{V}_{2,ax}u_2)(\xi^0) + (\mathbf{V}_{1,ax}q_2)(\xi^0) = z^0. \tag{3.49}$$

From the problem formulation we have the interface conditions

$$u_1 = u_2, \quad \mu_1 q_1 = q_2 \quad \text{on } \Gamma. \tag{3.50}$$

At first we apply the interface conditions to equation (3.49)

$$\frac{1}{2}u_1(\xi^0) - (\mathbf{V}_{2,ax}u_1)(\xi^0) + \mu_1(\mathbf{V}_{1,ax}q_1)(\xi^0) = z^0. \tag{3.51}$$

Using equations (3.48) and (3.51) we eliminate q_1 from the formulation. It gives us the boundary integral equation for the unknown function u_1 on the boundary Γ

$$\frac{1}{2}(\mu_1 + 1)u_1(\xi^0) + (\mu_1 - 1)(\mathbf{V}_{2,ax}u_1)(\xi^0) = z^0. \tag{3.52}$$

For the $\mu_1 > 1$, see (2.20), the equation (3.52) is a Fredholm integral equation of the second kind. When $\mu_1 = 1$, then from (3.52) we have $u_1(r,z) = z$. The sum of equations (3.48) and (3.51) results in

$$(\mu_1 - 1)(\mathbf{V}_{1,ax}q_1)(\xi^0) = z^0 - u_1(\xi^0). \tag{3.53}$$

For the given Dirichlet data the boundary integral equation (3.53) can be used to determine the unknown function q_1. Equation (3.53) is a Fredholm integral equation of the first kind for $\mu_1 \neq 1$.

Additionally, we write integral equations (3.52) and (3.53) in operator form

$$\begin{aligned}
(A_u u_1)(\xi) &= g_u(\xi) \quad \text{for } \xi \in \Gamma, \tag{3.54} \\
(A_q q_1)(\xi) &= g_q(\xi) \quad \text{for } \xi \in \Gamma, \tag{3.55}
\end{aligned}$$

where

$$\begin{aligned}
A_u &= \frac{1}{2}(\mu_1 + 1)\mathbf{I} + (\mu_1 - 1)\mathbf{V}_{2,ax}, \qquad g_u(\xi) = z, \\
A_q &= (\mu_1 - 1)\mathbf{V}_{1,ax}, \qquad g_q(\xi) = z - u_1(\xi).
\end{aligned}$$

Here $\mathbf{I}$ is an identity operator and $\xi = (r, z)$.

Discretisation by piecewise-constant collocation

We discretise integral equations (3.54) and (3.55) by the collocation method using piecewise constant approximation for unknown functions
Find $u_h \in S_0(T_n)$ and $q_h \in S_0(T_n)$ such that

$$\begin{aligned}
A_u u_h(\tilde{\xi}_i) &= g_u(\tilde{\xi}_i) \quad \text{for } \tilde{\xi}_i \in \tilde{\Xi}_n, \tag{3.56} \\
A_q q_h(\tilde{\xi}_i) &= g_q(\tilde{\xi}_i) \quad \text{for } \tilde{\xi}_i \in \tilde{\Xi}_n. \tag{3.57}
\end{aligned}$$

Following the idea of naive collocation, see [6, 7], as a collocation point $\tilde{\tilde{\xi}}_i$ we take a midpoint of the boundary element Γ_i (3.33). Let $\{\Phi_j\}_{j=1}^n$ denote a basis of the space $S_0(T_n)$ such that

$$\Phi_j(t) = 1, \ t \in [t_{j-1}, t_j]; \quad \Phi_j(t) = 0, \ \text{otherwise.}$$

Then functions u_h and q_h can be expressed as

$$u_h = \sum_{j=1}^n u_j \Phi_j, \quad q_h = \sum_{j=1}^n q_j \Phi_j$$

with unknowns $u_j = u(\tilde{\xi}_j)$ and $q_j = q(\tilde{\xi}_j)$, $j = \overline{1, n}$.

The equations (3.34) are equivalent to two quadratic systems of linear equations

$$\sum_{j=1}^n (A_u \Phi_j)(\tilde{\xi}_i) u_j = g_u(\tilde{\xi}_i), \quad i = \overline{1, n}, \tag{3.58}$$

$$\sum_{j=1}^n (A_q \Phi_j)(\tilde{\xi}_i) q_j = g_q(\tilde{\xi}_i), \quad i = \overline{1, n}, \tag{3.59}$$

for unknowns $u_1, \ldots, u_n$ and $q_1, \ldots, q_n$.

Numerical convergence of piecewise constant collocation

The first aim of numerical tests is to compare the experimental order of convergence (eoc) of the piecewise collocation method (3.56)-(3.57) with results predicted by the theory, see Remark 3.1.3. The other point of numerical testing is to analyse the influence of boundary approximation to the convergence of piecewise-constant collocation method (3.56)-(3.57) and to detect possible geometric instabilities due to an inexact representation of the geometry. For that reason we performed computations with the exact representation of the boundary and its piecewise linear and cubic spline approximations.

The magnetostatic problem (2.12)–(2.16) for the sphere, when $\mu_1 = const$, has the analytical solution, see [63]

$$u_1(r, z) = \frac{3}{(2 + \mu_1)} z \quad \text{for } (r, z) \in \Omega_1, \tag{3.60}$$

$$u_2(r, z) = z + \frac{(\mu_1 - 1)}{(2 + \mu_1)} \frac{z}{(r^2 + z^2)^{3/2}} \quad \text{for } (r, z) \in \Omega_2,$$

where the boundary Γ can be presented as

$$\Gamma = \{(r, z) \mid r = \sin t, \ z = \cos t, \ t \in [0, \pi/2]\}.$$

Taking into consideration that for the outward unit normal vector on Γ we have

$$n = (-z'(t), r'(t)) = (r(t), z(t)),$$

we can write

$$q_1(r, z) = \frac{\partial u_1}{\partial r} r + \frac{\partial u_1}{\partial z} z = \frac{3}{(2 + \mu_1)} z \quad \text{for } (r, z) \in \Gamma. \tag{3.61}$$

Let $\mu_1 = 6$ in our calculations. We apply the piecewise constant collocation (3.56)-(3.57) for $n = 4, 8, 16, 32$ and 64. A uniform grid T_n and a nonuniform one T_n^k are considered

$$T_n = \{t_j \mid t_j = jh, \ j = \overline{0, n}\}, \tag{3.62}$$

$$T_n^k = \{t_j \mid t_0 = 0; \ t_j = \frac{1}{2^{k+1-j}} h, \ j = \overline{1, k}; \ t_j = (j - k)h, \ j = \overline{k+1, k+n}\}, \tag{3.63}$$

where $h = \pi/(2n)$. The nonuniform discretisation T_n^k is based on the discretisation T_n with k times uniform refinements of the interval $[t_0, t_1]$. Fig. 3.2 presents uniform and nonuniform grid configurations for $n = 4$ and $k = 3$.
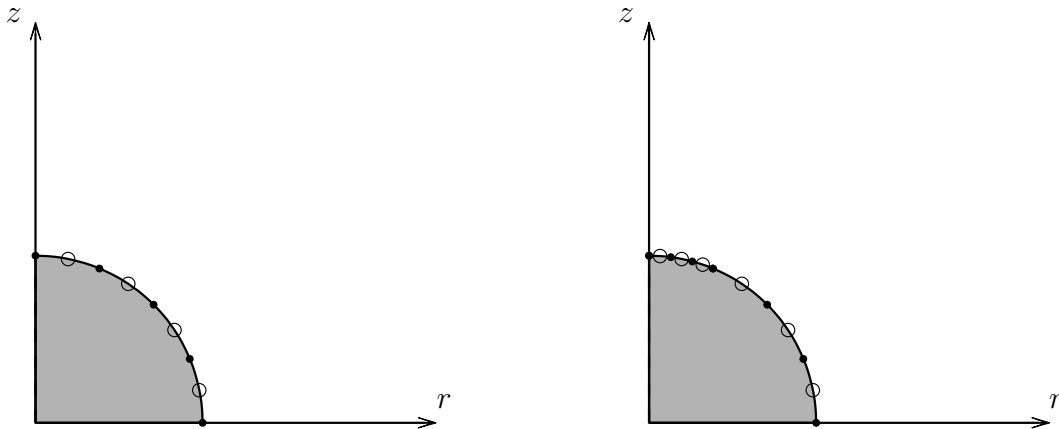

Figure 3.1: Grid configurations for T_4 (left) and T_4^3 (right): full markers are grid points, empty markers are collocation points.

To calculate the entries for the discrete systems (3.58), (3.59) we use a Gaussian quadrature formulas with 12 points for regular integrals and logarithmically weighted Gaussian formulas with 8 points for weakly singular integrals.

For a collocation method on the exact boundary Γ we define the error functions as

$$e_u(\xi) = u_1(\xi) - u_h(\xi), \quad e_q(\xi) = q_1(\xi) - q_h(\xi) \quad \text{for } \xi \in \Gamma.$$

For the case of an approximated boundary Γ_h we have

$$e_u(\xi) = u_1(\xi) - (u_h \circ F^{-1})(\xi), \quad e_q(\xi) = q_1(\xi) - (q_h \circ F^{-1})(\xi) \quad \text{for } \xi \in \Gamma,$$

where the mapping $F : \Gamma_h \to \Gamma$ is given by (3.29). We denote by $|| \cdot ||_2$ and $|| \cdot ||_\infty$ discrete analogs of the r-weighted L^2-norm and L^∞-norm, respectively, evaluated at the collocation points

$$||e_u||_2 = \left[\sum_{i=1}^n r(\tilde{t}_i)(u_1(\tilde{\xi}_i) - u_i)^2 |\xi_i - \xi_{i-1}| \right]^{1/2}, \quad ||e_u||_\infty = \max_{1 \le i \le n} |u_1(\tilde{\xi}_i) - u_i|,$$

$$||e_q||_2 = \left[\sum_{i=1}^n r(\tilde{t}_i)(q_1(\tilde{\xi}_i) - q_i)^2 |\xi_i - \xi_{i-1}| \right]^{1/2}, \quad ||e_q||_\infty = \max_{1 \le i \le n} |q_1(\tilde{\xi}_i) - q_i|.$$

The comparison of numerical results with the analytical solution on the exactly represented boundary Γ is illustrated in Table 3.1 and Table 3.2. Analysing the error for n between 4 and 64 we confirm the second order of convergence of the piecewise constant collocation (3.56), (3.57) on uniform T_n and nonuniform T_n^8 grids. It is one order higher than it was predicted by the theory for the L_2-norm, see Remark 3.1.3. However, the second order of convergence for piecewise constant collocation was proved in Theorem 4.6.17a in [31] for the L^∞-norm, calculated at the collocation points, provided some conditions for the integral operators and the assumption for the exact solution to be from the space $H^2(\Gamma)$. Additionally we can conclude that the nonuniform grid parametrisation (3.63) does not worsen the convergence.

Let us consider piecewise linear boundary approximation Γ_h^1 with the parametrisation (3.28) from the space $S_{2,1}$. The results of Tables 3.3 and 3.4 indicate the second order of convergence

n	$\|e_u\|_\infty$	eoc	$\|e_u\|_2$	eoc	$\|e_q\|_\infty$	eoc	$\|e_q\|_2$	eoc
4	.477e-3		.305e-3		.178e-2		.118e-2	
8	.155e-3	**1.625**	.936e-4	**1.704**	.601e-3	**1.568**	.357e-3	**1.719**
16	.432e-4	**1.840**	.254e-4	**1.884**	.167e-3	**1.851**	.964e-4	**1.888**
32	.113e-4	**1.932**	.657e-5	**1.948**	.435e-4	**1.939**	.250e-4	**1.949**
64	.289e-5	**1.970**	.167e-5	**1.976**	.111e-4	**1.966**	.635e-5	**1.976**

Table 3.1: Numerical convergence for the exact representation of Γ on uniform grids T_n.

n	$\|e_u\|_\infty$	eoc	$\|e_u\|_2$	eoc	$\|e_q\|_\infty$	eoc	$\|e_q\|_2$	eoc
4	.109e-2		.518e-3		.803e-2		.233e-2	
8	.235e-3	**2.216**	.108e-3	**2.257**	.214e-2	**1.906**	.448e-3	**2.379**
16	.530e-4	**2.150**	.263e-4	**2.042**	.549e-3	**1.964**	.103e-3	**2.127**
32	.125e-4	**2.084**	.663e-5	**2.001**	.139e-3	**1.984**	.254e-4	**2.015**
64	.303e-5	**2.044**	.167e-5	**1.985**	.348e-4	**1.994**	.637e-5	**1.992**

Table 3.2: Numerical convergence for the exact representation of Γ on nonuniform grids T_n^8.

for all situations except $\|e_q\|_\infty$. Numerically we got the first order for $\|e_q\|_\infty$ on the nonuniform grids. The maximum deviation from the exact solution takes place at the collocation points lying near the axis of revolution Oz. It follows that the piecewise linear boundary approximation decreases the order of convergence at the nonuniform grids (3.63).

n	$\|e_u\|_\infty$	eoc	$\|e_u\|_2$	eoc	$\|e_q\|_\infty$	eoc	$\|e_q\|_2$	eoc
4	.157e-1		.926e-2		.168e-2		.110e-2	
8	.413e-2	**1.927**	.240e-2	**1.946**	.520e-3	**1.696**	.310e-3	**1.829**
16	.105e-2	**1.975**	.609e-3	**1.981**	.138e-3	**1.909**	.800e-4	**1.951**
32	.265e-3	**1.991**	.153e-3	**1.993**	.353e-4	**1.972**	.202e-4	**1.984**
64	.663e-4	**1.996**	.383e-4	**1.997**	.893e-5	**1.993**	.508e-5	**1.994**

Table 3.3: Convergence for the piecewise-linear boundary Γ_h^1 on uniform grids T_n.

n	$\|e_u\|_\infty$	eoc	$\|e_u\|_2$	eoc	$\|e_q\|_\infty$	eoc	$\|e_q\|_2$	eoc
4	.132e-1		.828e-2		.190e-1		.500e-2	
8	.396e-2	**1.738**	.234e-2	**1.825**	.951e-2	**1.002**	.133e-2	**1.911**
16	.104e-2	**1.929**	.604e-3	**1.951**	.468e-2	**1.022**	.342e-3	**1.959**
32	.264e-3	**1.979**	.153e-3	**1.986**	.231e-2	**1.016**	.868e-4	**1.979**
64	.662e-4	**1.993**	.383e-4	**1.995**	.115e-2	**1.009**	.218e-4	**1.990**

Table 3.4: Convergence for the piecewise-linear boundary Γ_h^1 on nonuniform grids T_n^8.

Let us improve the smoothness property of boundary approximation and consider the boundary approximation by a cubic spline Γ_h^3 defined in the space $S_{4,3}$. The results of Tables 3.5 and 3.6 show the second order of convergence for the cubic spline approximation of the boundary even on the nonuniform grids.

Finally we present all numerical results in Figs. 3.2 and 3.3. The figures illustrate that the results of the calculations for the exact boundary and for its cubic spline approximation coincide nearly everywhere.

n	$\|e_u\|_\infty$	eoc	$\|e_u\|_2$	eoc	$\|e_q\|_\infty$	eoc	$\|e_q\|_2$	eoc
4	.548e-3		.359e-3		.180e-2		.118e-2	
8	.159e-3	**1.783**	.962e-4	**1.901**	.610e-3	**1.558**	.357e-3	**1.721**
16	.433e-4	**1.878**	.255e-4	**1.915**	.168e-3	**1.861**	.964e-4	**1.888**
32	.113e-4	**1.936**	.658e-5	**1.954**	.436e-4	**1.945**	.250e-4	**1.949**
64	.289e-5	**1.971**	.167e-5	**1.977**	.112e-4	**1.969**	.635e-5	**1.976**

Table 3.5: Convergence for the cubic spline boundary Γ_h^3 for uniform grids T_n.

$n-k$	$\|e_u\|_\infty$	eoc	$\|e_u\|_2$	eoc	$\|e_q\|_\infty$	eoc	$\|e_q\|_2$	eoc
4	.108e-2		.557e-3		.818e-2		.235e-2	
8	.235e-3	**2.205**	.111e-3	**2.331**	.216e-2	**1.918**	.449e-3	**2.385**
16	.530e-4	**2.148**	.264e-4	**2.070**	.552e-3	**1.970**	.103e-3	**2.132**
32	.125e-4	**2.083**	.663e-5	**1.990**	.139e-3	**1.988**	.254e-4	**2.016**
64	.303e-5	**2.044**	.167e-5	**1.986**	.349e-4	**1.996**	.637e-5	**1.993**

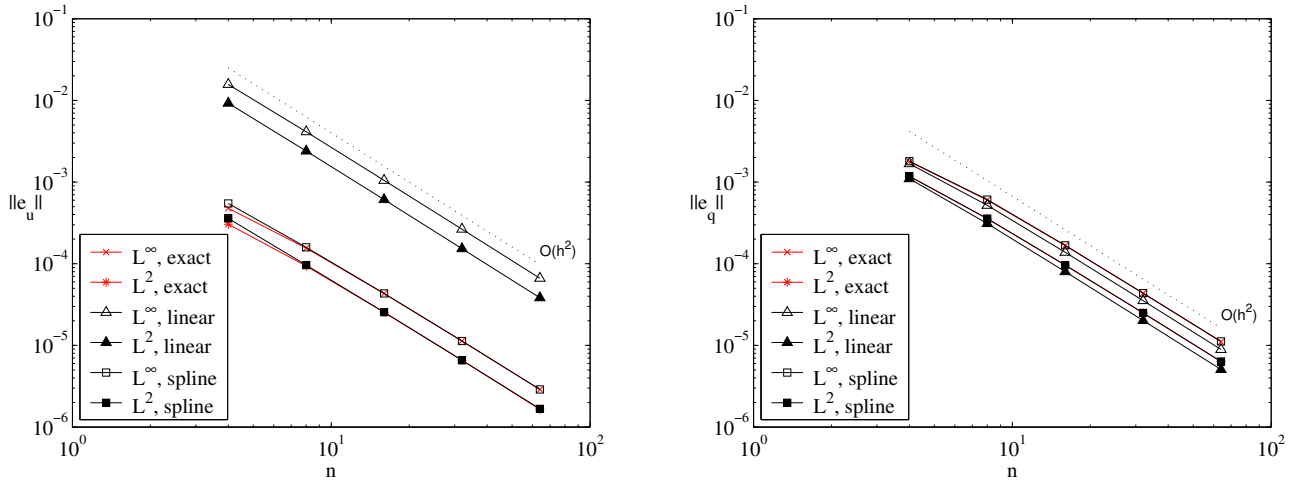Table 3.6: Convergence for the cubic spline boundary Γ_h^3 for nonuniform grids T_n^8.

Figure 3.2: Accuracy of numerical calculations on the uniform grids.
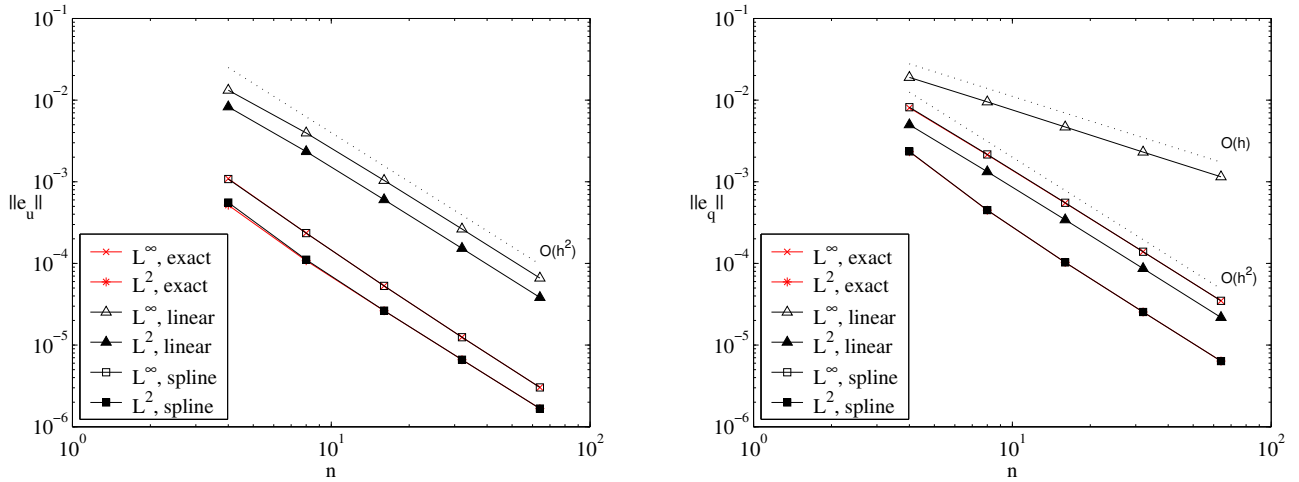

Figure 3.3: Accuracy of numerical calculations on the nonuniform grids.

3.3 Finite element method for the magnetostatic problem

3.3.1 Continuous formulation

In Section 2.3 we assumed that the domains D_1 and D_2, defined in $\mathrm{I\!R}^3$, are invariant by rotation around the z-axis and generated by rotating two-dimensional meridian domains Ω_1 and Ω_2 such that

$$\bar{\Omega} = \bar{\Omega}_1 \cup \bar{\Omega}_2 = \mathrm{I\!R}^+ \times \mathrm{I\!R}, \quad \Omega_1 \cap \Omega_2 = \emptyset, \quad \partial\Omega_1 \cap \partial\Omega_2 = \Gamma.$$

For computational purposes we restrict the unbounded domain Ω_2 by asymptotic boundaries $r = r_{right}$ and $z = z_{top}$. The distances of these boundaries from the free surface are finite but large enough to ensure that the magnetic field there is uniform. The dimensionless magnetostatic problem (2.12)-(2.16) takes the form

$$-\nabla \cdot (\mu(\xi, |\nabla u|)\nabla u) = 0, \quad \text{in } \Omega, \quad \mu = \begin{cases} \mu_1(|\nabla u|) & \text{for } \xi \in \Omega_1, \\ 1 & \text{for } \xi \in \Omega_2, \end{cases} \tag{3.64}$$

$$u = z \quad \text{for } r = r_{right}, \quad u = z_{top} \quad \text{for } z = z_{top}, \tag{3.65}$$

$$u = 0, \quad u = 0 \quad \text{for } z = 0, \tag{3.66}$$

$$\frac{\partial u}{\partial n} = 0 \quad \text{for } r = 0, \tag{3.67}$$

$$u_1 = u_2, \quad \mu_1 \frac{\partial u_1}{\partial n} = \frac{\partial u_2}{\partial n} \quad \text{on } \Gamma, \tag{3.68}$$

where

$$\mu_1(|\nabla u|) = 1 + 3\chi \frac{P(\gamma|\nabla u|)}{\gamma|\nabla u|}, \quad P(t) = \coth(t) - \frac{1}{t}, \quad \gamma = \frac{3\chi H_0}{M_s}. \tag{3.69}$$

We set for calculations $r_{right} = z_{top} = 20$.

Let us consider the boundary of the computational domain Ω as a union of the boundary

$$\Gamma_D = \partial\Omega \cap \{\{z = z_{top}\} \cup \{r = r_{right}\} \cup \{z = 0\}\}$$

with the Dirichlet condition $u = u_D$, corresponding to conditions (3.65) and (3.66), and the boundary on the z-axis

$$\Gamma_N = \partial\Omega \cap \{r = 0\}$$

with the Neumann boundary condition (3.67). Then we have

$$\partial\Omega = \Gamma_D \cup \Gamma_N.$$

Let us denote by X the space of axisymmetric functions

$$X = \{v \in L^2(D) \mid v \text{ is an axisymmetric function with respect to the } z\text{-axis}\}.$$

For any function $v \in X$ there exists a function $\tilde{v}$ defined on Ω such that

$$\tilde{v}(r, z) = v(r \cos\theta, z \sin\theta, z)$$

for $(r, z) \in \Omega$ and any $\theta \in [0, 2\pi]$. By the substitution we have

$$\int_D v^2(x, y, z)dxdydz = 2\pi \int_\Omega \tilde{v}^2(r, z)rdrdz.$$

It follows that the function $\tilde{v}$ belongs to the weighted space with the measure $rdrdz$

$$L_r^2(\Omega) = \left\{ \tilde{v} \mid \int_\Omega \tilde{v}^2(r, z)rdrdz < \infty \right\}$$

with an inner product

$$(\tilde{u}, \tilde{v}) = \int_\Omega \tilde{u}\tilde{v}rdrdz \quad \text{for } u, v \in L_r^2(\Omega).$$

For smooth functions the variable transformation leads to

$$\frac{\partial v}{\partial x} = \frac{\partial \tilde{v}(r(x, y), z)}{\partial x} = \frac{\partial \tilde{v}}{\partial r}\frac{\partial r}{\partial x} = \frac{\partial \tilde{v}}{\partial r}\cos\theta,$$

$$\frac{\partial v}{\partial y} = \frac{\partial \tilde{v}(r(x, y), z)}{\partial y} = \frac{\partial \tilde{v}}{\partial r}\frac{\partial r}{\partial y} = \frac{\partial \tilde{v}}{\partial r}\sin\theta,$$

$$\frac{\partial v}{\partial z} = \frac{\partial \tilde{v}}{\partial z}.$$

We have then that

$$\begin{aligned}
||v||_V^2 &= \int_D \left(v^2 + \left(\frac{\partial v}{\partial x}\right)^2 + \left(\frac{\partial v}{\partial y}\right)^2 + \left(\frac{\partial v}{\partial z}\right)^2 \right) dxdydz \\
&= 2\pi \int_\Omega \left(\tilde{v}^2 + \left(\frac{\partial \tilde{v}}{\partial r}\right)^2 + \left(\frac{\partial \tilde{v}}{\partial z}\right)^2 \right) rdrdz = 2\pi ||\tilde{v}||_{V_r}^2,
\end{aligned}$$

where $v \in V(D) = H^1(D) \cap X$ and $\tilde{v}$ belongs to the weighted Sobolev space

$$V_r(\Omega) = \{\tilde{v} \mid \tilde{v} \in L_r^2(\Omega), \nabla\tilde{v} \in L_r^2(\Omega)\}.$$

The space $V(D)$ is isomorphic to $V_r(\Omega)$, see Theorem II.2.1 in [16].

We define the space

$$W_r(\Omega) = \{v \in V_r(\Omega) \mid v|_{\Gamma_D} = 0\}.$$

To get the weak formulation for the problem (3.64)-(3.68), we multiply equation (3.64) by a weight function r and by an arbitrary function $v \in W_r(\Omega)$, integrate it over Ω and transform by the first Green formula. The weak formulation of (3.64)-(3.68) reads

Find $u_h \in V_r(\Omega)$ such that $u_h - u^* \in W_r(\Omega)$ and

$$(\mu(\xi, |\nabla u|)\nabla u, \nabla v) = 0 \quad \text{for any } v \in W_r(\Omega). \tag{3.70}$$

Here u^* is assumed to be smooth such that $u^*|_{\Gamma_D} = u_D$.

Solvability of the variational problem

The classical approach for deriving an assertion about the existence and uniqueness of a weak solution for the nonlinear boundary value problem consists in the transformation of the problem to an operator equation

$$Tu = F, \quad T : V \to V^*,$$

and further application of the theory of monotone operators, namely, the Browder's Theorem, see for instance [37]. If we verify that the operator T is bounded, demicontinuous, monotone and coercive, then the existence of a solution $u \in V$ of the operator equation and consequently, also the existence of the corresponding weak solution are guaranteed. This approach was studied for the case of weighted Sobolev spaces in [37].

Let us consider nonlinear differential operators of order $2k$

$$(Nu)(x) = \sum_{\alpha \in S} (-1)^{|\alpha|} D^\alpha a_\alpha (x; \delta_S u(x)) \tag{3.71}$$

with

$$\delta_S u(x) = \{D^\beta u(x); \ \beta \in S\}.$$

where $a_\alpha = a_\alpha(x;\xi)$ are given functions defined on $\Omega \times \mathbb{R}^m$, $\Omega \subset \mathbb{R}^N$, $\xi = \{\xi_\beta; \ \beta \in S\} \in \mathbb{R}^m$. The variable S denotes a subset of the set $\{\alpha; \ |\alpha| \leq k\}$ of all N-dimensional multiindices of length at most k. It contains the zero multiindex and at least one multiindex of the length k. The number of elements of the set S equals m.

We define the weighted Sobolev space $W^{k,2}(\Omega, w)$ as the set of all functions u such that

$$||u; W^{k,2}(\Omega, w)||^2 = \sum_{\alpha \in S} \int_\Omega |D^\alpha u(x)|^2 w(x) dx < \infty,$$

where the weight function $w(x)$ is measurable and positive almost everywhere in Ω such that

$$w(x)^{-1} \in L^1_{loc}(\Omega) \quad \text{and} \quad w(x) \in L^1_{loc}(\Omega).$$

Additionally we introduce a space $W_0^{k,2}(\Omega, w)$ as the closure of $C_0^\infty(\Omega)$ with respect to the norm $||\cdot; W^{k,2}(\Omega, w)||$.

Let a function $u_0 \in W^{k,2}(\Omega, w)$ and a functional $F \in [W_0^{k,2}(\Omega, w)]^*$ from the dual space to $W_0^{k,2}(\Omega, w)$ be given. A function $u \in W^{k,2}(\Omega, w)$ is a weak solution of the Dirichlet problem for the operator (3.71), if

$$u - u_0 \in W_0^{k,2}(\Omega, w) \quad \text{and}$$

$$\sum_{\alpha \in S} \int_\Omega a_\alpha(x; \delta_S u(x)) D^\alpha v(x) dx = <F, v> \quad \text{for any } v \in W_0^{k,2}(\Omega, w). \tag{3.72}$$

Theorem 3.3.1 (Theorem 50.2 in [37], existence and uniqueness of weak solution)
Let the coefficients $a_\alpha = a_\alpha(x;\xi)$ of the nonlinear differential operator (3.71) satisfy the Carathéodory condition, growth condition, monotonicity condition and coercivity condition:

$$a_\alpha(x;\xi) \text{ are measurable in } x \text{ for every } \xi \in \mathbb{R}^m \text{ and continuous in } \xi \text{ for a.e. } x \in \Omega; \tag{3.73}$$

$$|a_\alpha(x;\xi)| \leq w^{1/2}(x) \left(g_\alpha(x) + c_\alpha \sum_{\beta \in S} |\xi_\beta| w^{1/2}(x) \right), \tag{3.74}$$

where $g_\alpha \in L^2(\Omega)$ and $c_\alpha \geq 0$;

$$\sum_{\alpha \in S} (a_\alpha(x;\xi) - a_\alpha(x;\eta))(\xi_\alpha - \eta_\alpha) \geq 0 \tag{3.75}$$

for a.e. $x \in \Omega$ and all ξ, $\eta \in \mathbb{R}^m$;

$$\sum_{\alpha \in S} a_\alpha(x;\xi)\xi_\alpha \geq c_1 \sum_{\alpha \in S} w(x)\xi_\alpha^2 \tag{3.76}$$

for a.e. $x \in \Omega$ and all $\xi \in \mathbb{R}^m$ and $c_1 > 0$.

Then there exists at least one weak solution of the Dirichlet problem (3.72).

If the inequality in (3.75) is strict for $\xi \neq \eta$, then the weak solution is uniquely determined.

Let us show that the magnetostatic equation (3.64) can be written as the nonlinear operator of the form (3.71). After multiplying equation (3.64) by the function r we get

$$-\frac{\partial}{\partial r}\left(r\mu(\xi, |\nabla u|)\frac{\partial u}{\partial r}\right) - \frac{\partial}{\partial z}\left(r\mu(\xi, |\nabla u|)\frac{\partial u}{\partial z}\right) = 0 \quad \text{in } \Omega.$$

We obtain that the magnetostatic equation corresponds to (3.71), where

$$x = (r,z), \quad k = 1, \quad S = \{(0,1),(1,0)\}, \quad \delta_S = \left\{\frac{\partial u}{\partial r}, \frac{\partial u}{\partial z}\right\},$$

$$\xi = \{\xi_{(0,1)}, \xi_{(1,0)}\}, \quad \xi_{(0,1)} = \frac{\partial u}{\partial r}, \quad \xi_{(1,0)} = \frac{\partial u}{\partial z},$$

$$a_{(0,1)} = r\mu(x, |\xi|)\xi_{(0,1)}, \quad a_{(1,0)} = r\mu(x, |\xi|)\xi_{(1,0)}.$$

For the convenience we define $\xi_1 := \xi_{(0,1)}$, $\xi_2 := \xi_{(1,0)}$, $a_1 := a_{(0,1)}$, $a_2 := a_{(1,0)}$. The weighted Sobolev space $W^{k,2}(\Omega, w)$ with the weight function $w = r$ corresponds to the space $V_r(\Omega)$.

The solvability in Theorem 3.3.1 was stated for the Dirichlet problem. For the magnetostatic problem (3.64)-(3.68) we have a mixed Dirichlet-Neumann situation and transition conditions (3.68). In [37] an interpretation of the condition

$$u - u_0 \in W_0^{k,2}(\Omega, w)$$

was discussed. As an example the Laplace operator with the weight function $w = r$ was taken. The following facts were asserted. The condition $u - u_0 \in W_0^{k,2}(\Omega, r)$ means that on the boundary $\partial\Omega \setminus \{r = 0\}$ we have $u = u_0$ and on the boundary $r = 0$ no condition imposed on u. It allows us to assume that by setting the Neumann condition $\partial u/\partial n = 0$ over the boundary, where the weight function vanishes, we stay still in the frame of Theorem 3.3.1. The Dirichlet problem with discontinuous coefficients results in the weak formulation of the form (3.72) for $\Omega = \cup\Omega_i$ with continuous coefficients at every subdomain Ω_i. It follows that Theorem 3.3.1 can be applied for problems with discontinuous coefficients, provided every of conditions (3.73)-(3.76) to satisfy at all subdomains Ω_i.

In order to examine the solvability of the variational problem (3.70) we apply the results established in Theorem 3.3.1. Let us remind the properties of the function $\mu_1(t) = 1 + 3\chi P(\gamma t)/(\gamma t)$

$$1 \leq \mu_1(t) \leq 1 + \chi \quad \text{for } t \geq 0; \quad P(t) \geq 0 \text{ and } P'(t) \geq 0 \quad \text{for } t \geq 0. \tag{3.77}$$

Now we verify whether coefficients $a_1(x, |\xi|)$ and $a_2(x, |\xi|)$ satisfy conditions (3.73)-(3.76). We have that the functions $a_i = r\mu(x, |\xi|)\xi_i$ are measurable in x for every $\xi \in \mathbb{R}^2$ and continuous in ξ as the composition of continuous functions for $x \in \Omega_1 \cup \Omega_2$. The growth condition is satisfied with $g_\alpha(x) \equiv 1 + \chi$ and $c_\alpha = 1 + \chi$

$$|a_i(x, |\xi|)| = r\mu(x, |\xi|)|\xi_i| \le r(1 + \chi)|\xi_i| \le r^{1/2}(1 + \chi)\left(1 + \sum_{j=1}^{2} r^{1/2}|\xi_j|\right).$$

Next we show that the monotonicity condition (3.75) is satisfied. Let $\xi, \eta \in \mathbb{R}^2$ be arbitrary. We set $\zeta = \xi - \eta$ and

$$\phi(t) = r\frac{P(\gamma|\eta + t\zeta|)}{\gamma|\eta + t\zeta|}(\eta + t\zeta, \zeta), \quad t \in [0, 1].$$

$$\begin{aligned}
\phi'(t) &= rP'(\gamma|\eta + t\zeta|)\frac{(\eta + t\zeta, \zeta)^2}{|\eta + t\zeta|^2} - r\frac{P(\gamma|\eta + t\zeta|)}{\gamma|\eta + t\zeta|^3}(\eta + t\zeta, \zeta)^2 + r\frac{P(\gamma|\eta + t\zeta|)}{\gamma|\eta + t\zeta|}(\zeta, \zeta) \\
&= rP'(\gamma|\eta + t\zeta|)\frac{(\eta + t\zeta, \zeta)^2}{|\eta + t\zeta|^2} + r\frac{P(\gamma|\eta + t\zeta|)}{\gamma|\eta + t\zeta|}\left(-\frac{(\eta + t\zeta, \zeta)^2}{|\eta + t\zeta|^2} + (\zeta, \zeta)\right) \\
&\ge rP'(\gamma|\eta + t\zeta|)\frac{(\eta + t\zeta, \zeta)^2}{|\eta + t\zeta|^2} \ge 0.
\end{aligned}$$

To get the relation we used the fact that the function $P(t)$ is nonnegative and $P'(t) \ge 0$.

For the left-hand side of the monotonicity condition we have

$$r(\mu(x, |\xi|)\xi - \mu(x, |\eta|)\eta, \zeta) = r(\zeta, \zeta) + \phi(1) - \phi(0) = r(\zeta, \zeta) + \phi'(t_0) \ge r(\zeta, \zeta) > 0 \text{ for } x \in \Omega_1, \xi \ne \eta,$$

$$r(\mu(x, |\xi|)\xi - \mu(x, |\eta|)\eta, \zeta) = r(\zeta, \zeta) > 0 \quad \text{for } x \in \Omega_2, \ \xi \ne \eta.$$

The existence of $t_0 \in (0, 1)$ is guaranteed by the Mean Value Theorem. Hence the monotonicity condition (3.75) is satisfied.

Finally we have the coercivity condition (3.76) to be fulfilled

$$r\mu(x, |\xi|)(\xi, \xi) \ge r(\xi, \xi) \quad \text{for all } x \in \Omega \text{ and all } \xi \in \mathbb{R}^2.$$

Therefore, according to Theorem 3.3.1, there exists a uniquely determined weak solution of the magnetostatic problem (3.64)-(3.68).

3.3.2   Discrete formulation

Let us denote by Ω_h^1 and Ω_h^2 polygonal approximations of the domains Ω_1 and Ω_2, respectively, such that

$$\partial\Omega_h^1 \cap \partial\Omega_h^2 = \Gamma_h,$$

where Γ_h is a piecewise linear approximation of the boundary Γ. Let $\mathcal{T}_h^1$ and $\mathcal{T}_h^2$ be regular triangulations of $\bar{\Omega}_h^1$ and $\bar{\Omega}_h^2$, respectively, see for instance [23], such that

$$\bar{\Omega}_h^1 = \bigcup_{T \in \mathcal{T}_h^1} T, \quad \bar{\Omega}_h^2 = \bigcup_{T \in \mathcal{T}_h^2} T,$$

where T is a triangular element with a diameter h_T and $h = \max_{T \in \mathcal{T}_h} h_T$.

For the discretisation of the problem (3.70) we use conforming finite dimensional spaces

$$
\begin{aligned}
V_h(\Omega_h) &= \{v_h \in V_r(\Omega_h) \cap C(\bar{\Omega}_h) \mid v_h \text{ is linear on each } T \in \mathcal{T}_h^1 \cup \mathcal{T}_h^2\}, \\
W_h(\Omega_h) &= \{v_h \in W_r(\Omega_h) \cap C(\bar{\Omega}_h) \mid v_h \text{ is linear on each } T \in \mathcal{T}_h^1 \cup \mathcal{T}_h^2\}.
\end{aligned}
$$

where $\bar{\Omega}_h = \bar{\Omega}_h^1 \cup \bar{\Omega}_h^2$. An approximate solution u_h is sought in the space of linear conforming triangular elements. We apply a standard Galerkin approach to the problem (3.70). The discrete problem reads: Find $u_h \in V_h(\Omega_h)$ such that $u_h - u^* \in W_h(\Omega_h)$ and

$$
(\mu(\xi, |\nabla u_h|)\nabla u_h, \nabla v_h) = 0 \quad \text{for all } v_h \in W_h(\Omega_h). \tag{3.78}
$$

Convergence

Study of the convergence of the finite element method should take into account the problem formulation in cylindrical coordinates, approximation of the domain Ω by Ω_h and numerical integration for the semilinear form.

For two-dimensional problems the study of the finite element solution of nonlinear second order elliptic boundary value problems with discontinuous coefficients was presented in [26, 81] in the case of mixed Dirichlet-Neumann boundary conditions. The domain Ω is approximated by a polygonal one, conforming piecewise linear triangular elements are used and the integrals are evaluated by numerical quadratures. With the assumptions that the corresponding operator is strongly monotone and Lipschitz-continuous and that $u \in H^1(\Omega)$ the convergence of the method is proved. Under the additional assumption that u is piecewise of class $H^{1+\varepsilon}$, $0 < \varepsilon \le 1$ in [81] (u is piecewise of class $H^2(\Omega)$ in [26]) the convergence $O(h^\varepsilon)$ in [81] ($O(h)$ in [26]) is derived.

Iterative solution of the discrete problem

There are several ways to solve the discrete nonlinear problem (3.78). One possibility is to reduce this problem to a sequence of linear problems by the fixed-point method. Let $u_h^0 \in V_h$ be arbitrary. Suppose that $u_h^k \in V_h$, $k \in \{0, 1, \dots\}$ are known. Then $u_h^{k+1} \in V_h$ is determined as the solution of the linear problem

$$
(\mu(|\nabla u_h^k|)\nabla u_h^{k+1}, \nabla v_h) = 0 \quad \text{for all } v_h \in W_h. \tag{3.79}
$$

To solve the linear system, corresponding (3.79), we apply an F-cycle of a geometric multigrid method with one pre-smoothing and one post-smoothing step. For details on the multigrid method see [29]. As a smoother we use a Symmetric Successive Overrelaxation Method (SSOR), see for instance [64], with a relaxation parameter equals one. The iterative process continues until the defect of the linear system, when all quantities are taken at the k-th iteration, will be smaller than ε (generally 10^{-8}). Practically only a few steps (2-10) of the iterative process have to be performed to solve the linear system. Initially $\mu_1(|\nabla u_h^0|)$ set to be $1 + \chi$. It is the only quantity required to be defined from the previous iteration.

The software package **MooNMD**, see [36], was used for numerical simulations.

3.4   Boundary element-finite element coupling

It is well known, that a boundary element method (BEM) is suited to problems in the domain extending to infinity but is usually restricted to regions in which the governing equations are linear. On the other hand, the finite element method (FEM) is restricted to problems in bounded domains but is applicable to problems in which the material properties are not necessarily homogeneous and nonlinearity may occur.

For the numerical modeling of the magnetostatic problem (2.12)-(2.16) a coupled strategy of finite element and boundary element methods seems to be the favorable choice. A boundary integral formulation in the unbounded air domain satisfies the boundary condition for the magnetic field at infinity while with a finite element method we can resolve non-linearities inside of the fluid. Following the idea in [78], we apply the coupling of the collocation BEM in the exterior domain Ω_2 and the Galerkin FEM in the interior domain Ω_1 for the magnetostatic problem (2.12)-(2.16).

3.4.1 Continuous formulation

We denote by $D_1 \subset \mathbb{R}^3$ a bounded domain, see Fig. 2.1, by $\Omega_1 \subset \mathbb{R}^2$ a meridian section of D_1 and by Γ a meridian line of D_1, see Fig. 2.2. Let us consider the boundary of Ω_1 as a union of the boundary Γ_D with the Dirichlet condition (2.16)

$$u = 0 \quad \text{on } \Gamma_D,$$

the boundary Γ_N with the Neumann condition on the z-axis

$$\frac{\partial u}{\partial n} = 0 \quad \text{on } \Gamma_N$$

and the boundary Γ with the transmission conditions (2.13)

$$u_1 = u_2, \quad \mu_1 \frac{\partial u_1}{\partial n} = \frac{\partial u_2}{\partial n} \quad \text{on } \Gamma.$$

We have that

$$\partial \Omega_1 = \Gamma_D \cup \Gamma_N \cup \Gamma.$$

In Section 3.1 we formulated the following boundary integral equation for the Laplace equation in the exterior domain Ω_2, see (3.51)

$$\frac{1}{2}u(\xi^0) - (\mathbf{V}_{2,ax}u)(\xi^0) + (\mathbf{V}_{1,ax}\mu_1(|\nabla u|)q)(\xi^0) = z^0 \quad \text{for } \xi^0 \in \Gamma. \tag{3.80}$$

Here u denotes the axisymmetric potential, $q = \partial u/\partial n$ with the normal vector outer for Ω_1.

We reformulate the magnetostatic problem (2.12)-(2.16) as the nonlocal boundary value problem for (u, q) in Ω_1. The problem reads

$$-\nabla \cdot (\mu_1(|\nabla u|)\nabla u) = 0 \quad \text{in } \Omega_1, \tag{3.81}$$

$$(\frac{1}{2}\mathbf{I} - \mathbf{V}_{2,ax})u + \mathbf{V}_{1,ax}(\mu_1(|\nabla u|)q) = z, \quad \frac{\partial u}{\partial n} = q \quad \text{on } \Gamma, \tag{3.82}$$

$$u = 0 \quad \text{on } \Gamma_D, \tag{3.83}$$

$$\frac{\partial u}{\partial n} = 0 \quad \text{on } \Gamma_N. \tag{3.84}$$

The nonlocal boundary value value problem (3.81)-(3.84) is equivalent to the problem (2.12)-(2.16) in the sense that if (u, q) satisfies (3.81)-(3.84) and if we set from (3.24)

$$u(\xi^0) = (\tilde{\mathbf{V}}_{2,ax}u)(\xi^0) - (\tilde{\mathbf{V}}_{1,ax}q)(\xi^0) + z^0 \quad \text{for } \xi^0 \in \Omega_2,$$

then u satisfies (2.12)-(2.16) with $\partial u/\partial n = q$ on Γ.

Let us denote by X the space of axisymmetric functions

$$X = \{v \in L^2(D) \mid v \text{ is an axisymmetric function with respect to the } z\text{-axis}\}.$$

For any function $v \in X$ there exists a function $\tilde{v}$ defined on Ω_1 such that

$$\tilde{v}(r, z) = v(r \cos \theta, z \sin \theta, z)$$

for $(r, z) \in \Omega_1$ and any $\theta \in [0, 2\pi]$. By the substitution we have

$$\int_{D_1} v^2(x, y, z) dx dy dz = 2\pi \int_{\Omega_1} \tilde{v}^2(r, z) r dr dz.$$

It follows that the function $\tilde{v}$ belongs to the weighted space with the measure $r dr dz$

$$L_r^2(\Omega_1) = \left\{ \tilde{v} \mid \int_{\Omega_1} \tilde{v}^2(r, z) r dr dz < \infty \right\}$$

with an inner product

$$(\tilde{u}, \tilde{v})_{\Omega_1} = \int_{\Omega_1} \tilde{u} \tilde{v} r dr dz \quad \text{for } u, v \in L_r^2(\Omega_1).$$

For smooth functions $v \in X$ the variable transformation leads to

$$\frac{\partial v}{\partial x} = \frac{\partial \tilde{v}(r(x, y), z)}{\partial x} = \frac{\partial \tilde{v}}{\partial r} \frac{\partial r}{\partial x} = \frac{\partial \tilde{v}}{\partial r} \cos \theta,$$

$$\frac{\partial v}{\partial y} = \frac{\partial \tilde{v}(r(x, y), z)}{\partial y} = \frac{\partial \tilde{v}}{\partial r} \frac{\partial r}{\partial y} = \frac{\partial \tilde{v}}{\partial r} \sin \theta,$$

$$\frac{\partial v}{\partial z} = \frac{\partial \tilde{v}}{\partial z}.$$

Then we have that

$$\begin{aligned}
||v||_V^2 &= \int_D \left(v^2 + \left(\frac{\partial v}{\partial x} \right)^2 + \left(\frac{\partial v}{\partial y} \right)^2 + \left(\frac{\partial v}{\partial z} \right)^2 \right) dx dy dz \\
&= 2\pi \int_\Omega \left(\tilde{v}^2 + \left(\frac{\partial \tilde{v}}{\partial r} \right)^2 + \left(\frac{\partial \tilde{v}}{\partial z} \right)^2 \right) r dr dz = 2\pi ||\tilde{v}||_{V_r}^2,
\end{aligned}$$

where $v \in V(D) = H^1(D) \cap X$ and $\tilde{v}$ belongs to the weighted Sobolev space

$$V_r(\Omega) = \{\tilde{v} \mid \tilde{v} \in L_r^2(\Omega), \nabla \tilde{v} \in L_r^2(\Omega)\}.$$

The space $V(D_1)$ is isomorphic to $V_r(\Omega_1)$, see Theorem II.2.1 in [16].

We define the following spaces

$$\begin{aligned}
W_r(\Omega_1) &= \{v \in V_r(\Omega_1) \mid v|_{\Gamma_D} = 0\}, \\
Q_r(\Gamma) &= H^{-1/2}(\Gamma) \cap L_r^2(\Gamma), \\
\mathcal{H} &= W_r(\Omega_1) \times Q_r(\Gamma).
\end{aligned}$$

Let $\langle \cdot, \cdot \rangle_\Gamma$ denote the duality paring between spaces $H^{1/2}(\Gamma) \cap L_r^2(\Gamma)$ and $Q_r(\Gamma)$ with respect to the $L_r^2(\Gamma)$-inner product

$$\langle u, v \rangle_\Gamma = \int_\Gamma uvrd\Gamma \qquad \text{for all } u \in H^{1/2}(\Gamma) \cap L_r^2(\Gamma), v \in Q_r(\Gamma).$$

To get the weak formulation for the problem (3.81)-(3.84) inside the domain Ω_1, we multiply equation (3.81) by a weight function r and by an arbitrary function $v \in W_r(\Omega_1)$, integrate it over Ω_1 and transform by the first Green formula. Then the weak problem reads
Find $u \in W_r(\Omega_1)$ such that

$$(\mu_1(|\nabla u|)\nabla u, \nabla v)_{\Omega_1} = \langle \mu_1(|\nabla u|)q, v \rangle_\Gamma \quad \text{for any } v \in W_r(\Omega_1). \tag{3.85}$$

Putting together equations (3.85) and the nonlocal boundary condition (3.82) we get
Find $\mathcal{U} = (u, q) \in \mathcal{H}$ such that

$$\mathcal{A}(\mathcal{U}, v) = \mathcal{L}(v) \quad \text{for all } v \in W_r(\Omega_1). \tag{3.86}$$

Here

$$\mathcal{A}(\mathcal{U}, v) := (\mu_1 \nabla u, \nabla v)_{\Omega_1} - \langle \mu_1 q, v \rangle_\Gamma + (\frac{1}{2}\mathbf{I} - \mathbf{V}_{2,ax})u + \mathbf{V}_{1,ax}(\mu_1 q)$$

and

$$\mathcal{L}(v) := z|_\Gamma.$$

3.4.2   Discrete formulation

Let us denote by Ω_h an approximation of the bounded domain Ω_1. Let $\mathcal{T}_h$ be a regular triangulation of $\bar{\Omega}_h$ (see [23]), such that
$$\bar{\Omega}_h = \bigcup_{T \in \mathcal{T}_h} T,$$
where T is a triangular element with a diameter h_T and $h = \max_{T \in \mathcal{T}_h} h_T$. Let a set $\mathcal{E}_h$ consists of boundary edges of the triangulation $\mathcal{T}_h$

$$\mathcal{E}_h = \{E \, : \, E \text{ edge of } T \in \mathcal{T}_h, E \subset \Gamma_h\},$$

where $\partial\Omega_h = \Gamma_D \cup \Gamma_N \cup \Gamma_h$.

In the finite element-boundary element discretisation of the problem (3.86) we use the following finite dimensional spaces

$$\begin{aligned} W_h(\Omega_h) &= \{v_h \in W_r(\Omega_h) \cap C(\bar{\Omega}_h) \mid v_h \text{ is linear on each } T \in \mathcal{T}_h\}, \\ Q_h(\Gamma_h) &= \{q_h \in Q_r(\Gamma_h) \mid q_h \text{ is constant on each } E \in \mathcal{E}_h\}, \\ \mathcal{H}_h &= W_h(\Omega_h) \times Q_h(\Gamma_h). \end{aligned}$$

We apply a standard Galerkin approach for the finite element part of the problem (3.86) and boundary element collocation method for the boundary element part. This yields the following coupled method, see [78]
Find $(u_h, q_h) \in \mathcal{H}_h$ such that

$$(\mu_1(|\nabla u_h|)\nabla u_h, \nabla v_h)_{\Omega_h} = \langle \mu_1(|\nabla u_h|)q_h, v_h \rangle_{\Gamma_h} \quad \text{for all } v_h \in W_h(\Omega_h) \tag{3.87}$$

$$\frac{1}{2}u_h(\tilde{\xi}_i) - \int\limits_{\Gamma_h} q_{ax}^*(\tilde{\xi}_i,\xi)u_h(\xi)rds + \int\limits_{\Gamma_h} u_{ax}^*(\tilde{\xi}_i,\xi)\mu_1(|\nabla u_h|)q_h(\xi)rds = \tilde{z}_i \quad \text{for all } \tilde{\xi}_i \in \tilde{\Xi}_n. \quad (3.88)$$

Here $\xi \in \Gamma_h$ and $\tilde{\xi}_i = (\tilde{r}_i, \tilde{z}_i)$, $\tilde{\Xi}_n$ is a set of collocation points.

We define the boundary element-finite element basis of piecewise polynomial functions Φ based upon a domain triangulation $\mathcal{T}_h$ and a boundary grid Ξ_n as

$$\Phi = \{\phi_1, ..., \phi_N, \psi_1, ..., \psi_{n+1}, \Phi_1, ..., \Phi_n\}.$$

Here $\phi_1, \ldots, \phi_N$ are the basis functions for approximating u in Ω_h, $\psi_1, \ldots, \psi_{n+1}$ approximate u on Γ_h and $\Phi_1, \ldots, \Phi_n$ represent q on Γ_h. We set

$$u_h = \sum_{i=1}^{N} \alpha_i \phi_i + \sum_{i=1}^{n+1} \beta_i \psi_i, \quad q_h = \sum_{i=1}^{n} \gamma_i \Phi_i$$

with unknowns $\alpha = \{\alpha_1, \ldots, \alpha_N\}$, $\beta = \{\beta_1, \ldots, \beta_{n+1}\}$, $\gamma = \{\gamma_1, \ldots, \gamma_n\}$.

The finite dimensional spaces can be defined as

$$W_h = \text{span}\{\phi_1, \ldots, \phi_N, \psi_1, \ldots, \psi_{n+1}\}, \quad Q_h = \text{span}\{\Phi_1, \ldots, \Phi_n\}.$$

The isomorphism $\Phi : \mathbb{R}^{N+2n+1} \to \mathcal{H}_h$ leads to a system of nonlinear algebraic equations

$$\begin{pmatrix} A_1(u_h) & A_2(u_h) & \mathbf{0} \\ A_2^T(u_h) & A_3(u_h) & B_1(u_h) \\ \mathbf{0} & B_2 & B_3(u_h) \end{pmatrix} \begin{pmatrix} \alpha \\ \beta \\ \gamma \end{pmatrix} = \begin{pmatrix} 0 \\ 0 \\ f \end{pmatrix},$$

where

$$
\begin{aligned}
A_1 &= \{(a)_{ij} \mid a_{ij} = (\mu_1(|\nabla u_h|)\nabla\phi_j, \nabla\phi_i)_{\Omega_h}, \quad i = \overline{1,N},\ j = \overline{1,N}\}, \\
A_2 &= \{(a)_{ij} \mid a_{ij} = (\mu_1(|\nabla u_h|)\nabla\psi_j, \nabla\phi_i)_{\Omega_h}, \quad i = \overline{1,N},\ j = \overline{1,n+1}\}, \\
A_3 &= \{(a)_{ij} \mid a_{ij} = (\mu_1(|\nabla u_h|)\nabla\psi_j, \nabla\psi_i)_{\Omega_h}, \quad i = \overline{1,n+1},\ j = \overline{1,n+1}\}, \\
B_1 &= \{(b)_{ij} \mid b_{ij} = -\langle\mu_1(|\nabla u_h|)\Phi_j, \psi_i\rangle_{\Gamma_h}, \quad i = \overline{1,n+1},\ j = \overline{1,n}\}, \\
B_2 &= \{(b)_{ij} \mid b_{ij} = \frac{1}{2}\psi_j(\tilde{\xi}_i) - \int\limits_{\Gamma_h} q_{ax}^*(\tilde{\xi}_i,\xi)\psi_j rds, \quad i = \overline{1,n},\ j = \overline{1,n+1}\}, \\
B_3 &= \{(b)_{ij} \mid b_{ij} = \int\limits_{\Gamma_h} u_{ax}^*(\tilde{\xi}_i,\xi)\mu_1(|\nabla u_h|)\Phi_j rds, \quad i = \overline{1,n},\ j = \overline{1,n}\}, \\
f &= \{\tilde{z}_1 \ldots \tilde{z}_n\}.
\end{aligned}
$$

The resulting matrix is expressed as sparse finite element matrices A mixed with a dense and non-symmetric boundary element matrices B.

Convergence

The convergence of approximate solution (u_h, q_h) satisfying (3.87)-(3.88) to the solution (u, q) of the continuous problem (3.86) is connected with several difficulties caused by the problem formulation in cylindrical coordinates, by the nonlinearity of the problem and by different domains of definition of approximate and exact solutions.

In Cartesian coordinates with an assumption that $\mu_1 = const > 0$ we have the following results. The convergence of the coupled collocation boundary element and Galerkin finite element method with a finer boundary element grid or a finer finite element grid is proved in Theorems 3.3 and 3.5 in [78]

Theorem 3.4.1 (consequence of Theorem 3.3 in [78]) *Let the problem (3.86) be uniquely solvable. Let the conditions of Theorem (3.1.2) satisfy for the collocation equations (3.88), when u_h is assumed to be given (order of operator $\alpha = -1$). Furthermore, we assume a faster grid refinement of the boundary elements than of the finite elements*

$$\tilde{h} = o(h) \quad for\ h \to 0$$

and require the inverse assumption for the traces of functions $v \in H^1(\Omega_1)$ on Γ

$$||v||_{H^{\sigma+1/2}(\Gamma)} \leq ch^{-\sigma}||v||_{H^1(\Omega_1)} \tag{3.89}$$

with some $\sigma > 0$.
Then there exist $h_0 > 0$ such that for all $0 < h \leq h_0$ the coupled linear finite-element and constant boundary-element method (3.87)-(3.88) are uniquely solvable, and we have asymptotic convergence of optimal order

$$||u - u_h||_{H^\tau(\Omega_1)} + ||q - q_h||_{H^{\tilde{\tau}}(\Gamma)} \leq c \left\{ h^{\beta-\tau}||u||_{H^\beta(\Omega_1)} + \tilde{h}^{\tilde{\beta}-\tilde{\tau}}||q||_{H^{\tilde{\beta}}(\Gamma)} \right\} \tag{3.90}$$

where $\tau \in [1/2, 3/2]$, $\tilde{\tau} = \tau - 3/2$, $\beta \in [1, 3]$, $\tilde{\beta} \in [0, 1]$.

Theorem 3.5 in [78] shows the optimal order of convergence (3.90) for a faster grid refinement of the finite elements than of the boundary elements. The assumptions of Theorem 3.5 are stronger than those in Theorem 3.3. In particular, the meshes in Ω_1 and on Γ should be quasiuniform and collocation equations (3.88) can be approximated only by odd order splines.

Iterative solution of the discrete problem

There are several ways to solve the discrete nonlinear problem (3.87)-(3.88). One possibility is to reduce this problem to a sequence of linear problems by the fixed-point method. Let $(u_h^0, q_h^0) \in \mathcal{H}_h$ be arbitrary. Suppose that $(u_h^k, q_h^k) \in \mathcal{H}_h$, $k \in \{0, 1, \dots\}$ are known. Then $(u_h^{k+1}, q_h^{k+1}) \in \mathcal{H}_h$ is determined as the solution of the linear problem

$$(\mu_1(|\nabla u_h^k|)\nabla u_h^{k+1}, \nabla v_h)_{\Omega_h} = \langle \mu_1(|\nabla u_h^k|)q_h^{k+1}, v_h\rangle_{\Gamma_h} \quad \text{for all } v_h \in W_h(\Omega_h) \tag{3.91}$$

$$\frac{1}{2}u_h^{k+1}(\tilde{\xi}_i) - \int_{\Gamma_h} q_{ax}^*(\tilde{\xi}_i, \xi)u_h^{k+1}(\xi)rds + \int_{\Gamma_h} u_{ax}^*(\tilde{\xi}_i, \xi)\mu_1(|\nabla u_h^k|)q_h^{k+1}(\xi)rds = \tilde{z}_i \quad \text{for all } \tilde{\xi}_i \in \tilde{\Xi}_n. \tag{3.92}$$

To solve the linear system, corresponding (3.91)-(3.92), we use a direct solver. Namely, we apply the Gaussian elimination method with pivoting to the system

$$\begin{pmatrix} A_1(u_h^k) & A_2(u_h^k) & \mathbf{0} \\ A_2^T(u_h^k) & A_3(u_h^k) & B_1(u_h^k) \\ \mathbf{0} & B_2 & B_3(u_h^k) \end{pmatrix} \begin{pmatrix} \alpha^{k+1} \\ \beta^{k+1} \\ \gamma^{k+1} \end{pmatrix} = \begin{pmatrix} 0 \\ 0 \\ f \end{pmatrix}.$$

The iterative process continues until the defect of the linear system, when all quantities are taken at the k-th iteration, will be smaller than ε (generally 10^{-8}). Practically only a few steps (2-10) of the iterative process have to be performed to solve the linear system. Initially $\mu_1(|\nabla u_h^0|)$ set to be $1 + \chi$. It is the only quantity required to be defined from the previous iteration.

3.4.3 Numerical convergence of the coupled BEM-FEM method

Let us consider the magnetostatic problem (2.12)-(2.16), reformulated as (3.81)-(3.84). We set $\mu_1 = 6$ and take the surface Γ in the form of a circular curve with center 0 and radius $R_0 = 1$. The problem has the analytical solution

$$u(r, z) = \frac{3}{(2 + \mu_1)} z \quad \text{for } (r, z) \in \Omega_1,$$

$$q(r, z) = \frac{3}{(2 + \mu_1)} z \quad \text{for } (r, z) \in \Gamma.$$

For more details about the numerical example see Section 3.2.

We apply the coupled BEM-FEM method (3.87)-(3.88), which combines Galerkin finite element discretisation by piecewise linears for $u(r, z)$ in Ω_1 and collocation boundary element discretisation by piecewise constants for $q(r, z)$ on Γ. Following the results of the numerical tests from Section 3.2 we approximate the boundary Γ by a cubic spline. It results in a better accuracy for the solution of the collocation BEM, than approximation of Γ by piecewise linears, see Fig. 3.2 and Fig. 3.3. For the test calculations uniform grids on Γ are taken with the number of nodes $n = 64, 128, 256$. The Delaunay approach is used to construct a grid inside of the domain Ω_1. The final grid consists of 337 elements for $n = 64$, 742 elements for $n = 128$ and 1699 elements for $n = 256$, see Fig. 3.4. For details of grid construction see Section 3.5.
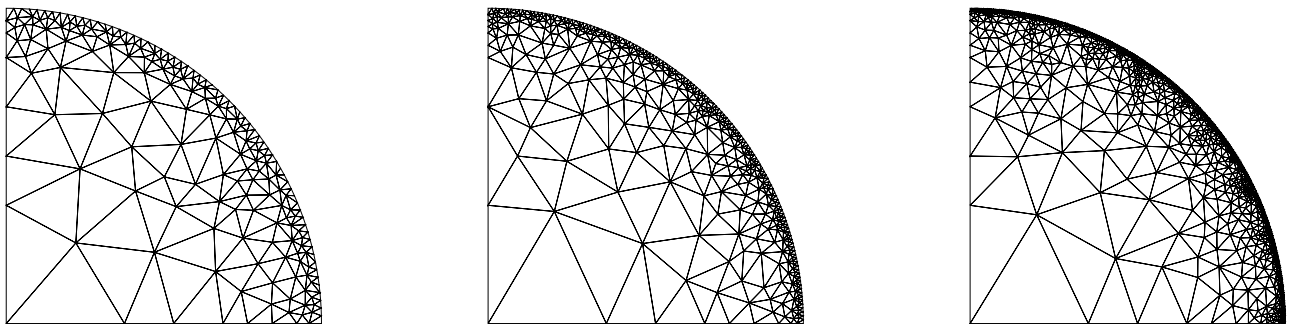

Figure 3.4: Grid configurations for $n = 64$ (left), $n = 128$ (middle) and $n = 256$ (right).

We measure the computational errors e_u and e_q on Γ in the r-weighted L^2-norm

$$||e_u||_2 = \left[\int_\Gamma r(u - u_h)^2 d\Gamma \right]^{1/2} \approx \left[\sum_{i=1}^n (u(\xi_{i-1/2}) - u_h(\xi_{i-1/2}))^2 \int_{\Gamma_i} r d\Gamma \right]^{1/2},$$

$$||e_q||_2 = \left[\int_\Gamma r(q - q_h)^2 d\Gamma \right]^{1/2} \approx \left[\sum_{i=1}^n (q(\xi_{i-1/2}) - q_h(\xi_{i-1/2}))^2 \int_{\Gamma_i} r d\Gamma \right]^{1/2},$$

where $\xi_{i-1/2}$ denotes the middle point of the boundary element Γ_i. The error for the function u is measured not over the domain Ω_1 but only over the boundary Γ in order to get numerical rate of convergence. Table 3.7 shows numerical errors $||e_u||_2$ and $||e_q||_2$ and empirical order of convergence (eoc) for different values of n. The numerical convergence of the second order for L^2-norm is consistent with results predicted by the theory in Cartesian geometry, see (3.90). The coupled BEM-FEM method results in a higher accuracy than the piecewise collocation BEM. For instance, the coupled BEM-FEM method gives $||e_u||_2$=0.214e-7 for $n = 64$, whereas the boundary element method gives $||e_u||_2$=0.167e-5, see Table 3.5.

n	$\|e_u\|_2$	eoc	$\|e_q\|_2$	eoc
64	.214e-7		.387e-6	
128	.533e-8	**2.006**	.973e-7	**1.994**
256	.133e-8	**2.003**	.244e-7	**1.997**

Table 3.7: Numerical accuracy of the coupled BEM-FEM method.

3.5   Grid generation

An important element of the numerical solution of partial differential equations by finite element methods is the grid which represents the physical domain in a discrete form. An overview on the methods for grid generation can be found in [21] and [45].

Two methods for grid generation - harmonic extension approach [21] and Delaunay technique [45, 68] are considered. These methods are briefly presented and compared with respect to the quality of the generated grids and the computational efficiency of the underlying algorithms in the application to the problem (2.12)-(2.17).

3.5.1   Harmonic extension

Popular grids are those whose generation relies on a mapping concept [21, 45]. According to this concept the nodes and cells of a grid in a region $\Omega \subset \mathbb{R}^d$ are defined by mapping the nodes and cells of a reference grid in some reference domain $\hat{\Omega} \subset \mathbb{R}^d$ with a certain transformation $A : \hat{\Omega} \to \Omega$.

Let us restrict to the case $d = 2$. Let a mapping B between the points of the reference boundary $\partial \hat{\Omega}$ and the points of the boundary $\partial \Omega$ of the computational domain be given

$$B : \partial \hat{\Omega} \to \partial \Omega.$$

The grid of the domain Ω can be determined by the mapping $A : \hat{\Omega} \to \Omega$ as a solution of the Laplace problem

$$-\Delta A = 0 \quad \text{in } \hat{\Omega}, \qquad A = B \quad \text{on } \partial \hat{\Omega}. \tag{3.93}$$

The mapping A is a harmonic extension of the mapping B given on the boundary. For details about this approach we refer to [21].

The following lemma gives an important property of the mapping A.

Lemma 3.5.1 (see Theorem 10.3.1 in [21]) *Let $\hat{\Omega} \subset \mathbb{R}^2$ be a bounded open set of class C^2 and let $\Omega \subset \mathbb{R}^2$ be a bounded convex open set. Let $B \in H^{3/2+\varepsilon}(\partial \hat{\Omega})$ be a homeomorphism between $\partial \hat{\Omega}$ and $\partial \Omega$ for $\varepsilon > 0$. Then the mapping A, defined as a solution of the problem (3.93), is a homeomorphism between the closures of $\hat{\Omega}$ and Ω.*

The problem (3.93) can be solved approximately by applying a finite element technique. A discrete Laplace operator A_h is taken as an extension operator from the boundary to the interior of the domain Ω. Let a conforming and regular triangulation of $\hat{\Omega}$ be given. We choose the space of piecewise linear functions $V_h(\hat{\Omega})$ to approximate the unknown mapping A. For the given $B(\partial \hat{\Omega})$ we define $A_h \in V_h(\hat{\Omega})$ by

$$\int_{\hat{\Omega}} \nabla A_h \nabla \psi = 0 \quad \text{for any } \psi \in V_{h,0}(\hat{\Omega}), \quad A_h(\partial \hat{\Omega}) = B(\partial \hat{\Omega}), \tag{3.94}$$

where $V_{h,0} = \{v_h \in V_h \mid v_h(\partial \hat{\Omega}) = 0\}$. Functions on the boundary are to be understood in the sense of trace, see [2].

Remark 3.5.1 *The grid determination for the domain $\Omega \subset \mathbb{R}^d$ requires d solutions of the Laplace problem (3.93).*

Remark 3.5.2 *The number of nodes and cells remains constant as predefined at the reference domain $\hat{\Omega}$ but the location of nodes are changed in $\Omega = A(\hat{\Omega})$.*

Remark 3.5.3 *The harmonic extension approach (3.93) is limited to situations where the domain Ω is convex.*

3.5.2 Delaunay approach

An other approach to the grid generation is a Delaunay technique, see [45]. The computational domain in the Delaunay triangulation is formed by tetrahedral (triangular) cells in such a way that the circumsphere of a cell does not contain any other point of the grid. This geometric constraint for grid points of the triangulation is called the Delaunay property or the Delaunay criterion. The following optimality properties are valid in two dimensions for the Delaunay triangulation, see [45]:

- Delaunay triangles are nearly equilateral;

- the maximum angle is minimised;

- the minimum angle is maximised.

Before constructing a Delaunay triangulation some grid points in a computational domain can be prespecified (for instance the points at the boundary of the domain). In this case the Delaunay property is often overridden at the points close to the prespecified ones, whereas other points obey the Delaunay criterion. A Delaunay triangulation with prespecified boundary points is called *a constrained Delaunay triangulation*. Alternatively to the constrained Delaunay triangulation *a conforming Delaunay triangulation* can be constructed. In this case grid points are added to the boundary of the computational domain and inside of it to fulfill the Delaunay criterion everywhere.

The software package **Triangle**, see [68], allows to generate constrained and conforming Delaunay triangulations by using exact arithmetic. The package includes resources to construct grids with prespecified constraints on the smallest angle and the smallest triangle area. These possibilities allow a-priory to control the quality of the generated grid. Several Delaunay algorithms for grid generation are implemented to the **Triangle**. The comparison analysis of the implemented approaches in [68] shows that the divide-and-conquer algorithm is the fastest.

3.5.3 Numerical tests

Test 1. Grid quality

Let us consider a domain Ω with a given boundary, obtained numerically by solving the problem (2.12)-(2.17). Numerical calculations was made for the linear magnetisable fluid with the parameter $\chi = 21$ for dimensionless magnetic fields $B_m = \mu_0 \chi V^{1/3} H_0^2 / (2\sigma) = \{0, 5.724, 5.725\}$. The equilibrium free boundary Γ is presented by the fixed number of points N, which are connected by line segments.

To apply the harmonic extension approach we define the reference domain $\hat{\Omega}$, a grid in $\hat{\Omega}$ and the mapping B between $\partial\hat{\Omega}$ and $\partial\Omega$. As a reference domain we take Ω for $B_m = 0$. The

boundaries $\partial\hat\Omega$ and $\partial\Omega$ consist of the horizontal boundary on the Or-axis, the vertical boundary on the Oz-axis and the free surface

$$\partial\hat\Omega = \hat\Gamma_{hor} \cup \hat\Gamma_{ver} \cup \hat\Gamma, \quad \partial\Omega = \Gamma_{hor} \cup \Gamma_{ver} \cup \Gamma.$$

By a Delaunay approach we construct a grid in $\hat\Omega$ with N prespecified nodes on $\hat\Gamma$, see 3.5a. To find the approximate mapping A_h between $\hat\Omega$ and Ω, it is enough to describe the mapping B in the pointwise sense, see (3.94). We define the nodes on Γ_{hor} and Γ_{ver} by means of a geometric sequence. The multiplier of the sequence is determined from the requirement for the edge on the Or-axis (Oz-axis), touching Γ, to have the same length as the adjoint edge on Γ. Fig. 3.5 shows grids, generated by the harmonic extension approach. The smallest angle of the triangulations equals 3.3 degree in Fig. 3.5c.

Remark 3.5.4 *The quality of the grids, generated by the harmonic extension approach, can be improved by changing the reference domain $\hat\Omega$ and the boundary mapping $B(\hat\Omega)$.*

Fig. 3.6 illustrates grids, generated by the Delaunay approach. We constructed Delaunay triangulation with prespecified nodes on Γ. We used the constraint on the smallest angle of grid cells to be more than 30 degree.

Finally we can conclude that the Delaunay approach allows to construct triangulations of the better quality than those by the harmonic extension approach. It can be essential for problems with changing boundaries when the boundary variation is strong.

Test 2. Computational efficiency: CPU-time

Let us consider a domain Ω, corresponding to Fig. 3.5b. We apply the harmonic extension and the Delaunay approaches, when the boundary Γ is given by different number of points, $N = \{64, 128, 256\}$. All calculations are made by means of a software package **MooNMD**, see [36], with the use of the package **Triangle**.

For the harmonic extension approach we create the discrete system, corresponding to the problem (3.94), and solve it by the Gauss-Seidel method. To construct the Delaunay triangulation we apply divide-and-conquer algorithm in **Triangle** and transfer the created grid to **MooNMD**. Table 3.8 presents time expenses for the algorithms realisations.

	Number of points on Γ		
Algorithm	64	128	256
Harmonic extension			
• create a discrete system	0.01	0.03	0.05
• solve a discrete system	0.03	0.06	0.27
Delaunay approach			
• create a grid	0.01	0.01	0.01
• create a new grid object	0.03	0.12	0.62

Table 3.8: Time for grid generation on a HP 9000/785/C3700 with 750 MHz processor (seconds).

The results in Table 3.8 show that the main computational efforts of the harmonic extension approach was made to solve the discrete system. The main efforts of the Delaunay technique connects with creating a new grid object in **MooNMD** for the grid, generated in **Triangle**. If to compare the algorithms on the grid with 64 points on Γ then the computational efforts of

both approaches nearly coincide. Going to the finer mesh with 128 points on Γ the harmonic extension approach seems to be working twice more quickly, whereas further increase in grid points indicate the further increase in the time ration between the harmonic extension algorithm and the Delaunay approach.

Finally we can conclude that the harmonic extension approach is computationally more effective then the Delaunay approach. From other side, the loss in quality of the grid, generated by the harmonic extension approach (see Fig. 3.5c), can be crucial for its further application for the numerical solution of differential equations.
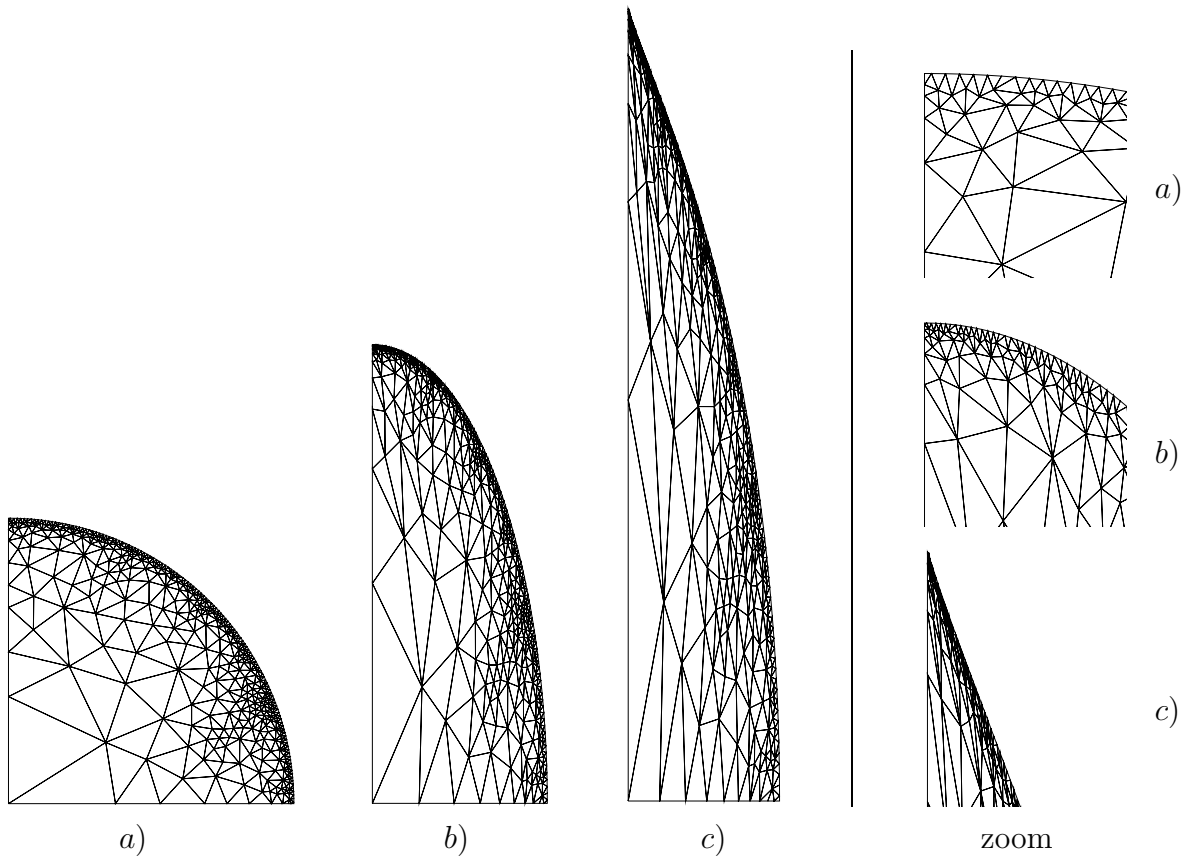
Figure 3.5: Grids, generated by the harmonic extension approach. The row of pictures at the right side presents zoom of the drop shapes at the tip.
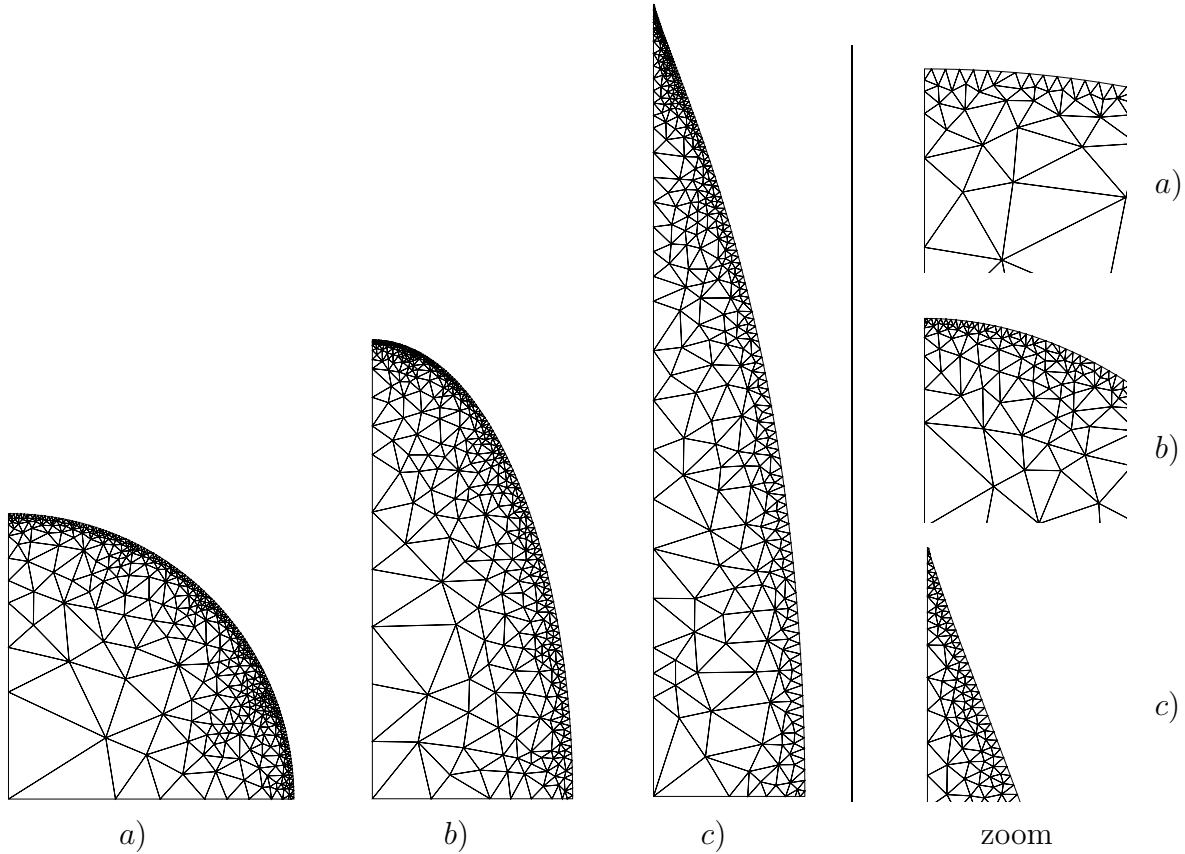
Figure 3.6: Grids, generated by the Delaunay approach. The row of pictures at the right side presents zoom of the drop shapes at the tip.

Chapter 4

Numerical methods for modeling of equilibrium free surfaces

In this chapter we study different aspects for the numerical solution of the Young-Laplace equation (2.17). Following the methods in [58] for the discretisation of the resulting parametric equations we present a finite-difference method and a spline-method.

4.1 Parametric statement of Young-Laplace equation

Surface parametrisation

Let s be an arc length of the free boundary Γ that ranges from $s = 0$ to $s = \ell$. We choose the point $s = 0$ on the z-axis and the point $s = \ell$ on the plane $z = 0$. Let us describe the boundary Γ by the parametric functions $R(s)$ and $Z(s)$, where R and Z are radial and axial surface locations in a cylindrical coordinate system. Then

$$\Gamma = \{(r, z) \mid r = R(s), z = Z(s), s = [0, \ell]\}$$

presents a parametric description of the boundary Γ.

We recall some properties of such boundary representation. For the parametrisation in respect to the arc length the natural condition is valid

$$R'(s)^2 + Z'(s)^2 \equiv 1. \tag{4.1}$$

The unit normal vector outward to the fluid domain Ω_1 and the unit tangent vector oriented in the direction of increasing s take form

$$\mathbf{n} = (-Z', R'), \quad \mathbf{t} = (R', Z').$$

The surface curvature $\mathcal{K}$ in cylindrical coordinates (r, z) is defined by the formula

$$\mathcal{K} = -(RZ')'/(RR'). \tag{4.2}$$

The minus sign in (4.2) appears, while moving along Γ in the direction of increasing s fluid remains on the right, otherwise it would be the plus sign.

Substituting the expression for the curvature (4.2) to equation (2.17) we can write

$$Z'' = R'F, \quad 0 < s < \ell, \tag{4.3}$$

$$F = -\frac{\mu_0 R_0}{2\sigma} \left[2H_0 \int_0^H M(H_0 H) dH + \left(M(H_0 H) \frac{H_n}{H} \right)^2 \right] - \frac{Z'}{R} + C,$$

where the first term of the function F is assumed to be given and C is an unknown constant.

After the differentiation of condition (4.1)

$$R'R'' + Z'Z'' \equiv 0$$

and substituting it to equation (4.3) we get that

$$R'' = -Z'F, \quad 0 < s < \ell. \tag{4.4}$$

Remark 4.1.1 *The same result we get by applying the condition $R'^2 + Z'^2 = const$ for some const ≥ 0. To fix the constant equals to 1 we should, additionally to equations (4.3) and (4.4), satisfy condition (4.1) for some value of s.*

Additionally to equations (4.3) and (4.4) we formulate boundary conditions

$$\begin{aligned}
R(0) &= 0, & R'(0) &= 1, & Z'(0) &= 0; \\
Z(\ell) &= 0, & R'(\ell) &= 0, & Z'(\ell) &= -1.
\end{aligned} \tag{4.5}$$

Setting boundary conditions $R(0) = 0$ and $Z(\ell) = 0$ we allow for the end points of the boundary Γ to lie only on the coordinate axes. The remaining boundary conditions fix the contact angle equals $\pi/2$ at the top of the drop ($s = 0$), and at the equator ($s = \ell$). Thereby we assume rounded ends for the drop surface and symmetry in respect to the plane $z = 0$.

Remark 4.1.2 *According to Remark 4.1.1 we can conclude that a solution of equations (4.3) and (4.4) satisfying any three conditions from the following four*

$$R'(0) = 1, \quad Z'(0) = 0, \quad R'(\ell) = 0, \quad Z'(\ell) = -1, \tag{4.6}$$

satisfy also the remaining one up to a sign. As a consequence, one of the conditions (4.6) can be neglected in the model. Particularly, we omit the condition $R'(0) = 1$.

A constraint for the fluid volume to be of a fixed amount (incompressible fluid)

$$V = 4\pi R_0^3 \int_0^\ell Z R R' ds \tag{4.7}$$

should be satisfied in addition.

Change of variables

The specific feature of the parametric statement (4.3)-(4.7) is that the arc length ℓ as an additional unknown in the formulation. For this reason we nondimensionalise space variables over ℓ

$$\tilde{r} = \frac{r}{\ell}, \quad \tilde{z} = \frac{z}{\ell}, \quad \tilde{s} = \frac{s}{\ell}; \quad \tilde{R}(\tilde{s}) = \frac{R(s)}{\ell}, \quad \tilde{Z}(\tilde{s}) = \frac{Z(s)}{\ell}.$$

It allows us to move the unknown length ℓ into the equations (4.3) and (4.4) and make computations at the fixed interval $(0, 1)$. The problem (4.3)-(4.7) takes the following form (we omit the tildes for convenience)

$$Z'' = R'F, \quad R'' = -Z'F, \quad F = f - \frac{Z'}{R} + C, \quad 0 < s < 1; \tag{4.8}$$

$$R(0) = 0, \; R'(0) = 1, \; Z'(0) = 0; \quad Z(1) = 0, \; R'(1) = 0, \; Z'(1) = -1;$$

$$V = 4\pi R_0^3 \ell^3 \int_0^1 Z R R' ds, \tag{4.9}$$

where $f = -\frac{\mu_0 R_0}{2\sigma}\ell\left[2H_0\int\limits_0^H M(H_0H)dH + \left(M(H_0H)\frac{H_n}{H}\right)^2\right]$.

Let us introduce a notation for the dimensionless length of the free boundary

$$L = \frac{R_0\ell}{V^{1/3}}.$$

Then the function f can be rewritten as

$$f = -\frac{\mu_0 V^{1/3}}{2\sigma}L\left[2H_0\int\limits_0^H M(H_0H)dH + \left(M(H_0H)\frac{H_n}{H}\right)^2\right].$$

From the volume constraint (4.9) we get that

$$L = \left(4\pi\int\limits_0^1 ZRR'ds\right)^{-1/3}. \tag{4.10}$$

Till now we did not fix the constant C in equations (4.8). To do it we write the first equation from (4.8) in the equivalent form

$$(RZ')' = RR'(f + C)$$

and integrate it over s at the interval (0,1)

$$\int\limits_0^1 (RZ')'ds = \int\limits_0^1 RR'(f+C)ds, \quad (RZ')|_{s=0}^{s=1} = \int\limits_0^1 RR'fds + \frac{C}{2}\left.R^2\right|_{s=0}^{s=1}.$$

Then we have

$$C = -\frac{2}{R^2(1)}\left(R(1) + \int\limits_0^1 RR'fds\right). \tag{4.11}$$

From the way of construction the expression (4.11) it follows that we formally need the boundary condition $Z'(1) = -1$ to define the constant C. From other side, Remark 4.1.2 says that one of conditions (4.6) we can neglect. Consequently, it is enough to complete equations

$$Z'' = R'F, \quad R'' = -Z'F, \quad F = f - \frac{Z'}{R} + C, \quad 0 < s < 1; \tag{4.12}$$

by four boundary conditions

$$R(0) = 0, \; Z'(0) = 0; \quad Z(1) = 0, \; R'(1) = 0, \tag{4.13}$$

where L and C are fixed by (4.10) and (4.11), respectively, and

$$f = f(H, H_n, L) = -\frac{\mu_0 V^{1/3}}{2\sigma}L\left[2H_0\int\limits_0^H M(H_0H)dH + \left(M(H_0H)\frac{H_n}{H}\right)^2\right].$$

Function f for different magnetisation laws

We concretise the form of the function f in (4.12) for different magnetisation laws $M(H)$. Namely, two cases are considered - linear magnetisation law (2.5) and the Langevin law (2.6).

For the weak magnetic fields the linear magnetisation law (2.5) is a reasonable approximation. Then the function f takes the form

$$f = -B_m L(H^2 + \chi H_n^2), \quad B_m = \frac{\mu_0 V^{1/3}\chi}{2\sigma}H_0^2, \tag{4.14}$$

where a dimensionless parameter B_m denotes the magnetic Bond number.

For the magnetic fluids with the magnetisation law in the form of the Langevin function (2.6) the function f can be written as

$$f = -WL\left[\frac{2}{3\chi}\ln\frac{\sinh(\gamma H)}{\gamma H} + \left(P(\gamma H)\frac{H_n}{H}\right)^2\right], \quad W = \frac{\mu_0 M_s^2 V^{1/3}}{2\sigma}, \, \gamma = \frac{3\chi}{M_s}H_0, \tag{4.15}$$

where W and γ are dimensionless parameters.

4.2   Finite-difference method

Discretisation

Let us introduce a uniform grid T_N on the parameter interval $[0,1]$

$$T_N = \{s_i \mid s_i = ih, \, h = 1/N, \, i = \overline{0,N}\}.$$

We define grid functions $R_h = \{R_i\}_{i=0}^N$ and $Z_h = \{Z_i\}_{i=0}^N$ such that $R_i \approx R(s_i)$, $Z_i \approx Z(s_i)$, $i = 0,\ldots,N$, where $R(s)$ and $Z(s)$ are the exact solution of the problem (4.12)-(4.13).

Following the standard approach of finite-difference methods we replace derivatives in the differential equations (4.12) by difference quotients

$$Z_{ss,i} = R_{\overset{\circ}{s},i}F(s_i,L), \quad R_{ss,i} = -Z_{\overset{\circ}{s},i}F(s_i,L), \quad i = \overline{1,N-1} \tag{4.16}$$

where

$$R_{\overset{\circ}{s},i} = \frac{1}{2h}(R_{i+1} - R_{i-1}), \quad R_{ss,i} = \frac{1}{h^2}(R_{i-1} - 2R_i + R_{i+1}),$$

$F(s_i,L) = F(R(s_i), Z(s_i), R'(s_i), Z'(s_i), H_i, H_{n,i}, L)$. The notations $Z_{\overset{\circ}{s},i}$ and $Z_{ss,i}$ are analogously defined as for the function R_h.

For the functions $R(s)$, $Z(s)$ from the space $C^4[0,1]$ and exactly given constants L and C the difference equations (4.16) have the second order of local approximation at the grid points s_i, $i = \overline{1,N-1}$. To prevent the second order of local approximation for the difference method we should approximate the function F and boundary conditions (4.13) at least with the second order. For the function F we have that

$$F(s_i,L) = F_i + O(h^2), \quad F_i = f(H_i, H_{n,i}, L_h) - \frac{Z_{\overset{\circ}{s},i}}{R_i} + C_h, \quad i = \overline{1,N-1}$$

when $C = C_h + O(h^2)$. For the volume constraint (4.9) we apply the midpoint rule to calculate the integral

$$V = V_h + O(h^2), \quad V_h = 4\pi R_0^3 \ell^3 h \sum_{i=1}^N \left[Z_{i-1/2}R_{i-1/2}\frac{R_i - R_{i-1}}{h}\right],$$

where $R_{i-1/2} = (R_{i-1} + R_i)/2$. Then

$$L_h = \left(4\pi h \sum_{i=1}^{N} \left[Z_{i-1/2} R_{i-1/2} \frac{R_i - R_{i-1}}{h} \right] \right)^{-1/3}. \tag{4.17}$$

We construct C_h from the expression (4.11) with an application of the midpoint rule for the integral calculation

$$C_h = -\frac{2}{R_N^2} \left(R_N + h \sum_{i=1}^{N} \left[R_{i-1/2} \frac{R_i - R_{i-1}}{h} f(H_{i-1/2}, H_{n,i-1/2}, L_h) \right] \right). \tag{4.18}$$

From the Taylor expansion we have

$$Z(h) = Z(0) + hZ'(0) + \frac{h^2}{2} Z''(0) + O(h^3),$$

$$Z'(0) = \frac{Z(h) - Z(0)}{h} - \frac{h}{2} R'(0) F(0, L) + O(h^2).$$

The function F contains in the expression the term Z'/R. We have that $Z'(0) = 0$ and $R(0) = 0$. By applying the L'Hopital rule then we get

$$\lim_{s \to 0} \frac{Z'(s)}{R(s)} = \lim_{s \to 0} \frac{Z''(s)}{R'(s)} = F(0, L).$$

Hence

$$F(0, L) = (f(H_0, H_{n,0}, L) + C)/2,$$

and we come to the second order approximation of the boundary condition $Z'(0) = 0$

$$\frac{Z_1 - Z_0}{h} = \frac{h}{2} F_0, \quad F_0 = \frac{1}{2} \left(f(H_0, H_{n,0}, L_h) + C_h \right).$$

In the same way we get the second order approximation for the boundary condition $R'(1) = 0$

$$\frac{R_N - R_{N-1}}{h} = -\frac{h}{2} F_N, \quad F_N = \left(f(H_N, H_{n,N}, L_h) + \frac{1}{R_N} + C_h \right).$$

By construction we get the finite-difference scheme of the second order for the problem (4.12)-(4.13)

$$Z_{ss,i} = R_{\overset{\circ}{s,i}} F_i, \quad R_{ss,i} = -Z_{\overset{\circ}{s,i}} F_i, \quad i = \overline{1, N-1} \tag{4.19}$$

$$R_0 = 0, \quad \frac{Z_1 - Z_0}{h} = \frac{h}{2} F_0, \tag{4.20}$$

$$\frac{R_N - R_{N-1}}{h} = -\frac{h}{2} F_N, \quad Z_N = 0, \tag{4.21}$$

where

$$F_i = f(H_i, H_{n,i}, L_h) - \frac{Z_{\overset{\circ}{s,i}}}{R_i} + C_h, \quad i = \overline{1, N-1},$$

$$F_0 = \frac{1}{2} \left(f(H_0, H_{n,0}, L_h) + C_h \right), \quad F_N = \left(f(H_N, H_{n,N}, L_h) + \frac{1}{R_N} + C_h \right),$$

and L_h, C_h are calculated with formulas (4.17) and (4.18), respectively.

Iterative solution of the difference problem (4.19)-(4.21)

In [53, 57, 58] two iteration-difference approaches were developed to solve nonlinear difference problem (4.19)-(4.21). One of them is the following. Suppose that R_i^k, Z_i^k, F_i^k, $i = \overline{0, N}$ are known. Let us construct $R_h^{k+1'}$ and $Z_h^{k+1'}$ in the following way

$$R_{ss,i}^{k+1'} = -Z_{\overset{\circ}{s},i}^k F_i^k, \quad i = \overline{1, N-1}$$

(4.22)

$$R_0^{k+1'} = 0, \quad \frac{R_N^{k+1'} - R_{N-1}^{k+1'}}{h} = -\frac{h}{2} F_N^k;$$

$$Z_{ss,i}^{k+1'} - R_{\overset{\circ}{s},i}^k F_i^k = 0, \quad i = \overline{1, N-1}$$

(4.23)

$$\frac{Z_1^{k+1'} - Z_0^{k+1'}}{h} = \frac{h}{2} F_0^k, \quad Z_N^{k+1'} = 0,$$

where

$$F_i^k = f(H_i, H_{n,i}, L_h^k) - \frac{Z_{\overset{\circ}{s},i}^k}{R_i^k} + C_h^k, \quad i = \overline{1, N-1}.$$

This procedure suggests a linearisation of difference equations (4.19)-(4.21). Equations (4.22) and (4.23) can be solved now in an uncoupled manner. Equations (4.22) are solved for $R_h^{k+1'}$ and equations (4.23) used to obtain $Z_h^{k+1'}$. Finally $F_i^{k+1'}$ are calculated.

To improve numerical stability of scheme (4.22)-(4.23) we apply a successive under-relaxation technique

$$u_i^{k+1} = u_i^k + \tau(u_i^{k+1'} - u_i^k), 0 < \tau < 1.$$

Thus we get the following scheme

$$\frac{1}{\tau}\left(R_{ss,i}^{k+1} - R_{ss,i}^k\right) + R_{ss,i}^k + Z_{\overset{\circ}{s},i}^k F_i^k = 0, \quad i = \overline{1, N-1}$$

(4.24)

$$R_0^{k+1} = 0, \quad \frac{R_N^{k+1} - R_{N-1}^{k+1}}{h} = -\frac{h}{2} F_N^k;$$

$$\frac{1}{\tau}\left(Z_{ss,i}^{k+1} - Z_{ss,i}^k\right) + Z_{ss,i}^k - R_{\overset{\circ}{s},i}^k F_i^k = 0, \quad i = \overline{1, N-1}$$

(4.25)

$$\frac{Z_1^{k+1} - Z_0^{k+1}}{h} = \frac{h}{2} F_0^k, \quad Z_N^{k+1} = 0.$$

For the calculations we take the relaxation parameter $\tau = 0.01$. By numerical experiments in [58] $\tau = 0.01$ are found as the preferable choice for the stability of the finite-difference scheme in a wide range of drop elongations.

Linear systems (4.24), (4.25) are tridiagonal for the unknowns at the $(k+1)$-th iteration and can be solved by the Thomas algorithm. A diagonal dominance of the matrices corresponding to (4.24) and (4.25) implies the stability of the method at every iteration.

The iterative process continues unless defects of the difference equations (4.19) at the k-th iteration are satisfied

$$\max_{i=1,N-1} \left\{ \left| R_{ss,i}^k + Z_{\circ,i}^k F_i^k \right|, \left| Z_{ss,i}^k - R_{\circ,i}^k F_i^k \right| \right\} < \varepsilon, \quad \varepsilon = 10^{-8}.$$

The iterative scheme (4.24),(4.25) was successfully applied to compute equilibrium shapes of simply- and doubly-connected surfaces both in the presence of gravitational, centrifugal and magnetic forces and their absence under zero-gravity, see [55, 74, 75].

Grid selection: stretching transformation

Let us define an independent variable transformation such that

$$s = s(t), \quad t \in [0,1] \quad \text{such that} \quad \dot{s}(t) > 0, \quad s(0) = 0, \quad s(1) = 1.$$

In order to apply this transformation to the equations (4.12)-(4.13) the following partial derivatives are formed

$$\frac{d}{ds} = \frac{d}{dt}\frac{dt}{ds} = \frac{1}{\dot{s}}\frac{d}{dt}, \quad \frac{d^2}{ds^2} = \frac{1}{\dot{s}}\left(\frac{1}{\dot{s}}\frac{d}{dt}\right)^{\cdot},$$

where dots denote derivatives in respect to t. The problem (4.12)-(4.13) can be reformulated in respect to the variable t

$$\left(\frac{\dot{Z}}{\dot{s}}\right)^{\cdot} = \dot{R}F, \quad \left(\frac{\dot{R}}{\dot{s}}\right)^{\cdot} = -\dot{Z}F, \quad F = f - \frac{\dot{Z}}{\dot{s}R} + C, \quad 0 < t < 1; \tag{4.26}$$

$$R(0) = 0, \ \dot{Z}(0) = 0; \quad Z(1) = 0, \ \dot{R}(1) = 0, \tag{4.27}$$

where

$$f = f(H, H_n, L) = -\frac{\mu_0 V^{1/3}}{2\sigma} L \left[2H_0 \int_0^H M(H_0 H)dH + \left(M(H_0 H)\frac{H_n}{H} \right)^2 \right],$$

$$C = -\frac{2}{R^2(1)}\left(R(1) + \int_0^1 R\dot{R}f dt \right), \quad L = \left(4\pi \int_0^1 ZR\dot{R}dt \right)^{-1/3}.$$

The finite-difference scheme of the second order for the problem (4.26)-(4.27) can be constructed in the same manner as it was done for the problem formulation (4.12)-(4.13). Analogously to the difference problem (4.19)-(4.21) we write

$$\frac{1}{h}\left(\frac{Z_{i+1} - Z_i}{h\dot{s}(t_{i+1/2})} - \frac{Z_i - Z_{i-1}}{h\dot{s}(t_{i-1/2})} \right) = R_{t,i}^\circ F_i, \quad i = \overline{1, N-1} \tag{4.28}$$

$$\frac{1}{h}\left(\frac{R_{i+1} - R_i}{h\dot{s}(t_{i+1/2})} - \frac{R_i - R_{i-1}}{h\dot{s}(t_{i-1/2})} \right) = -Z_{t,i}^\circ F_i, \quad i = \overline{1, N-1} \tag{4.29}$$

$$R_0 = 0, \quad \frac{Z_1 - Z_0}{h} = \frac{h\dot{s}(0)^2}{2}F_0, \tag{4.30}$$

$$\frac{R_N - R_{N-1}}{h} = -\frac{h\dot{s}(1)^2}{2}F_N, \quad Z_N = 0, \tag{4.31}$$

where

$$F_i = f(H_i, H_{n,i}, L_h) - \frac{Z_{t,i}^{\circ}}{\dot{s}(t_i) R_i} + C_h, \quad i = \overline{1, N-1},$$

$$F_0 = \frac{1}{2}\left(f(H_0, H_{n,0}, L_h) + C_h\right), \quad F_N = \left(f(H_N, H_{n,N}, L_h) + \frac{1}{R_N} + C_h\right),$$

and L_h, C_h are calculated with formulas (4.17) and (4.18), respectively.

It is known from the experimental observations that with increase of the applied magnetic field the drop extends in the direction of the field and forms peak-shaped surfaces [8, 14]. The surface curvature increases strongly at the region of the drop tip ($s = 0$). In addition, the curvature decreases monotonically as we move away from the peak. This preliminary information on the structure of the solution can be used as a criterion for the grid construction to resolve accurately area of high curvatures.

Let us consider the stretching transformation proposed in [62] for boundary layer problems with a reformulation in the form, see [4]

$$t(s) = 1 - \frac{\ln\left[1 + 2(1-s)/(a+s)\right]}{\ln\left[1 + 2/a\right]}, \quad s \in [0,1], \quad a > 0,$$

with the inverse

$$s(t) = -a + \frac{2(a+1)}{1 + (1 + 2/a)^{1-t}}, \quad t \in [0,1], \quad a > 0.$$

By construction the transformation $s(t)$ concentrates grid points near the boundary $t = 0$ as the stretching parameter a approaches 0. The stretching parameter suggested in [62] is related to the boundary layer thickness d by

$$(1+a)^2 = \frac{1}{1-d}.$$

A special choice of the parameter a was suggested in [58] for solving free-surface equations, when the high resolution of the solution requires in the region of high curvatures ($t = 0$). The stretching parameter a was determined by the requirement for the product of the mean curvature dimensionless over the arc length $R_0\ell$ at the drop tip ($t_0 = 0$) by the step size of the stretched grid $s(t_1) - s(t_0)$ to be constant, equals the product of the dimensionless mean curvature of the spherical drop $\pi/2$ by the step size of the uniform grid $h = t_1 - t_0$. We have for the dimensionless mean curvature that

$$-\left.\frac{(RZ')'}{2RR'}\right|_{s=0} = -(f(H_0, H_{n,0}, L_h) + C_h)/2.$$

Hence we get the condition for the parameter a in the following form

$$-(f(H_0, H_{n,0}, L_h) + C_h)\left[-a + \frac{2(a+1)}{1 + (1 + 2/a)^{1-h}}\right] = \pi h. \tag{4.32}$$

By construction we have that increase in curvature at the drop tip is proportional to decrease in the smallest step size of the stretched grid. The grid points are therefore densest at the tip of the drop, where greater resolution is desirable.

For the fixed value of a and the given set of parameters (B_m or W and γ, see (4.14), (4.15)) we get numerically the drop shape by solving equations (4.28)-(4.31). Using (4.32) we determine a new value of the parameter a, which is used for further calculations.

4.3   Spline method

The cubic spline

Let us introduce a uniform grid T_N on the parameter interval $[0, 1]$

$$T_N = \{s_i \mid s_i = ih, \ h = 1/N, \ i = \overline{0, N}\}.$$

We consider a space of cubic splines

$$S_{4,3}(T_N) = \{u(s) \in C^2(T_N) \mid u(s)|_{(s_{i-1}, s_i)} \in P_3(s_{i-1}, s_i), \ i = \overline{1, N}\}.$$

It is well known, see for instance [3], that $u(s) \in S_{4,3}(T_N)$ on $[s_{i-1}, s_i]$ can be presented as

$$
\begin{aligned}
u(s) \ &= \ M_{i-1}\frac{(s_i - s)^3}{6h} + M_i\frac{(s - s_{i-1})^3}{6h} \\
&+ \ \left(u_{i-1} - \frac{h^2}{6}M_{i-1}\right)\frac{s_i - s}{h} + \left(u_i - \frac{h^2}{6}M_i\right)\frac{s - s_{i-1}}{h},
\end{aligned}
\tag{4.33}
$$

where $M_i = u''(s_i)$, $u_i = u(s_i)$. Due to (4.33), the functions $u(s)$ and $u''(s)$ are continuous on $[0, 1]$. From (4.33) we can get the expressions for the one-sided limits of the derivative

$$
\begin{aligned}
\lim_{s \to 0} u'(s_i - s) \ &= \ u'(s_i^-) = \frac{u_i - u_{i-1}}{h} - \frac{h}{6}(M_i - M_{i-1}) + \frac{h}{2}M_i, \\
\lim_{s \to 0} u'(s_i + s) \ &= \ u'(s_i^+) = \frac{u_{i+1} - u_i}{h} - \frac{h}{6}(M_{i+1} - M_i) - \frac{h}{2}M_i.
\end{aligned}
\tag{4.34}
$$

Let us now enforce the continuity of $u'(s)$ by means of (4.34)

$$\frac{u_i - u_{i-1}}{h} - \frac{h}{6}(M_i - M_{i-1}) + \frac{h}{2}M_i = \frac{u_{i+1} - u_i}{h} - \frac{h}{6}(M_{i+1} - M_i) - \frac{h}{2}M_i, \tag{4.35}$$

where $i = \overline{1, N-1}$. We assume that two additional condition are given

$$u'(0) = a, \quad u'(1) = b \quad \text{or} \quad u''(0) = a, \quad u''(1) = b. \tag{4.36}$$

Using (4.34) we get

$$\frac{u_1 - u_0}{h} - \frac{h}{6}(M_1 - M_0) - \frac{h}{2}M_0 = a, \quad \frac{u_N - u_{N-1}}{h} - \frac{h}{6}(M_N - M_{N-1}) + \frac{h}{2}M_N = b \quad \text{or}$$

$$M_0 = a, \qquad\qquad\qquad\qquad\qquad\qquad M_N = b. \tag{4.37}$$

From Theorem 3.5.1 and 3.6.1 in [3] it follows that for the given values u_i, a, b such that

$$u(s_i) = u_i, \quad i = \overline{1, N-1}$$

with conditions at the end points (4.36)

$$u'(0) = a, \quad u'(1) = b, \quad \text{or} \quad u''(0) = a, \quad u''(1) = b$$

the cubic spline $u(s) \in S_{4,3}(T_N)$ exists and unique.

If $f(s) \in C^4[0, 1]$ and

$$u(s_i) = f(s_i), \quad i = \overline{1, N-1}$$

with conditions at the end points

$$u'(0) = f'(0), \quad u'(1) = f'(1) \quad \text{or} \quad u''(0) = f''(0), \quad u''(1) = f''(1),$$

then for the spline function $u(s) \in S_{4,3}(T_N)$ we have

$$f^{(\alpha)}(s) = u^{(\alpha)}(s) + O(h^{4-\alpha}), \quad \alpha = \overline{0,4} \tag{4.38}$$

uniformly with respect to s in $[0,1]$, see [3]. Moreover, the convergence can not be higher, unless $f(s)$ is itself a cubic polynomial, see Section 3.12 in [3].

Discretisation

We find an approximate solution R_h, Z_h for the problem (4.12)-(4.13) in the space of cubic splines $S_{4,3}(T_N)$ by satisfying the differential equations at the grid points $s_i \in T_N$

$$M_i^z = R_h'(s_i)F(s_i, L), \quad M_i^r = -Z_h'(s_i)F(s_i, L), \quad i = \overline{1, N-1}; \tag{4.39}$$

$$R_h(s_0) = 0, \; Z_h'(s_0) = 0; \quad Z_h(s_N) = 0, \; R_h'(s_N) = 0, \tag{4.40}$$

where $M_i^r = R_h''(s_i)$, $M_i^z = Z_h''(s_i)$.

By construction, spline functions should satisfy condition (4.35) which expresses the continuity of $R_h'(s)$ and $Z_h'(s)$ at the inner grid points $s_i, i = \overline{1, N-1}$. Additionally we set boundary conditions at the end points by satisfying equations (4.12) at s_0 and s_N

$$M_0^r = 0, \quad M_0^z = F_0; \quad M_N^r = F_N, \quad M_N^z = 0. \tag{4.41}$$

We have $4(N-1) + 8$ equations in respect to $4(N+1)$ unknowns R_i, Z_i, M_i^r, M_i^z, $i = \overline{0, N}$.

For the functions $R(s)$, $Z(s)$ from the space $C^4[0,1]$ and exactly given constants L and C the difference equations (4.39) have the second order of local approximation at the grid points s_i, $i = \overline{1, N-1}$. Precisely, we substitute $R(s)$ and $Z(s)$ into difference equations and from (4.38) we get

$$Z''(s_i) = R'(s_i)F(s_i, L) + T_i(h), \quad R''(s_i) = -Z'(s_i)F(s_i, L) + T_i(h), \quad i = \overline{1, N-1},$$

with the local truncation error

$$T_i(h) = O(h^2) + F(s_i, L)O(h^3).$$

To prevent the second order of local approximation for equations (4.39) we approximate the function F at least with the second order

$$F(s_i, L) = F_i + O(h^2), \quad F_i = f(H_i, H_{n,i}, L_h) - \frac{Z_h'(s_i)}{R_i} + C_h, \quad i = \overline{1, N-1}$$

$$F_0 = \frac{1}{2}\left(f(H_0, H_{n,0}, L_h) + C_h\right), \quad F_N = \left(f(H_N, H_{n,N}, L_h) + \frac{1}{R_N} + C_h\right).$$

when $C = C_h + O(h^2)$. For the details of getting expression for F_0 see Section 4.2.

For the volume constraint (4.9) we apply Gaussian quadrature formula with 5 points to get exact integral evaluation. As a consequence we have

$$L_h = L.$$

We construct C_h from the expression (4.11) in the following way

$$C_h = -\frac{2}{R_N^2}\left(R_N + h\sum_{i=1}^N f(H_{i-1/2}, H_{n,i-1/2}, L_h) \int_{s_{i-1}}^{s_i} R_h R_h' ds\right), \tag{4.42}$$

where integrals are calculated exactly by Gaussian formulas with 3 points.

Problem reformulation

The problem reformulation follows the idea suggested in [58].

For the spline functions $R_h(s)$ we have by the Taylor expansion that

$$R'_h(s_{i-1/2}) = R'_h(s_i) - \frac{h}{2}M_i^r + \frac{h^2}{8}R'''_h(s_i - 0) = R'_h(s_i) - \frac{h}{2}M_i^r + \frac{h^2}{8}R'''_h(s_{i-1/2}),$$

$$R'_h(s_{i+1/2}) = R'_h(s_i) + \frac{h}{2}M_i^r + \frac{h^2}{8}R'''_h(s_i + 0) = R'_h(s_i) + \frac{h}{2}M_i^r + \frac{h^2}{8}R'''_h(s_{i+1/2}).$$

It follows that

$$R'_h(s_i) = \frac{q_i^r + q_{i+1}^r}{2} \quad i = \overline{1, N-1}, \tag{4.43}$$

$$M_i^r = \frac{q_{i+1}^r - q_i^r}{h} \quad i = \overline{1, N-1}, \tag{4.44}$$

where

$$q_i^r = R'_h(s_{i-1/2}) - \frac{h^2}{8}R'''_h(s_{i-1/2}), \quad i = \overline{1, N}.$$

Analogously we can write for the function $Z_h(S)$

$$Z'_h(s_i) = \frac{q_i^z + q_{i+1}^z}{2} \quad i = \overline{1, N-1}, \tag{4.45}$$

$$M_i^z = \frac{q_{i+1}^z - q_i^z}{h} \quad i = \overline{1, N-1}, \tag{4.46}$$

where

$$q_i^z = Z'_h(s_{i-1/2}) - \frac{h^2}{8}Z'''_h(s_{i-1/2}), \quad i = \overline{1, N}.$$

We substitute (4.43)-(4.46) to equations (4.39) and use the Taylor expansion at the end points together with boundary conditions $Z'_h(s_0) = 0$ and $R'_h(s_N) = 0$

$$\Lambda_1(q^r, q^z, F)|_i \equiv q_{i+1}^r - q_i^r + \frac{h}{2}\left(q_i^z + q_{i+1}^z\right)F_i = 0 \quad i = \overline{1, N-1} \tag{4.47}$$

$$\Lambda_2(q^r, q^z, F)|_i \equiv q_{i+1}^z - q_i^z - \frac{h}{2}\left(q_i^r + q_{i+1}^r\right)F_i = 0 \quad i = \overline{1, N-1} \tag{4.48}$$

$$q_1^z = \frac{h}{2}F_0, \quad q_N^r = -\frac{h}{2}F_N. \tag{4.49}$$

Introducing new variables q_i^r, q_i^z allows us to reformulate the problem with $4(N+1)$ unknowns as two subproblems. The first one is solving (4.47)-(4.48) in respect to q_i^r, q_i^z, $i = \overline{1, N}$. The other one is calculating R_i, Z_i, M_i^r, M_i^z, $i = \overline{0, N}$ using direct formulas (4.43), (4.44) and conditions (4.41) together with the representations for the spline derivatives (4.34)

$$M_0^r = 0, \quad M_i^r = \frac{q_{i+1}^r - q_i^r}{h}, \quad M_N^r = F_N \quad i = \overline{1, N-1} \tag{4.50}$$

$$M_0^z = F_0, \quad M_i^z = \frac{q_{i+1}^z - q_i^z}{h}, \quad M_N^z = 0 \quad i = \overline{1, N-1} \tag{4.51}$$

$$R_0 = 0, \quad \frac{R_i - R_{i-1}}{h} - \frac{h}{6}(M_i^r - M_{i-1}^r) + \frac{h}{2}M_i^r = \frac{q_i^r + q_{i+1}^r}{2} \quad i = \overline{1, N} \tag{4.52}$$

$$Z_N = 0, \quad \frac{Z_{i+1} - Z_i}{h} - \frac{h}{6}(M_{i+1}^z - M_i^z) - \frac{h}{2}M_i^z = \frac{q_i^z + q_{i+1}^z}{2} \quad i = \overline{0, N-1}. \tag{4.53}$$

Iterative solution of the difference problem (4.47)-(4.53)

Because of the function F depends on R_h, Z_h, the subproblems (4.47)-(4.49) and (4.50)-(4.53) are coupled. One possibility is to split the subproblems iteratively. A single iteration of the iterative decoupling strategy reads as follows.

Suppose that F_i^k, $i = \overline{0, N}$ are given. At first we solve equations (4.47)-(4.49) to find $(q_i^r)^{k+1}$, $(q_i^z)^{k+1}$, $i = \overline{1, N}$. Then by relations (4.50)-(4.53) one after another we calculate $(M_i^r)^{k+1}$, $(M_i^z)^{k+1}$, R_i^{k+1}, Z_i^{k+1}, $i = \overline{0, N}$. Finally we can get F_i^{k+1}, the initial data for the next iteration.

To solve nonlinear equations (4.47)-(4.49) we apply an iterative technique with under-relaxation, similar to (4.24)-(4.25), constructed for the difference method.

Suppose that $(q_i^r)^l$, $(q_i^z)^l$, F_i^l are known. Let us construct $(q_i^r)^{l+1}$, $(q_i^z)^{l+1}$ in the following way

$$(q_{i+1}^r)^{l+1} - (q_i^r)^{l+1} = (q_{i+1}^r)^l - (q_i^r)^l - \tau \Lambda_1^l(q^r, q^z, F)|_i, \quad i = \overline{1, N-1}$$

(4.54)

$$(q_N^r)^{l+1} = -\frac{h}{2} F_N^l;$$

$$(q_{i+1}^z)^{l+1} - (q_i^z)^{l+1} = (q_{i+1}^z)^l - (q_i^z)^l - \tau \Lambda_2^l(q^r, q^z, F)|_i, \quad i = \overline{1, N-1}$$

(4.55)

$$(q_1^z)^{l+1} = \frac{h}{2} F_0^l.$$

Here $0 < \tau < 1$ is a relaxation parameter.

In [58] two different algorithms to solve equations (4.47)-(4.49) are suggested. Instead of using boundary condition (4.49), the Algorithm (47) in [58] applies both conditions on the left side $R_h'(s_0) = 1$, $Z_h'(s_0) = 0$, resulting in

$$q_1^r = 1, \quad q_1^z = \frac{h}{2} F_0,$$

(4.56)

when the Algorithm (44) in [58] uses the conditions on the right side $R_h'(s_N) = 0$, $Z_h'(s_N) = -1$

$$q_N^r = -\frac{h}{2} F_N, \quad q_N^z = -1.$$

(4.57)

Definition of both boundary conditions on the same side allows to find the solution for q^r and q^z on the $(k+1)$-th external iteration by the recursive procedures, see [58]. It requires no additional iterative process, like (4.54), (4.55), when the boundary conditions on both sides (4.49) are specified.

4.4   Stabilisation by relaxation: test example

We applied a successive under-relaxation technique for equations (4.22)-(4.23) and (4.47)-(4.49) to improve the numerical stability of the methods. The aim of this section is to examine the influence of relaxation to the stability of the iterative schemes for the finite-difference (4.24)-(4.25) and for the spline methods (4.50)-(4.55).

Let us consider the problem formulation with the function f in the form

$$f = -WL(r')^2, \quad W = \frac{\mu_0 M_s^2 V^{1/3}}{2\sigma}.$$

This corresponds to the test problem in [58]. Such a formulation is the case of the saturated magnetic fluid, when the magnetisation $M = M_s$. For details of the model see [58].

Analogously to [58] we present the number of iterations for the finite-difference scheme (4.24)-(4.25) (*FD*), for the spline schemes (4.50)-(4.55) (*S-1*) and the spline schemes (44)-(46) in [58] (*S-2*) for different relaxation τ and parameter W. The difference in spline schemes appears due to the definition of boundary conditions as (4.49) or (4.57).

	$\tau = 0.5$			$\tau = 0.1$			$\tau = 0.05$			$\tau = 0.01$		
W	*FD*	*S-1*	*S-2*	*FD*	*S-1*	*S-2*	*FD*	*S-1*	*S-2*	*FD*	*S-1*	*S-2*
2.5	19	19	63	113	113	339	231	231	683	1167	1167	3439
5	210	209	61	123	123	323	249	249	651	1262	1261	3278
7.5	×	×	57	129	128	301	261	261	608	1320	1319	3058
10	-	-	57	132	132	282	268	268	569	1357	1355	2863
12.5	-	-	137	134	134	267	273	272	537	1377	1375	2702
15	-	-	×	136	136	254	276	275	511	1391	1387	2568
...				...	...	...	...	...	...	...	...	...
27.5	-	-	-	209	203	220	274	272	428	1381	1372	2121
30	-	-	-	417	387	219	272	270	418	1370	1360	2059
32.5	-	-	-	×	×	225	270	268	409	1357	1346	2001
...						...	...	...	...	...	...	...
40	-	-	-	-	-	542	268	268	388	1313	1296	1853
42.5	-	-	-	-	-	1259	386	362	382	1301	1285	1809
45	-	-	-	-	-	×	833	720	378	1292	1277	1769
47.5	-	-	-	-	-	-	×	×	363	1295	1287	1733
...									...	...	...	...
55	-	-	-	-	-	-	-	-	377	2260	2189	1615
57.5	-	-	-	-	-	-	-	-	411	3424	3224	1586
60	-	-	-	-	-	-	-	-	470	∞	> 5000	1580
...									...			...
70	-	-	-	-	-	-	-	-	1193	-	-	1429
72.5	-	-	-	-	-	-	-	-	2180	-	-	1411
75	-	-	-	-	-	-	-	-	∞	-	-	1383
...												...
187.5	-	-	-	-	-	-	-	-	-	-	-	3316
190	-	-	-	-	-	-	-	-	-	-	-	4035
192.5	-	-	-	-	-	-	-	-	-	-	-	> 5000

Table 4.1: Iteration number of the finite-difference scheme (*FD*), spline scheme (4.50)-(4.55) (*S-1*) and spline scheme (44)-(46) in [58] (*S-2*). The cross sign denotes numerical instability.

The calculations were made on the uniform grid with $h = 0.01$. The parameter W was changed with a step of 2.5. An initial iterative approximation for new W was a solution obtained for the previous value of W. As a criterion for the accuracy of an iterative solution we asked for the defect of the difference equations to be less than a tolerance $\varepsilon = 10^{-4}$.

From the Table 4.1 we can see that decrease in the relaxation parameter τ results in increase of number of iterations or, by other words, slows the convergence. From other side decrease in τ improves numerical stability as parameter W increases. For instance, for $W = 40$ only schemes with $\tau = 0.05$ and $\tau = 0.01$ converge, schemes with $\tau = 0.5$ and $\tau = 0.1$ are numerically unstable. Increase in W corresponds to stronger change in curvature at the free surface.

Comparing different methods we state that the convergence and stability properties of the finite-difference scheme and the spline scheme *S-1* are nearly identical. The spline scheme *S-2*

shows better stability properties and is comparable (even better for $\tau = 0.01$) in performance to the fourth-order tangential scheme in [58].

For the test example we applied also the spline scheme (45)-(47) in [58] where the left side conditions (4.56) are used. The scheme shows no convergence for any values of the relaxation parameter. From the results of the numerical experiments we assume that for axisymmetric problems one of the 'non-axis' conditions (4.57) should necessarily satisfy.

The main advantage of the spline-method over the finite-difference method is that the solution of the Young-Laplace equation is found in the form of an analytical representation lying in $C^2[0, 1]$. The finite-difference method gives only point-wise boundary representation and requires additional efforts to construct smooth boundary approximation. The boundary smoothness is important requirement for an application of boundary element methods. Influence of boundary approximation to the convergence of piecewise-constant collocation was analysed in Section 3.2.

Chapter 5

Numerical results on a magnetic-fluid drop

At the beginning of the chapter with numerical results let us estimate the relevant characteristic dimensionless parameters of the problem. We distinguish two situations. The first one corresponds to calculations for linear magnetisable fluids, the second - for nonlinear magnetisable ones. In the case of linear magnetisable fluids the initial susceptibility χ and the magnetic Bond number B_m are the dimensionless parameters representing the evolution of the drop surface

$$\chi, \quad B_m = \mu_0 V^{1/3} \chi H_0^2 / (2\sigma).$$

For nonlinear magnetisable fluids the initial susceptibility χ, the dimensionless field strength γ and the parameter W describes the problem

$$\chi, \quad \gamma = 3\chi H_0 / M_s, \quad W = \mu_0 M_s^2 V^{1/3} / (2\sigma).$$

For linear magnetisable fluids we take the initial susceptibility $\chi \in \{5, 21, 40\}$. The susceptibility of magnetic fluids takes moderate value $\chi < 10$, see for instance [17]. The hysteresis for the drop deformation is predicted for $\chi > 20$ and may be observed only for the concentrated phase microdrops formed during the separation process of colloidal ferromagnetic, see [17]. For nonlinear magnetisable fluids we choose $\chi \in \{1.9, 5, 21\}$.

The magnetic constant $\mu_0 = 4\pi \cdot 10^{-7}$ H/m denotes the permeability in vacuum. We take the surface tension $\sigma \sim 0.0265$ kg/s^2, the initial drop radius as the characteristic length $R_0 \sim 10^{-3}$ m and the magnetic saturation $M_s \in [5, 45]$ kA/m. We assume the applied magnetic field $H_0 \in [0, 6]$ kA/m for the model with linear magnetisable fluids and $H_0 \in [0, 750]$ kA/m for nonlinear magnetisable ones. Then the dimensionless parameters are specified as follows

$$\chi \in \{5, 21, 40\}, \quad B_m \in [0, 40]; \quad \chi \in \{1.9, 5, 21\}, \quad \gamma \in [0, 10^2], \quad W = \{5, 500\}.$$

For all simulations we used a code based on the software package **MooNMD**, see [36]. The main part of the program package presents variety of tools to apply finite element methods for solving many classes of partial differential equations in two- and three-dimensional cases. The package **MooNMD** was successfully applied in the solution of the incompressible steady state and time dependent Navier-Stokes equations [33, 34, 49], for the large eddy simulation of turbulent flows [32, 35] and for free boundary value problems with capillary surfaces [41, 46]. The flexibility of the package **MooNMD** is realised by a strict separation of geometry and finite element data. For the numerical simulation of equilibrium magnetic fluid drops several algorithms were additionally programmed. Namely, a one-dimensional collocation BEM and numerical methods of Chapter 4 for modeling equilibrium free surfaces were added to the **MooNMD**.

For the first publications of the numerical results, presented in Chapter 5, see [42, 43].

5.1   Linear magnetisable fluids

5.1.1   Comparison with spheroidal shapes, hysteresis effect

There are different approaches for the theoretical description of a behaviour of a drop in a field, see [8, 14, 17, 72]. All solutions of the theoretical studies are approximate due to the assumption for the drop shape to be spheroidal and restricted to the case of the weak magnetic fields, when the linear magnetisation law $M(H) = \chi H$ can be applied.

The theoretical approach presented in [8] is based on the minimisation of the magnetic energy and the interfacial energy in respect to the aspect ratio between major and minor spheroid semi-axes. In [14] the free surface equation is required to be satisfied only at the top and the equator of a spheroid. Authors in [17, 72] analyse the drop behaviour by using a virial method. The comparative analysis of all mentioned theoretical approaches, see [17], concludes that the theoretical studies yield identical results for small drop deformations. Moreover, they reported that the energy approach in [8] and the virial technique in [17, 72] give identical results for any field, despite the fact that the solutions of both methods have different analytical representations.

Let the magnetic fluid drop has some shape with lengths a and b along z and r axes, respectively. The drop sizes a and b are the analog of major and minor spheroid semi-axes. As a geometrical characteristic of the drop deformation a length-to-diameter ratio a/b is measured for different values of the applied field.

The numerical and theoretical (energy approach in [8]) dependences of drop deformations upon the dimensionless magnetic field $B_m = \mu_0 V^{1/3} \chi H_0^2/(2\sigma)$, for several values of the magnetic susceptibility χ are displayed in Fig. 5.1-5.3. Each curve is a solution family computed at a fixed value of $\chi = \{5, 21, 40\}$ corresponding to Figs. 5.1, 5.2, 5.3, respectively, and is traced by continuation in the value of the field B_m. The pictures that higher values of the applied field B_m cause the drop to elongate along the field direction.

For the case $\chi = 5$, see Fig. 5.1, the numerical and theoretical results show quantitative agreement within 0.5% . It allows us to conclude that for such a fluid the numerically computed drop shapes are very close to prolate spheroid, see Fig. 5.1 at the right. According to the results of numerical simulations we can report also that theoretical studies in [8, 14, 17] give reasonable approximation for the drop shaping of the fluids with $\chi \leq 5$ in the region of weak fields.

For the first time, experimental measurements of hysteresis in the deformation of agglomerate drops (2 to 20 μm) of a magnetic fluid are reported in [8]. According to the theoretical results in [8, 14, 17] the drop deformation displays hysteresis as a function of the applied field for $\chi > 20$. The found dependencies are characterized by the existence of a region where for a certain magnetic field threshold the drop becomes unstable jumping from a slightly elongated shape to a much more elongated one. When decreasing the magnetic field the same feature occurs but for a smaller magnetic field threshold. A limited range of the magnetic field strength values exists (hysteretic regime), where two equilibrium configurations of a drop are allowed, one of which occurs upon increasing the strength of a magnetic field, another - upon its decrease. Numerically we observed that the dependence of the drop elongation upon the field goes from a monotone curve for $\chi < 21$ to S-shaped curves for $\chi \geq 21$, see Fig. 5.1-5.3.

Precise determination of a critical value χ_c, presenting the lowest χ for which hysteresis effect appears, is not a subject of the current work. Many investigations to verify the critical point are fulfilled [8, 48, 67, 79]. The minimum-energy argument in [8] predicts that hysteresis should occur when $\chi_c = 19.8$. In the first numerical study on this problem in [48] the bound $18 < \chi_c < 19$ is defined. The critical point found numerically in [67] is specified in the range $18.6 \leq \chi_c \leq 18.7$. The results of the paper [79] show that hysteresis should be observed over
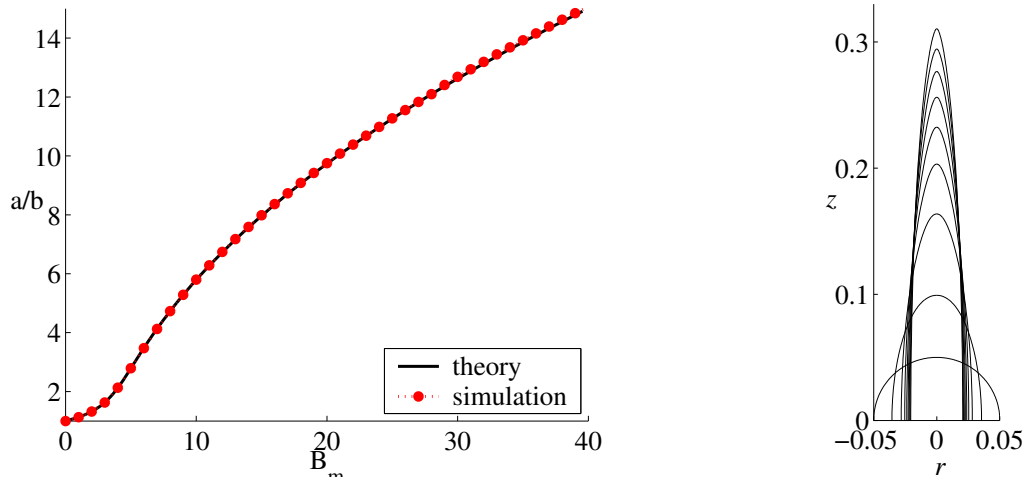
Figure 5.1: The dependence of the drop elongation upon the magnetic field: $\chi = 5$, linear magnetisation law. Shapes on the right correspond to $B_m = \{0, 5, 10, 15, 20, 25, 30, 35, 40\}$.
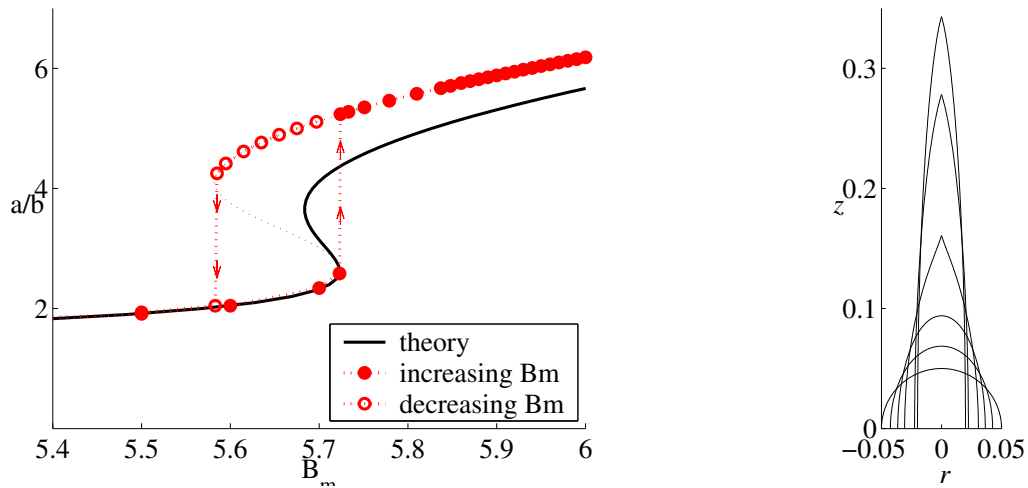

Figure 5.2: The dependence of the drop elongation upon the magnetic field: $\chi = 21$, linear magnetisation law. Shapes on the right correspond to $B_m = \{0, 5, 5.723, 5.725, 10, 15\}$.
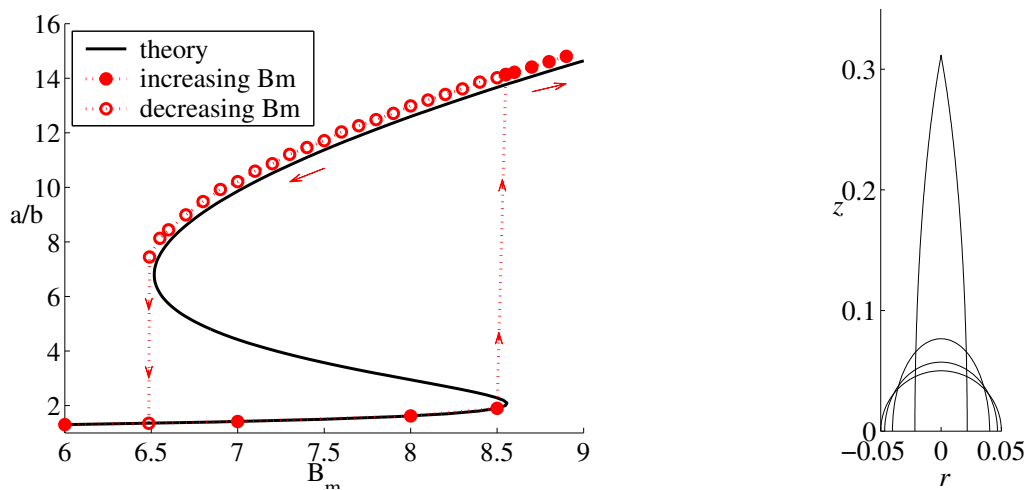

Figure 5.3: The dependence of the drop elongation upon the magnetic field: $\chi = 40$, linear magnetisation law. Shapes on the right correspond to $B_m = \{0, 5, 8.5, 8.55\}$.

the range $19.25 \pm 0.25 \leq \chi_c \leq 20.75 \pm 0.25$. To guarantee the appearance of the hysteresis in drop deformation the value $\chi = 21$ is taken in our numerical simulations.

The difference between theory and numerics for $\chi \geq 21$, see Fig. 5.2, 5.3, lies within 1% for the lower branch of the solution, but shows more then 15% for the upper branch. The quantitative difference might be connected with the assumption of the theoretical model for a drop to be a spheroid for any applied field. Surfaces close to conical are observed numerically for the upper branches of solution, see Fig. 5.2 and 5.3 at the right. An appearance of shapes with pointed ends is confirmed experimentally in [8, 10].

Figs. 5.4-5.6 show equilibrium shapes for $\chi = \{5, 21, 40\}$ and different values of the applied magnetic field B_m. A close-up view of the drop tips is presented on the right of Figs. 5.4-5.6. The drop tip is becoming increasingly more conical as the aspect ration increases. The curvatures at the drop tip for the shapes on the right of Figs. 5.4-5.6 exceed that of the spherical drop ($B_m = 0$) at 159.1, 928.5 and 1149.3 times, respectively.

Computational instabilities are reported at many numerical studies on this problem, see [9, 20, 48, 67, 79] and they are observed in our calculations. The numerical instabilities appear in the regions of strong shape deformations and at critical points, where a transition between branches of a solution appears. In several works, for instance [48, 79], the importance of high grid resolution in a region of high surface curvatures is mentioned but no further work is made to confirm this assumption. To overcome instabilities in our numerical calculations we reduce a step size for the parameter B_m in regions of strong surface changes and increase a grid resolution in a region of the drop tip (region of the highest curvatures) by applying an adaptive technique for grid construction on a free surface, see Section 4.2. As a consequence of a special grid construction on the free surface we come to an a-priori adaptive grid in a fluid domain by applying the Delaunay triangulation, see Fig. 3.6. It allowed us to resolve accurately the nonuniformity of the magnetic field, appearing close to the free surface. As an additional stabilisation tool we apply an under-relaxation technique for the algorithm of the free surface calculations (4.24)-(4.25) and for the global iterative process, see (2.27). It allowed us to perform calculations and get equilibrium shapes in a wide range of field intensities.

The numerical solutions do not end with the last calculated points in Figs. (5.1)-(5.3). The calculations are stopped at some values of the parameter B_m. The linear magnetisation law is valid only for weak fields and numerical results for larger values of B_m would have no physical meaning.

The results of numerical simulations confirm that the realized numerical modeling permits to follow the hysteresis effect for the drop deformation and to reproduce equilibrium drop shapes close to conical.

5.1.2   Conical shapes

The magnetic fluid drops with shapes close to conical are observed experimentally in [8] for the concentrated phase microdrops with size from 2 to 20 μm.

According to the results of numerical simulations we observe that for the magnetic fluids with susceptibility $\chi \geq 21$ in the vicinity of the symmetry axis the drop shape become acute for all solutions lying on the upper branch, see Figs. 5.2 and 5.3. Shapes, close to conical, appear after the first turning point for the increasing magnetic field and preserve their acute configuration till the second turning point for the decreasing field.

According to the numerical study in [48] the authors did not expect solutions to exist after the first turning points. The authors in [79] reported that for $\chi > 20.75 \pm 0.25$ families of equilibrium drop shapes become unstable at the first turning point and terminate. Non-overcoming numerical instabilities in [48, 79] served as a reason for such conclusions.
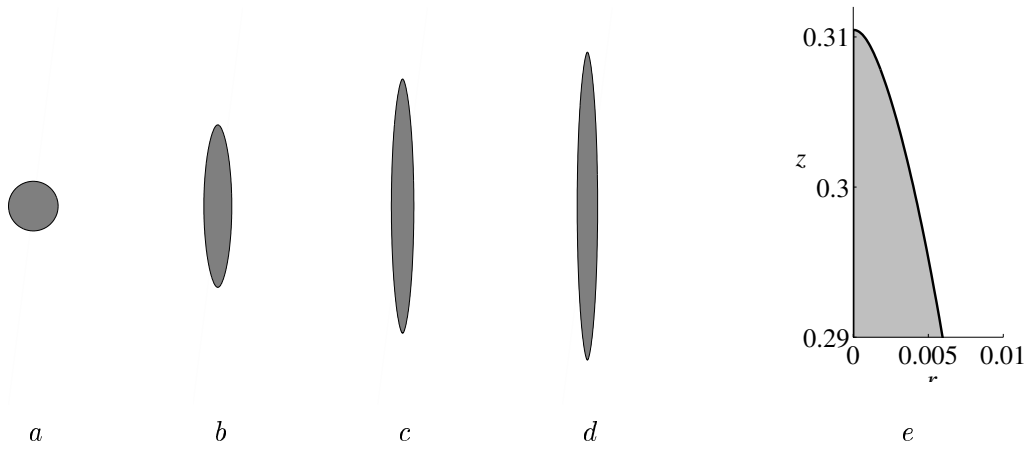
Figure 5.4: Drop deformation due to increasing magnetic field B_m: a, $B_m = 0$; b, $B_m = 10$; c, $B_m = 25$; d, $B_m = 40$; e, drop tip at $B_m = 40$. $\chi = 5$, linear magnetisation law.
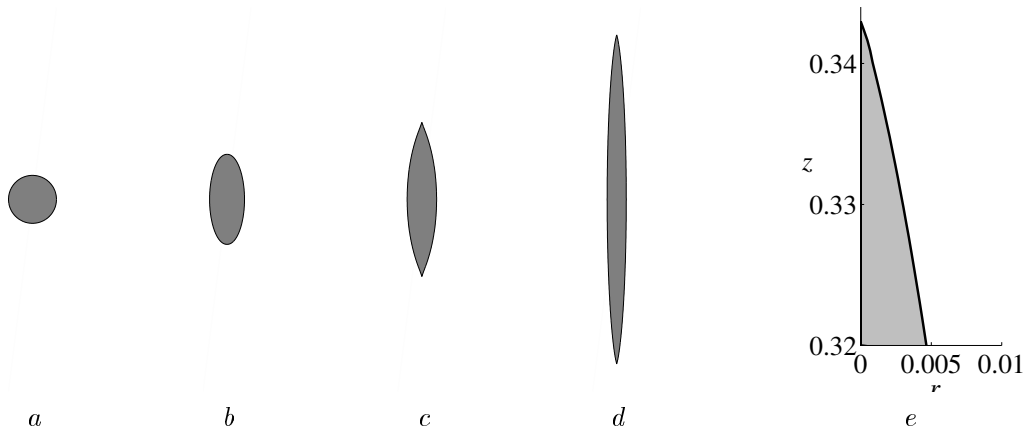

Figure 5.5: Drop deformation due to increasing magnetic field B_m: a, $B_m = 0$; b, $B_m = 5.723$; c, $B_m = 5.725$; d, $B_m = 15$; e, drop tip at $B_m = 15$. $\chi = 21$, linear magnetisation law.
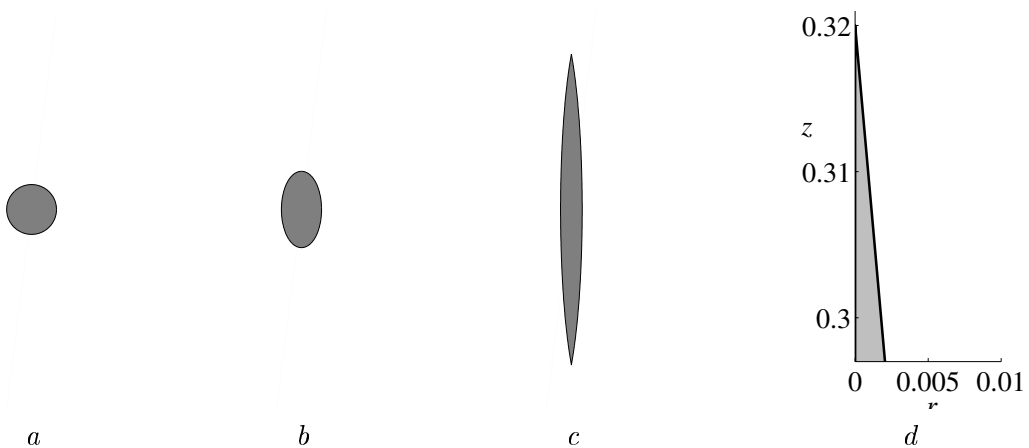

Figure 5.6: Drop deformation due to increasing magnetic field B_m: a, $B_m = 0$; b, $B_m = 8.5$; c, $B_m = 8.55$; d, drop tip at $B_m = 8.55$. $\chi = 40$, linear magnetisation law.

The internal field of a magnetisable ellipsoid is uniform and directed along the applied field. The result is shown in § 8 of [38]. Strong deviation from the ellipticity in shape forming near the symmetry axis results that the magnetic field deviates there from the uniform configuration at most. High grid resolution in the vicinity of the drop tip, see Fig. 3.6, allow us to resolve accurately field nonuniformity.

In Fig. 5.7 we present the radius of the mean curvature at the drop tip $R(0)$ dimensionless over the radius of spherical drop R_0 for different values of the applied magnetic field B_m. The radius $R(0)$ is calculated as a reciprocal value of the mean curvature, approximated locally by the finite-difference approach, see Section 4.2,

$$R(0) \approx \frac{1}{-(RZ')'/(2RR')|_{s=0}}.$$
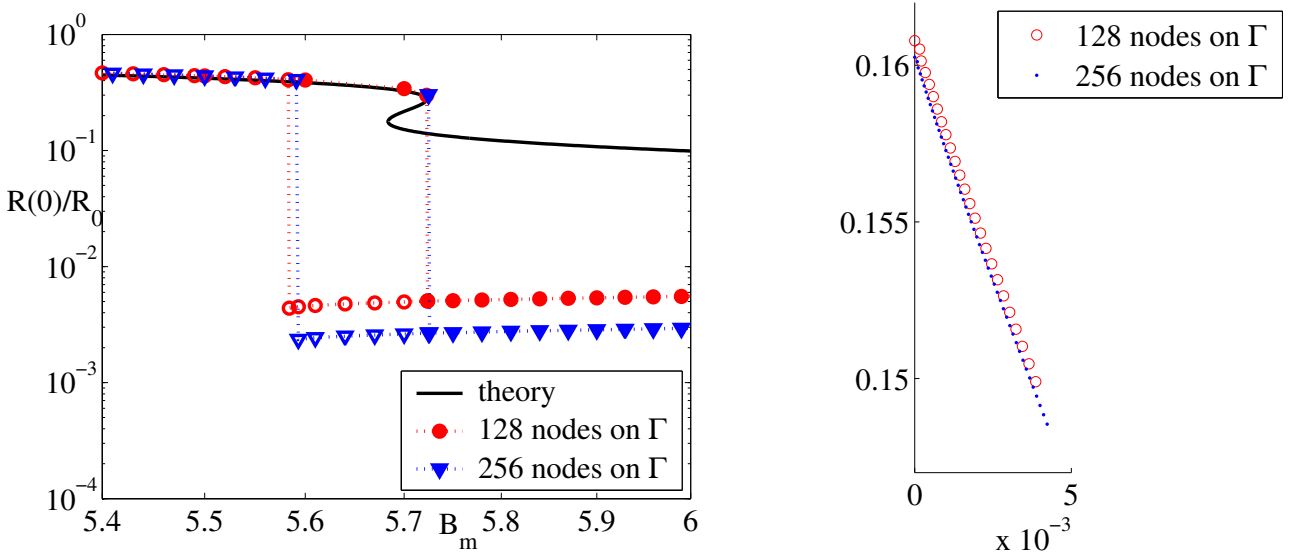
Figure 5.7: Left: the radius of the mean curvature at the drop tip $R(0)$ dimensionless over the radius of spherical drop R_0 for different values of the applied magnetic field B_m; right: shapes at the first turning point $B_m = 5.724$. $\chi = 21$, linear magnetisation law.

In the case of zero magnetic field the ratio $R(0)/R_0$ equals 1. Increasing magnetic field decreases the radius of curvature. Formation of conical points means that the radius of curvature must go to zero or the curvature must take an infinite value. It results in singular solutions for the system of governing equations, describing the problem. To resolve singularities the mathematical model should be modified. We decided to leave the model without any modifications and try to get conical shapes approximately by increasing grid resolution in the vicinity of the drop tip. Shapes close to conical are obtained numerically, see Fig. 5.7 on the right.

Several observations can be pointed out from Fig. 5.7. Theoretical and numerical results coincide for the increasing field till the first turning point ($B_m = 5.724$) and for the decreasing field after the second turning point ($B_m = 5.583$). We conclude that spheroidal approximation has a range of validity which depends on the fluid susceptibility and intensities of the magnetic field. Increase in grid resolution from 128 to 256 nodes on the free surface Γ (corresponding grid configurations can be seen in Fig. 3.4) changes field intensities at the turning points, where transitions between branches of solution appear, by less than 0.2%. We conclude that grid refinement does not show qualitative changes in solution behaviour. The surfaces, represented by 256 nodes, will be closer to conical ones than those built with 128 points, because of closer

to zero values of the radius $R(0)$. It follows that the calculated results are sensitive to grid refinement when shapes close to conical are formed.

Several investigations are made to study appearance of conical interfaces as equilibrium shapes of a magnetic fluid drop, see [18, 60, 69, 71]. Consider a conical interface with an angle 2α. The curvature of a cone $\mathcal{K}$ is inversely proportional to the distance from the cone tip ρ as follows

$$2\mathcal{K} = \frac{1}{R_1} + \frac{1}{R_2} = \frac{1}{\infty} + \frac{\cot\alpha}{\rho} = \frac{\cot\alpha}{\rho}.$$

From a balance between magnetostatic and surface tension forces for fluids with constant permeabilities, i.e. from the Younge-Laplace equation (2.11) for $M = \chi H$

$$\sigma\mathcal{K} = \frac{\mu_0}{2}\chi H^2 + \frac{\mu_0}{2}\chi^2 H_n^2 + C$$

we can get that $H = O(1/\sqrt{\rho})$ in a cone. The magnetic potential satisfying Laplace's equation inside and outside the cone can be expressed in spherical coordinates (ρ, θ, φ) with the tip of the cone at the origin as follows, see [18, 60, 71]

$$
\begin{aligned}
u_1 &= u_0 + c_1\rho^{1/2}P_{1/2}(\cos\theta), & 0 \leq \theta \leq \alpha \\
u_2 &= u_0 + c_2\rho^{1/2}P_{1/2}(-\cos\theta), & \alpha \leq \theta \leq \pi
\end{aligned}
$$

where c_1 and c_2 are constants, $P_{1/2}$ is the Legendre function of order $1/2$ and the line $\theta = 0$ or π is the symmetry axis of the cone. The boundary conditions on the interface (2.13) lead to an homogeneous linear system which has nontrivial solutions if and only if

$$\frac{\mu_1}{\mu_2} = -\frac{P'_{1/2}(-\cos\alpha)P_{1/2}(\cos\alpha)}{P'_{1/2}(\cos\alpha)P_{1/2}(-\cos\alpha)}, \tag{5.1}$$

where the prime denotes derivative with respect to the argument, see [18, 60]. The relation (5.1) allows to construct a dependence of a cone angle as a function of the permeability ratio, see Fig 5.8. The theory predicts that there exist $\chi^* \approx 16.6$, corresponding to $\alpha \approx 30°$, such that for $\chi < \chi^*$ no conical solution exists. We notice here that $\chi^* < \chi_c \approx 20.5$, see Section 5.1.1, where χ_c is a lowest value of χ for which hysteresis takes place. It means that for fluids with $\chi^* \leq \chi < \chi_c$ conical shapes can appear without hysteretic behaviour of a solution.

From theoretical results follows that fluids with $\chi \geq \chi_c$ can form conical shapes and according to our numerical results we can conclude that such shapes lie on the upper branch of a solution curve, see Figs. 5.2, 5.3. The numerical results confirm a conclusion of a semi-analytical approach in [44] showing that the solutions on the upper branch of hysteretic curve are not spheroidal but instead have singular tips. They found that for the applied field H_0 larger than a second turning point, a drop with conical tips has a lower energy and a larger aspect ratio compared to that of the elongated spheroid by Bacri&Salin in [8]. Therefore, it is energetically favourable to have a drop with conical tips at a sufficiently large field.

It is worth to mention that for $\chi > \chi^*$ two different equilibrium cone angles are possible, see Fig. 5.8. According to the argumentation in [44] the larger cone angle corresponds to an unstable equilibrium, where the conical interface for the smaller angle is stable against small perturbations of the cone angle α.

We measured the cone angle of the numerically obtained shapes for $\chi = 21$ and compared it with the theoretical predictions in [18, 60], see Fig. 5.9. The theoretical angle is the smallest from the predicted ones, see Fig. 5.8. The numerical angle is calculated with MATLAB from the polynomial curve fitting of 20 points of the numerical shape to the linear function in a least
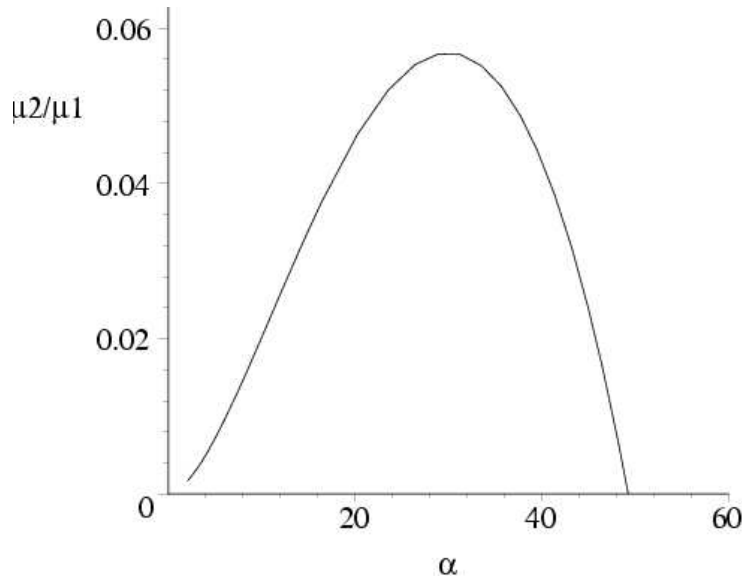
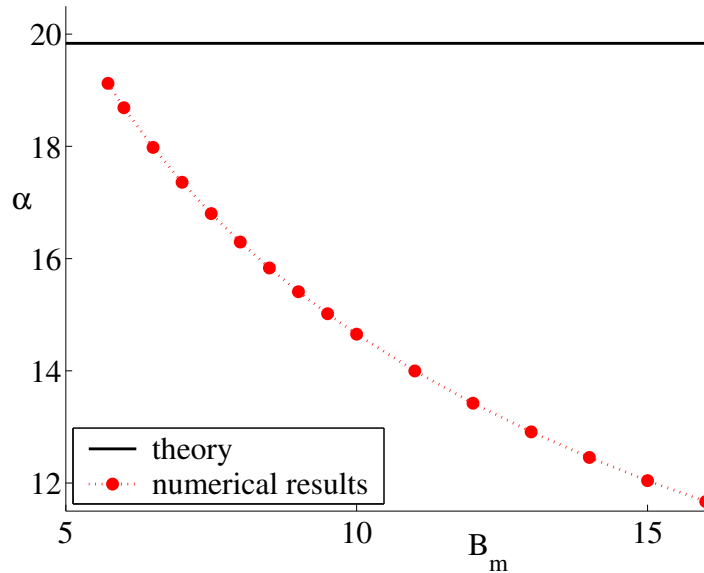Figure 5.8: Cone angle as a function of the permeability ratio. Theoretical results in [18, 60].

Figure 5.9: Cone angle as a function of the applied magnetic field B_m: $\chi = 21$ ($\mu_2/\mu_1 = 1/22 \approx$ 0.0455); theoretical results in [18, 60], see also Fig. 5.8.

square sense. The points lie close to the axis and present only the 0.06-th part of the whole surface length, see Fig. 5.7 on the right.

The theory and numerics is in the rather good agreement for the conically formed shape, corresponding to the first turning point at $B_m = 5.724$. The difference is less than 4%. Increase in the applied field results in decrease of the cone angle of the numerically obtained shapes, see Fig. 5.9. Thus, the deviation between theoretical and numerical results increases with the increasing field.

Experimentally the cone measurements are made in [71] for the limit case, i.e. $\mu_2/\mu_1 = 0$. From the experiment they got that the cone angle α is greater than 45°, whereas $\alpha \approx 49.3$ is predicted by the theory in [71]. An existence of any other experimental studies about the cone measurements does not known for us. Experimental verification of the theoretical and numerical results in Fig. 5.8 and Fig. 5.9 would be interesting.

Theoretical studies in [18, 60, 71] are approximate due to dealing with the governing equations only in a region of a cone. An open question of such analysis is how a local conical solution may be joined with the rest of the shape of the drop. A deeper insight to this problem is done in [44, 69].

A semi-analytical approach is applied in [44] to analyse static singular shapes of a fluid drop. An assumption is made that H_z is independent of r. A drop surface is approximated by matching a spheroid with two cones in a tip region of a relative size 10^{-4}. The resulting integral equation are solved numerically. The authors find that a stable drop with conical tips exists only above a threshold field and that such a drop is energetically favoured compared to the spheroidal shape at a sufficiently high field.

A slender-body theory is used in [69] to determine the approximate static shape of a conically ended magnetic fluid drop. The authors simplify the governing equations using the assumption of slenderness $b/a << 1$ and neglecting the effect of the normal component of the magnetic field to the surface, supposing $H_n = 0$. The model equations are reduced to an ordinary differential equation for the fluid intensity, coupled to an algebraic equation for the pressure balance at the interface.

The slender-body approach allows to find that for the large Bond number the aspect ratio a/b of conical shapes is proportional to $B_m^{3/7}$ as $B_m \to \infty$, see Fig. 6 in [69]. This observation coincides with those for the spheroidal shape approximation of the theory [8], see Fig. 5.10. Numerically we get that a/b is proportional to B_m^3, which is also consistent with the theoretical results but in the region closer to the first turning point.
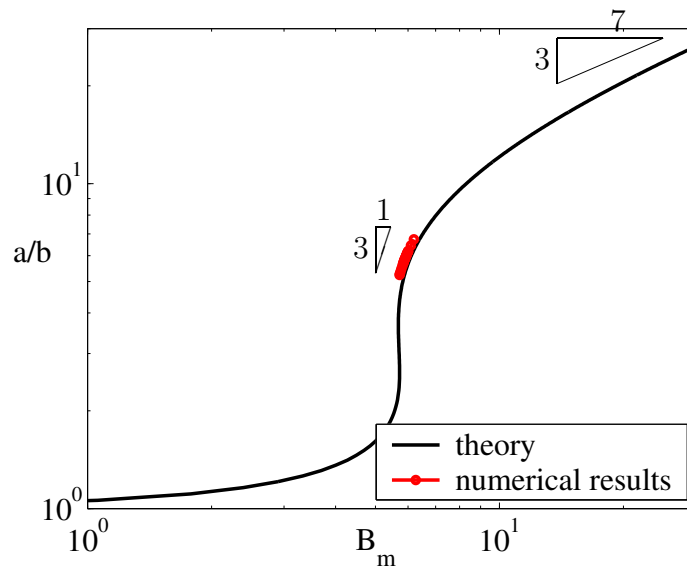

Figure 5.10: The aspect ratio of the drop as a function of the applied magnetic field: $\chi = 21$, linear magnetisation law.

The analyses in [44, 69] lead to relationships between the permeability ratio, the cone angle, the aspect ratio of the drop and the magnetic field B_m^* at which a conical end is first observed. These approaches are more thorough than those in [18, 60, 71], where as a result only the relation (5.1) between the permeability ratio and the cone angle follows. The approaches in [44, 69] are applied to the case of large drop deformations and pointed ends ($B_m \geq B_m^*$), but are inappropriate for the case of rounded ends and small deformations. Thus, our numerical study has some advantages, allowing to get the solution in the whole range of field intensities.

5.2 Nonlinear magnetisable fluids

In the previous section only linear magnetisable fluids are considered. The linear magnetisation law $M = \chi H$ is a reasonable assumption in the region of weak magnetic fields, whereas nonlinear magnetisation is a necessary requirement for the problem modeling in a wide range of field intensities.

The results of this section are for nonlinear magnetisable fluids following the Langevin law

$$M(H) = M_s P(\gamma H), \quad P(t) = \coth t - \frac{1}{t}, \quad \gamma = \frac{3\chi}{M_s}.$$

The physical meanings of the parameters can be understood by examining the asymptotic behaviour of $M(H)$ for small and large values of H while holding M_s and γ fixed

$$\lim_{H \to 0} M(H) = \frac{1}{3} M_s \gamma H = \chi H, \quad \lim_{H \to \infty} M(H) = M_s.$$

The parameter χ is the initial slope of the curve relating magnetisation to field strength, see the right picture of Fig. 5.11, M_s is the saturation magnetisation.

In the left picture of Fig. 5.11 the numerical dependencies of drop deformations upon the applied magnetic field H_0 for nonlinear magnetisable fluids with the magnetic susceptibility $\chi = 21$ and different values of the dimensionless parameter $W = \mu_0 M_s^2 V^{1/3}/(2\sigma)$ (dimensionless analog of the saturation M_s) are compared with the spheroidal drop approximation for linear magnetisable fluid in [8]. In the region of weak fields $H_0 \in [0, 0.35]$ kA/m the numerical results for different values W are close to each other and differ not strongly from the theoretical approximation for the linear magnetisable fluid (black solid line). The results show that nonlinear magnetisable drops behave similarly to linear magnetisable drops at low field strengths when drop deformations are small. This fact follows from the behaviour of the magnetisation curves in this region of fields, see the left picture of Fig. 5.11. To be correct with interpreting data from the left picture we should point that the field intensity H_0 in air corresponds to the magnetic filed with a smaller intensity inside of the fluid. The field $H_0 = 0.378$ kA/m (it corresponds to the first turning point $B_m = 5.724$, see Fig. 5.2) produces a uniform field with intensity $H_i = 0.078$ kA/m inside a spherical drop, see vertical dashed lines. For the relation between H_0 and H_i see for instance [17] or equation (5.2) from the following subsection. The region of weak fields $H_0 \in [0, 0.35]$ corresponds to $H_i \in [0, 0.07]$ inside of the fluid, where magnetisation laws do have linear behaviour.

From the numerical results of Fig. 5.11 we have that a larger W results in a more elongated shape. The largest possible elongation for the fixed H_0 corresponds to the case of the linear magnetisable fluid (a consequence of the magnetisation law behaviour). The drop elongates monotonically under increasing field with tendency to take unchangeable configuration in the region of fluid saturation. An analogous qualitative behaviour of the drop elongation is observed experimentally in [5].

5.2.1 Comparison with spheroidal shapes

If we assume that the drop shape is spheroidal then the drop elongation for every field intensity can be determined by applying a theoretical approach, so-called, the virial method in [17, 72]. The virial method in contrast to the theoretical studies in [8, 14] allows to consider nonlinear magnetisable fluids.

The field strength within a spheroid is uniform and is associated with the external field strength H_0 by means of the relationship

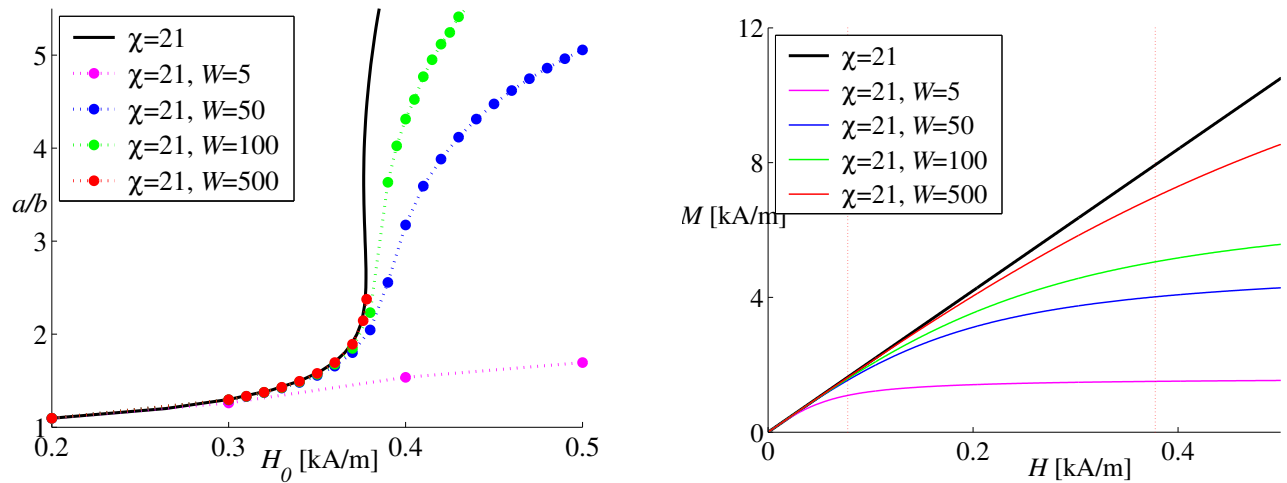$$H_i + M(H_i)n_x = H_0, \tag{5.2}$$

Figure 5.11: Left: the dependence of the drop elongation upon the applied magnetic field: $\chi = 21$, nonlinear magnetisation law; black solid line corresponds to the spheroidal drop approximation in [8] for linear magnetisation law, point markers present numerical results. Right: magnetisation law for different fluids.

where H_i is the field strength inside the drop, see for instance [17]. Here, n_x is the shape dependent demagnetisation factor

$$n_x = \frac{1-e^2}{2e^3}\left(\ln\frac{1+e}{1-e} - 2e\right), \tag{5.3}$$

where $e^2 = (1 - b^2/a^2)$ is the eccentricity of a spheroid meridian, b and a denote minor and major axes of a spheroid.

The virial method yields the following dependence

$$\frac{\mu_0(3V/4\pi)^{1/3}M^2}{4\pi\sigma} = f(e), \tag{5.4}$$

where

$$f(e) = \frac{1}{2\pi}\frac{(3-2e^2)(1-e^2)^{1/2}/e^2 - (3-4e^2)\arcsin e/e^3}{(1-e^2)^{7/6}\left((3-e^2)\ln\left((1+e)/(1-e)\right)/e^5 - 6/e^4\right)}. \tag{5.5}$$

The relation (5.4) corresponds to equation (4.29) in [17] and equation (5) in [72] but is written their in Gauss-units. We have that $\tilde{M} = \sqrt{\mu_0/(4\pi)}M$, where tilde is used for the Gauss-field and the quantity without tilde is in Si-units.

Let us substitute M to the relation (5.4) in the Langevin form

$$M(H_i) = M_s P(\gamma H_i) = M_s\left(\coth\left(\gamma H_i\right) - \frac{1}{\gamma H_i}\right), \quad \gamma = \frac{3\chi}{M_s}$$

for H_i defined from (5.2). We get the nonlinear dependence of the eccentricity of the equilibrium drop configuration e upon γ for different values $W = \mu_0 M_s^2 V^{1/3}/(2\sigma)$

$$\frac{1}{2\pi}\left(\frac{3}{4\pi}\right)^{1/3}WP^2(\gamma h_i) = f(e), \quad \gamma = \frac{3\chi H_0}{M_s},$$

where $h_i = H_i/H_0$. Applying the Newton method we find values of e ($a/R_0 = (1-e^2)^{-1/3}$) for the given W and γ. The corresponding dependences are drawn by black lines in Fig. 5.12. The

curves with markers present solution families computed at fixed values of χ and W and are traced by continuation in the value of the magnetic field γ. The change in drop height with field strength is steeper for the fluids with higher W, i.e. a larger W results in a more elongated shape. From the results presented in Fig. 5.12 we see that for $\gamma \in [0, 50]$ theoretical and numerical results nearly coincide. It follows that for the taken magnetic fluids drop shapes are rather close to spheroidal configurations in a wide range of field intensities. For the modeled fluids the theory predicts a monotone behaviour of the dependencies with tendency to take unchangeable surface configurations for strong fields, see black lines in Fig. 5.12. For $\gamma > 50$ the numerical results show a qualitative difference with the theory. A larger applied field produces a less elongated shape. Such a 'non-physical' behaviour showed by numerical results (an experimental observation of the drop elongation in saturation can be found in [5]) are discussed in the following section.
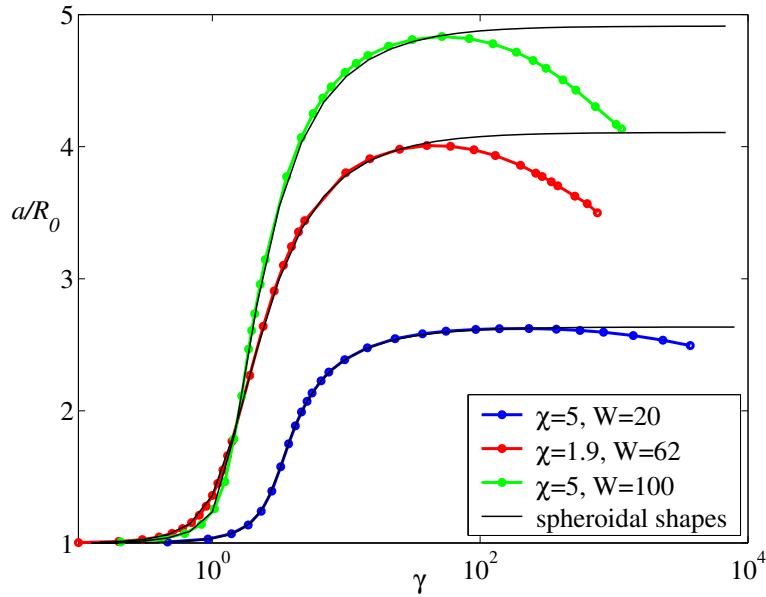
Figure 5.12: The dependence of the drop elongation upon the dimensionless magnetic field $\gamma = 3\chi H_0/M_s$: nonlinear magnetisation law; black line corresponds to the spheroidal shape approximation by the virial method, see [17, 72]; point markers present numerical results.

Fig. 5.13 displays some characteristics of the magnetic field structure inside of the drop. Namely, the left picture shows the maximum value of the r-component of the magnetic field vector $\mathbf{H} = (H_r, H_z)$ and the right picture presents the difference $H_z^{top} - H_z^{bottom}$ of z field-components at the tip of the drop and on the equator. The magnetic field is dimensionless over H_0. Fig. 5.13 (left) shows the dependence of $\max(H_r)$ over $\gamma \in [10^{-1}, 10^3]$ for different fluids. The dependencies are qualitatively the same for the modeled fluids. For the weak fields $\max(H_r)$ is nearly zero, then its value increases with increasing field till reaching the maximum at $\gamma = \gamma^*$. For $\gamma > \gamma^*$ the value of $\max(H_r)$ decreases with increasing field till value close to zero is reached in the region of strong fields, where the fluid goes to be saturated. For the fluid in saturation the permeability μ_1 tends to a permeability of a surrounding air $\mu_2 = 1$ when H_0 tends to infinity, resulting that the dimensionless internal magnetic field $\mathbf{H} = (0, 1)$ coincides with the uniform external field, see equations (2.12)-(2.16). The maximum value of H_r over all γ and for the considered fluids equals 0.004. It corresponds to the fluid with the highest $W = 100$ and the strongest drop elongation, see Fig. 5.12. We conclude that the magnetic field inside of the modeled fluids is vertically directed.

A judgement on the field uniformity can be made from the Fig. 5.13 (right) where the relative
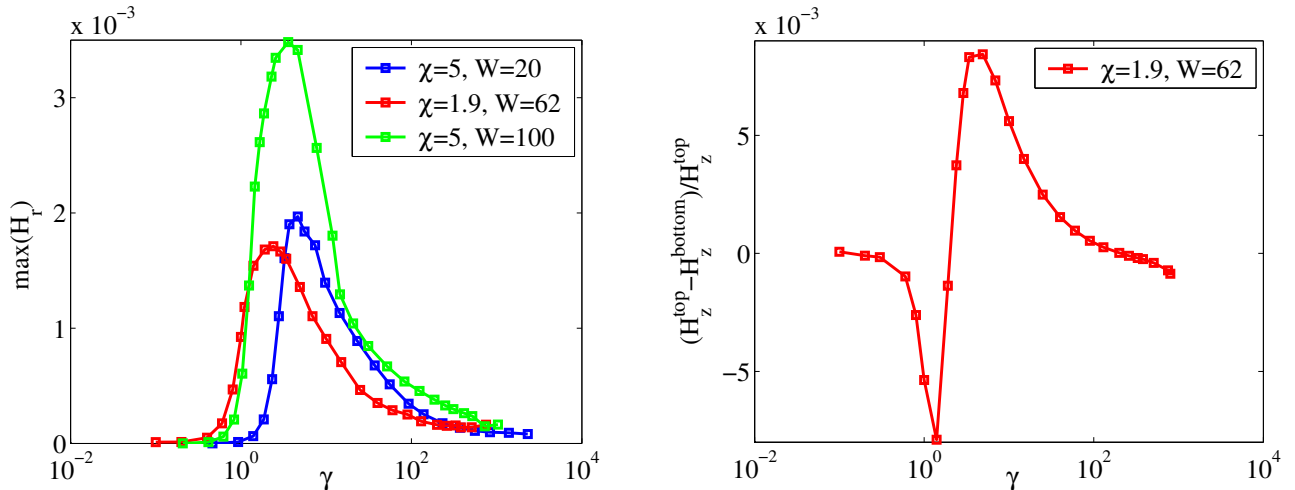
Figure 5.13: Characteristics of the magnetic field structure inside of the fluid drop upon the applied magnetic field. The magnetic field $\mathbf{H} = (H_r, H_z)$ is dimensionless over H_0. Variables H_z^{top} and H_z^{bottom} denote z-component of the field vector at the tip of the drop and on the equator, respectively.

difference between H_z^{top} and H_z^{bottom} is presented. The fluid with the parameters $\chi = 1.9$, $W = 62$ is considered. A uniform field corresponds to a zero difference. For weak fields (field uniformity due to spheroidal shapes) and for strong fields (field uniformity due to the fluid saturation) values of $H_z^{top} - H_z^{bottom}$ are close to zero. For $\gamma \in [10^0, 10^2]$ the difference grows. The uniformity is disturbed by the deviation of equilibrium shapes from spheroidal configurations but the divergence is not so strong. The difference is not larger than 1%. The strongest deviation from the field uniformity are expected for shapes close to conical, which can be presented only for fluids with the magnetic susceptibility $\chi \geq \chi^* \approx 16.6$.

5.2.2 Numerical difficulties for saturated fluids

The aim of this section is to clarify the reason for the qualitative difference between numerical and theoretical results in the region of strong fields ($\gamma > 50$), see Fig. 5.12.

Let us start from the deeper insight to the model equations. We reformulated the Young-Laplace equation (2.17) as follows

$$Z'' = R'F, \quad R'' = -Z'F, \quad F = f - \frac{Z'}{R} + C, \quad 0 < s < 1; \tag{5.6}$$

$$R(0) = 0, \; Z'(0) = 0; \quad Z(1) = 0, \; R'(1) = 0; \tag{5.7}$$

$$f = -WL\left[\frac{2}{3\chi}\ln\frac{\sinh(\gamma H)}{\gamma H} + \left(P(\gamma H)\frac{H_n}{H}\right)^2\right], \quad W = \frac{\mu_0 M_s^2 V^{1/3}}{2\sigma}, \quad \gamma = \frac{3\chi}{M_s}H_0. \tag{5.8}$$

Here H is the magnetic field dimensionless over H_0. For details see Chapter 4 and equations (4.12), (4.13) and (4.15).

For strong fields, when $\gamma \to \infty$, we have the following asymptotic behaviour for terms in

the expression for the function f

$$\lim_{\gamma \to \infty} \ln \frac{\sinh{(\gamma H)}}{\gamma H} = \lim_{\gamma \to \infty} \ln \frac{e^{\gamma H} - e^{-\gamma H}}{2\gamma H} = \lim_{\gamma \to \infty} \gamma H, \tag{5.9}$$

$$\lim_{\gamma \to \infty} \left(P(\gamma H) \frac{H_n}{H} \right)^2 = \lim_{\gamma \to \infty} \left(\left(\coth{(\gamma H)} - \frac{1}{\gamma H} \right) \frac{H_n}{H} \right)^2 = \left(\frac{H_n}{H} \right)^2.$$

The first term tends to infinity with increasing γ, whereas the second term takes a finite value from the interval $[0, 1]$. The 'big' term (5.9) is compensated by the constant C in the expression of the function F, where the constant C is fixed by the relation (4.11)

$$C = -\frac{2}{R^2(1)} \left(R(1) + \int\limits_0^1 RR'f ds \right).$$

It results in a finite value for the expression $(f + C)$ and as a consequence in a finite value for the curvature of the surface. An arithmetic with big numbers in calculating the function F produces an additional numerical error and can influence strongly the accuracy of the numerical results. To avoid this effect let us return to the mathematical model of the problem, namely to the equation (2.10). The pressure of the fluid can be specified differently, see for instance [14]. In no-gravity case the pressure can be expressed as

$$p = \mu_0 \int\limits_0^H M dH + p_1 \quad \text{or} \quad p = \mu_0 \int\limits_{H_0}^H M dH + \tilde{p}_1, \tag{5.10}$$

where p_1 and $\tilde{p}_1$ denote pressures at the points, where $H = 0$ or $H = H_0$, respectively. Differences appear in the value of constant C, which is unknown and is fixed during calculations. We used the first situation for the mathematical model described in Section 2. The only difference in the model equations for different pressure expressions (5.10) is in the change of the function f for the Young-Laplace formulation (5.6)-(5.8). We get

$$f = -WL \left[\frac{2}{3\chi} \ln \frac{\sinh{(\gamma H)}}{\sinh{(\gamma)H}} + \left(P(\gamma H) \frac{H_n}{H} \right)^2 \right].$$

We have than that

$$\lim_{\gamma \to \infty} \ln \frac{\sinh{(\gamma H)}}{\sinh{(\gamma)H}} = \lim_{\gamma \to \infty} \ln \frac{e^{\gamma(H-1)}}{H} = \lim_{\gamma \to \infty} \gamma(H-1). \tag{5.11}$$

In contrast to (5.9) now the 'big' term is suppressed by the factor $(H - 1)$ tending to zero in the saturation.

A suggested modification of the mathematical model improved the quality of the numerical results, see Fig. 5.14. Unfortunately, the calculations could not be proceeded after the last calculated point ($\gamma \approx 100$). The numerical scheme becomes unstable for $\gamma > 100$.

In this section we mention also the other numerical problem which becomes pronounced in the region of strong fields. An accuracy in calculating the magnetic field H over the surface and its smoothness can play an important role when $\gamma \to \infty$, see (5.11).
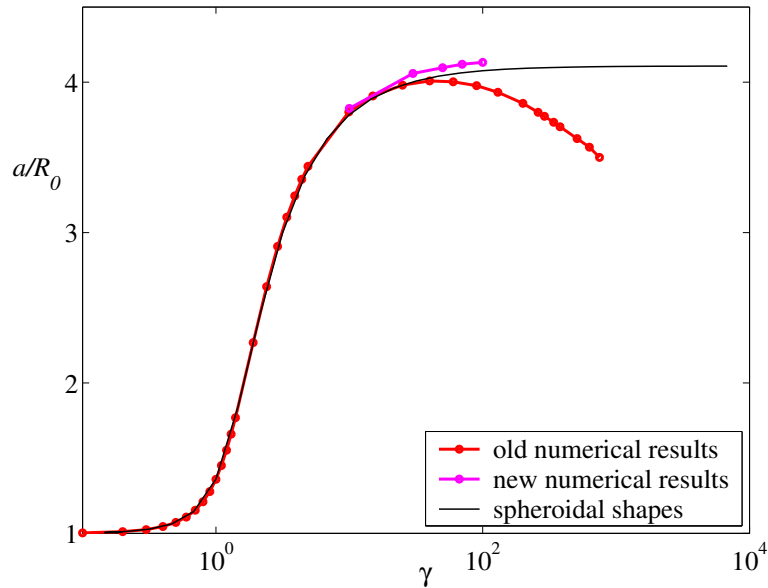
Figure 5.14: The dependence of the drop elongation upon the dimensionless magnetic field $\gamma = 3\chi H_0/M_s$: nonlinear magnetisation law, $\chi = 1.9$, $W = 62$; black line corresponds to the spheroidal shape approximation by the virial method, see [17, 72].

Axisymmetric potential. Losing accuracy near the axis in BEM formulation.

For the magnetic fluid in saturation the permeability μ_1 tends to the permeability of a surrounding air $\mu_2 = 1$ when the applied field H_0 tends to infinity. The dimensionless magnetostatic problem (2.12)-(2.16) takes the form

$$-\nabla \cdot (\nabla u_i) = 0, \quad \text{in } \Omega_i;$$

$$u_1 = u_2, \quad \frac{\partial u_1}{\partial n} = \frac{\partial u_2}{\partial n} \qquad \text{on } \Gamma,$$

$$u_2 = z, \quad (r, z) \to \infty, \tag{5.12}$$

$$u_1 = 0, \quad u_2 = 0 \quad \text{for } z = 0.$$

The exact solution of the problem (5.12) is given by

$$u_1(r, z) = z \quad \text{in } \Omega_1, \quad u_2(r, z) = z \quad \text{in } \Omega_2.$$

To solve numerically the magnetostatic problem (5.12) we apply a coupled strategy of boundary and finite element methods, see Section 3.4. The numerical solutions are thought to be found in the space of linear functions for the potential u_1 in Ω_1 and in the space of piecewise constant functions for the normal derivative of the potential $\partial u_1/\partial n$ on the free surface Γ. It appeared that the simple exact solution of the magnetostatic problem (5.12) can not be accurately resolved by the coupled BEM-FEM approach in axisymmetric case.

For the test calculations two different configurations for the free surface Γ are taken, see Fig. 5.15. The surface Γ_1 is defined as a part of a circle and the surface Γ_2 corresponds to the shape in Fig. 5.14 for new numerical results with $\gamma \approx 100$. The surface Γ_1 has a uniform points distribution, whereas for the surface Γ_2 grid points are concentrated near the tip. Both surfaces are approximated by the cubic spline. The left picture of Fig. 5.15 presents difference

between the exact solution of the problem (5.12) and numerically calculated one by the coupled BEM-FEM approach.
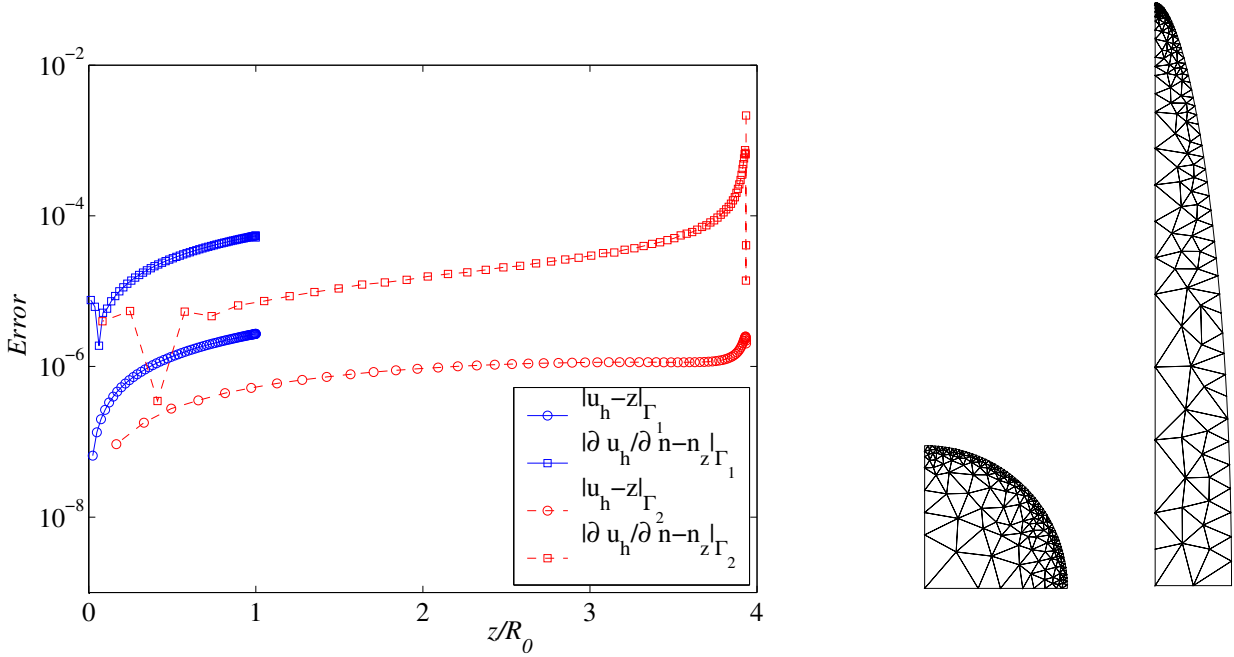

Figure 5.15: Numerical error as a function of the free surface position for the domain Ω_1 with $\Gamma = \Gamma_1$ and $\Gamma = \Gamma_2$, see on the right side. For the potential error $|u_h - z|$ the difference is taken at the grid points. For the error in the normal derivative of the potential $|\partial u/\partial n - n_z|$ the difference is calculated in the middle point of subsplines. n_z denotes z-component of the external normal vector to the surface Γ.

Fig. 5.15 shows that the numerical solutions lose accuracy near the axis of symmetry (the largest z value) for the case of the elongated drop (dashed lines). An analogous effect is discussed in [50] where the boundary integral technique is applied for the computation of the axisymmetric flow. The authors reported that the cause of the difficulty is in the particular behaviour of the integrands in the BEM-formulation, when a source point ξ^0 lies near the symmetry axis. For the potential problem, see Section 3.1, we have the following asymptotic behaviour of kernel functions in boundary integral operators

$$
\begin{aligned}
\lim_{\xi \to \xi^0, r^0 = 0} a_1(\xi^0, \xi) &= \frac{K(0)}{2\pi}, \\
\lim_{\xi \to \xi^0, r^0 = 0} a_2(\xi^0, \xi) &= -\frac{K(0)}{4\pi} + O\left(\frac{1}{r^0}\right).
\end{aligned}
$$

The quantity $1/r^0$ in the limit for the kernel function $a_2(\xi^0, \xi)$ grows unboundendly as ξ^0 approaches the axis of symmetry, resulting in strong variation for the integrand.

To overcome the loss of accuracy for the numerical integration near the symmetry axis the authors in [50] suggested to apply adaptive integration methods for computing boundary integrals. An efficiency of the adaptive integration for calculating boundary integrals in axisymmetric problems are reported in [50] on the base of numerical tests. They compared adaptive quadrature approach with the non-adaptive method, where integrals (regular and weakly singular) are calculated with 6-point Gaussian quadratures.

The numerical results in Fig. 5.15 are calculated without using adaptive quadratures. We apply 12 points Gaussian quadrature formulas for calculating regular integrals and 8 points

logarithmically weighted Gaussian formulas for weakly singular integrals. An application of adaptive integration (a tolerance set to 10^{-12}), suggested in [50], is not improve the accuracy of the numerical results. The solutions for non-adaptive and adaptive integration are identical. We assume that the loss of accuracy near the symmetry axis appears due to the concentration of grid points near the symmetry axis. The numerical results for uniform points distribution on the surface, see Fig. 5.15, solid lines, show the smooth behaviour of the discretisation error near the symmetry axis.

Numerical difficulties near the symmetry axis appear in BE-formulation of the axisymmetric problem (5.12). The finite element method does not exhibit the same sensitive behaviour of the numerical solution, see Section 6.

Chapter 6

Equilibrium shapes of a bubble inside a magnetic-fluid layer

The subject of this chapter is a problem on equilibrium shapes of a bubble inside an infinite volume of magnetic fluid under the action of a uniform applied magnetic field.

It is reported in [17] that in a fashion analogous to the elongation of the magnetic-fluid drop in a non-magnetic surrounding in the direction of the field the same occurs upon placing a drop of non-magnetic medium (bubble) in the magnetic fluid. The physical reasons of the deformation in both cases, however, differs. Stretching of the magnetic fluid drop occurs because of an action of the magnetic surface stress. When considering the bubble surrounded by a magnetic fluid, then the fluid acts towards the bubble flattening. However, distribution of the pressure in the magnetic fluid, associated with the non-uniformity of the field outside the bubble, acts contrariwise. The non-uniformity of the magnetic field inside the fluid influences stronger the surface change than the pressure jump at the fluid-air interface, see e.g. [5], thus causing the elongation of the bubble in the direction of the field.

6.1 Governing equations

We consider a freely suspended axisymmetric bubble of a prescribed volume surrounded by the magnetic fluid. We assume that the field intensity vector $\mathbf{H_0}$, applied at infinity, is parallel to the z-axis, i.e. $\mathbf{H_0} = (0, 0, -H_0)$. Mathematically the problem statement for calculating equilibrium shapes of a bubble is similar to those formulated for the equilibrium shapes of a magnetic fluid drop (2.12)-(2.17). The difference now is that the fluid domain Ω_1 is unbounded, whereas the air domain Ω_2 is bounded by the free surface Γ, see Fig. 2.2 and Fig. 6.1. For simplicity of the representation in this Chapter we remind the formulation of the dimensionless magnetostatic problem (2.12)-(2.16)

$$-\nabla \cdot (\mu_i(|\nabla u_i|)\nabla u_i) = 0, \quad \text{in } \Omega_i; \quad \begin{aligned} \mu_1 &= 1 + \frac{M(H_0|\nabla u_1|)}{H_0|\nabla u_1|} & \text{in } \Omega_1, \\ \mu_2 &= 1 & \text{in } \Omega_2, \end{aligned} \tag{6.1}$$

$$u_1 = u_2, \quad \mu_1 \frac{\partial u_1}{\partial n} = \frac{\partial u_2}{\partial n} \qquad \text{on } \Gamma, \tag{6.2}$$

$$\lim_{(r,z) \to \infty} (u_2 - z) = 0, \tag{6.3}$$

$$\frac{\partial u_1}{\partial n} = 0, \quad \frac{\partial u_2}{\partial n} = 0 \quad \text{for } r = 0, \tag{6.4}$$

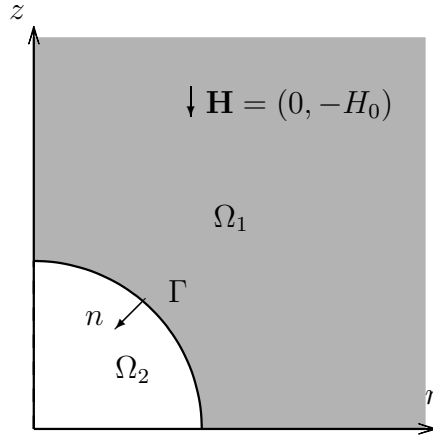$$u_1 = 0, \quad u_2 = 0 \quad \text{for } z = 0. \tag{6.5}$$

Figure 6.1: An initial computational domain in cylindrical coordinates.

The magnetisation law $M(\cdot)$ is taken in the Langevin form

$$M(H_0|\nabla u_1|) = M_s P(\gamma|\nabla u_1|), \quad P(t) = \coth t - \frac{1}{t}, \quad \gamma = \frac{3\chi}{M_s} H_0,$$

which results that the fluid permeability μ_1 is expressed as

$$\mu_1 = 1 + 3\chi \frac{P(\gamma|\nabla u_1|)}{\gamma|\nabla u_1|}.$$

The model problem is closed by the Young-Laplace equation in the dimensionless form

$$\frac{\sigma}{R_0}\mathcal{K} = \mu_0 H_0 \int\limits_1^H M(H_0 H) dH + \frac{\mu_0}{2}\left(M(H_0 H)\frac{H_n}{H}\right)^2 + C \quad \text{on } \Gamma, \tag{6.6}$$

where $H = |\nabla u_1|$ and $H_n = -\nabla u_1 \cdot \mathbf{n}$. Some changes appear in (6.6) comparing to the equation (2.17) for the magnetic-fluid drop. The integral term is taken from 1 to H instead of the integration from 0 to H as in the equation (2.17). Both formulations are correct, because the pressure of the fluid can be specified in following different ways, see for instance [14],

$$p = \mu_0 \int\limits_0^H M dH + p_1 \quad \text{or} \quad p = \mu_0 \int\limits_{H_0}^H M dH + \tilde{p}_1,$$

where p_1 and $\tilde{p}_1$ denote pressures at the points, corresponding to $H = 0$ or $H = H_0$, respectively. Differences in the Young-Laplace equation appear for the value of constant C, which is unknown a-priori and is fixed during calculations.

The other change in the mathematical model is because the normal vector on Γ changes a direction to the opposite, see Figs 2.2 and 6.1 for comparison. As a result the surface curvature K changes a sign, i.e.

$$\mathcal{K} = (RZ')'/(RR').$$

Following the idea of Chapter 4 we reformulates the Young-Laplace equation (6.6) as

$$Z'' = R'F, \quad R'' = -Z'F, \quad F = f - \frac{Z'}{R} + C, \quad 0 < s < 1; \qquad (6.7)$$

$$R(0) = 0, \ Z'(0) = 0; \quad Z(1) = 0, \ R'(1) = 0; \qquad (6.8)$$

where L and C are fixed by (4.10) and (4.11), respectively, and

$$f = f(H, H_n, L) = WL\left[\frac{2}{3\chi}\ln\frac{\sinh(\gamma H)}{\sinh(\gamma)H} + \left(P(\gamma H)\frac{H_n}{H}\right)^2\right], \quad W = \frac{\mu_0 M_s^2 V^{1/3}}{2\sigma}.$$

For details of the reformulation we refer to equations (4.12) and (4.13).

6.2   Numerical solution strategy

The problem under consideration is a coupled system of the magnetostatic equations (6.1)-(6.5) and the free surface equations (6.7)-(6.8). A solution of the magnetostatic problem (6.1)-(6.5) depends on the position of the free surface Γ, because the surface separates media of different magnetic properties. The position of the free surface as a solution of the equations (6.7)-(6.8) depends on the magnetic field configuration on it. The coupled problem (6.1)-(6.5), (6.7)-(6.8) should be solved simultaneously. Due to the complex statement we apply an iterative decoupling strategy to the equations, see for details Section 2.4. Each iteration consists of two steps. The first step is to solve the magnetostatic problem (6.1)-(6.5) for the fixed free surface Γ, the second step is to find a solution of free surface equations (6.7)-(6.8) for the given field configuration.

To solve the magnetostatic problem (6.1)-(6.5) numerically we apply the finite element method, see Section 3.3. It is possible to use a boundary element technique in the bounded region Ω_2 but it is impossible to handle the unbounded domain Ω_1 by BEM due to the non-linearity of the equation there. The coupled boundary and finite element method, which is reasonable to apply for finding equilibrium magnetic fluid drop shapes, is not worthwhile for the problem on equilibrium bubble shapes.

To solve the free surface equations (6.7)-(6.8) numerically we apply the finite-difference scheme, see Section 4.2.

Triangulation of the computational domain is adopted to the varying free surface shape during the iterative process. As a mechanism for obtaining a new grid for the magnetostatic problem after the interface position is changed, we use the Delaunay technique presented in Section 3.5.

6.3   Numerical results

Behaviour of magnetic-fluid drops and bubbles in the magnetic fluid as a function of the applied field strength is displayed in Figs 6.2 and 6.3. The variables a and b denote drop and bubble lengths along z and r axis, respectively. Fig. 6.2 presents results for the linear magnetisable fluid with the susceptibility $\chi = 5$. Fig. 6.3 displays results for the nonlinear magnetisable fluid with parameters $\chi = 1.9$, $W = 62$. Each curve is a solution family traced by continuation in the value of the dimensionless applied field B_m in Fig. 6.2 or γ in Fig. 6.3.

The results show that higher values of the applied field cause the bubble to elongate along the field direction. At very small fields the bubble deforms to a larger extent than the drop.

After reaching some field strength ($H_0 \approx 1.5$ kA/m in Fig. 6.2 and $H_0 \approx 1$ kA/m in Fig. 6.3) the drop shows stronger deformation than the bubble with the increasing field.

If we assume that the bubble shape is spheroidal then the surface elongation for every field intensity can be determined by applying a theoretical approach, so-called, the virial method [17, 72]. The corresponding dependence for the linear magnetisable fluid with the susceptibility $\chi = 5$ is drawn by a dashed solid line in Fig. 6.2. It constructed from the relation (4.35) in [17] after variable transformation from Gauss- to SI-units. We have that

$$\frac{1}{8\pi} \left(\frac{3}{4\pi} \right)^{1/3} B_m = \left(4\pi\chi - \frac{4\pi\chi^2 n_x(e)}{1+\chi} \right)^2 f(e),$$

where the magnetic Bond number $B_m = \mu_0 V^{1/3} \chi H_0^2 / (2\sigma)$, the demagnetisation factor $n_x(e)$ is defined by (5.3), the function $f(e)$ by (5.5) and the eccentricity of a spheroid $e^2 = 1 - b^2/a^2$.

In Subsection 5.2.2 for the numerical results on the magnetic-fluid drop the numerical difficulties for saturated fluids are discussed. One of the difficulty is the loss of accuracy near the symmetry axis for the numerical solution of the magnetostatic problem (5.12) when a coupled strategy of boundary and finite element methods is applied. Numerical instability is observed for $\gamma \approx 100$ and the calculations could not be proceed for $\gamma > 100$, see Fig. 6.3. The finite element technique is applied for solving the magnetostatic problem (6.1)-(6.5) in the process of finding equilibrium bubble shapes. Numerical calculations for the finite element discretisation show no computational difficulties for $\gamma > 100$, see Fig. 6.3. This observation can be considered as an additional corroboration of the hypotheses that the computational instability for the drop calculations comes from the boundary element discretisation of the magnetostatic problem. According to the numerical results we report an advantage of using finite element technique over the boundary element discretisation in application to the axisymmetric magnetostatic problem (2.12)-(2.16) in the region of strong fields.
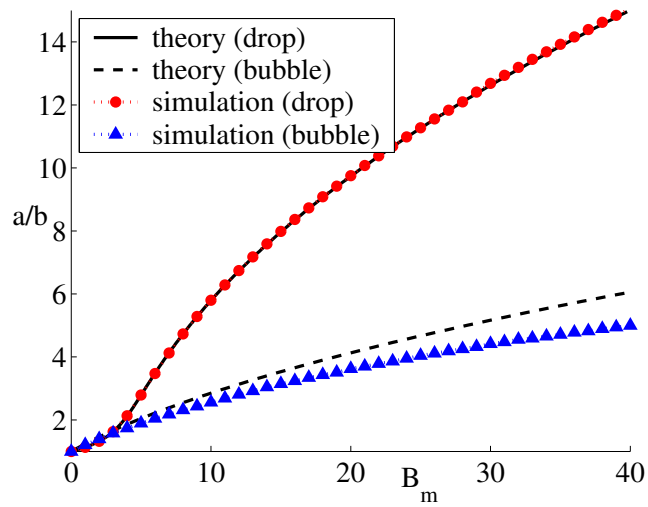
Figure 6.2: The dependence of the drop and the bubble elongation upon the dimensionless magnetic field $B_m = \mu_0 V^{1/3} \chi H_0^2 / (2\sigma)$: linear magnetisation law, $\chi = 5$. The theoretical results are obtained by the virial method, see [17, 72].
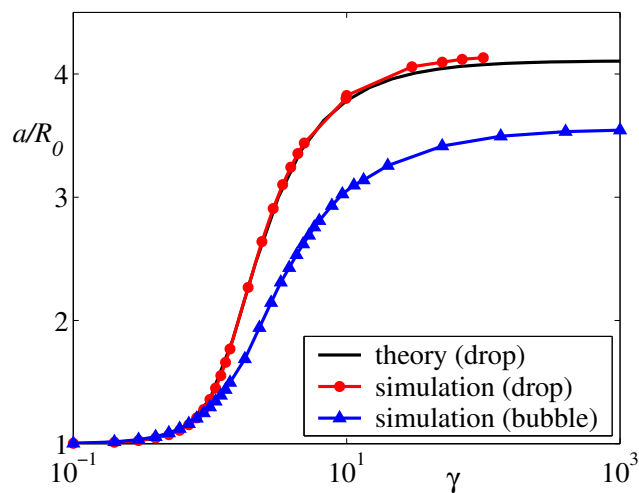

Figure 6.3: The dependence of the drop and the bubble elongation upon the dimensionless magnetic field $\gamma = 3\chi H_0 / M_s$: nonlinear magnetisation law, $\chi = 1.9$, $W = 62$. The theoretical results are obtained by the virial method, see [17, 72].

Chapter 7

Equilibrium surfaces of a magnetic-fluid layer

The subject of this chapter is a numerical study of the problem on a horizontal magnetic-fluid layer under the action of gravity and a uniform magnetic field. Equilibrium surface shapes and the critical parameters corresponding to onset of the layer instability are treated numerically.

The instability of a magnetic-fluid surface in a uniform normally directed magnetic field (Rosensweig instability or the normal-field instability) is one of the interesting phenomena of ferrohydrodynamics, see [24]. For weak magnetic fields the interface between the magnetic fluid and a surrounding gas remains flat. When the intensity of the magnetic field exceeds a critical value, the spontaneous generation of an ordered pattern of surface protuberances is produced on the surface. A stationary wave structure arises on a free surface in a threshold-like manner with the amplitude growing as the field intensity increases. This effect has been sufficiently studied experimentally [24] and theoretically [27, 28].

A nonlinear description of the instability is necessary in order to estimate the shape of peaks in a pattern and to determine what particular final pattern (hexagons, squares) occurs due to the complex nonlinear interaction. Closer theoretical study is made difficult by the necessity to solve a hydrostatic problem with unknown free surface shape and important role of magnetic field distortions on the free surface that require an appropriate solving of Maxwell's equations. Despite some recent progress, see [28], theoretical investigations based on analytical studies are still restricted to small relative permeabilities ($\mu < 1.4$) and a linear magnetisation law. A full numerical approach taking into account all nonlinear effects is necessary.

7.1 Mathematical model

We consider a semi-infinite magnetic-fluid layer with a horizontal plane free surface bounded from above by a nonmagnetic gas. We define the unperturbed plane surface by the equation $z = 0$. The system is regarded under the action of gravity and a uniform vertical magnetic field. We assume that the field intensity vector $\mathbf{H_0}$, applied at infinity, is parallel to the z-axis, i.e. $\mathbf{H_0} = (0, 0, -H_0)$. A two-dimensional cut through the three dimensional layer surface is displayed in Fig. 7.1.

The theoretical study in [27] predicted the occurrence of regular hexagonal or square pattern of peaks. This observation was confirmed experimentally in [24]. In our model we assume that the free surface of a single peak is a surface of revolution and go in the model formulation to the cylindrical coordinates (r, z). We restrict the computational domain to a single cell of the developed pattern and specify symmetry boundary conditions at the cell boundary $r = a$. Here
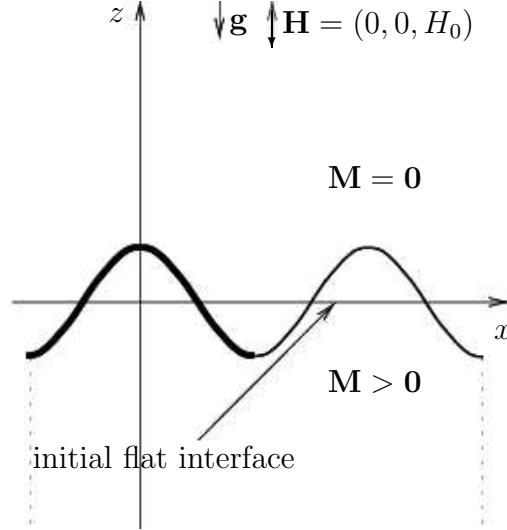
Figure 7.1: Schematical illustration of the surface deformation.

a denotes a half of the wavelength of an axially symmetric surface perturbation and is used as a characteristic length scale for the dimensionless calculations. Up to know, there is no technique available to get the wave length of the equilibrium directly from the simulation.

By restricting calculations to a single cell it is impossible to find a solitary surface patterns, recently observed experimentally in [61]. For the numerical study of a solitary surface configurations see Section 7.4.

Mathematically the problem statement for calculating axisymmetric equilibrium shapes of a magnetic-fluid layer is similar to those formulated for the equilibrium shapes of a magnetic-fluid drop (2.12)-(2.17). The formulation of the dimensionless magnetostatic problem (2.12)-(2.16) takes the form

$$-\nabla \cdot (\mu_i(|\nabla u_i|)\nabla u_i) = 0, \quad \text{in } \Omega_i; \quad \begin{aligned} \mu_1 &= 1 + \frac{M(H_0|\nabla u_1|)}{H_0|\nabla u_1|} && \text{in } \Omega_1, \\ \mu_2 &= 1 && \text{in } \Omega_2, \end{aligned} \tag{7.1}$$

$$u_1 = u_2, \quad \mu_1 \frac{\partial u_1}{\partial n} = \frac{\partial u_2}{\partial n} \qquad \text{on } \Gamma, \tag{7.2}$$

$$\frac{\partial u_1}{\partial r} = 0, \quad \frac{\partial u_2}{\partial r} = 0 \quad \text{for } r = 0, \tag{7.3}$$

$$\frac{\partial u_1}{\partial r} = 0, \quad \frac{\partial u_2}{\partial r} = 0 \quad \text{for } r = 1, \tag{7.4}$$

$$\lim_{z \to -\infty} (u_1 - h_0^1 z) = 0, \quad \lim_{z \to +\infty} (u_2 - z) = 0. \tag{7.5}$$

The space variables are dimensionless over a and the magnetic field over H_0. Domains Ω_1 and Ω_2 are vertically unbounded. The symmetry condition at the cell boundary is given by (7.3). Taking into consideration that the applied field is perturbed by the surface only locally in a neighbourhood of the interface we can use at infinity boundary conditions (7.5) for the undisturbed case $\Gamma = \{(r, z) \,|\, r \in [0, 1], z = 0\}$. These conditions define uniform magnetic field far from the free surface. The dimensionless intensity in surrounding air equals 1 at infinity. The variable h_0^1 denotes the dimensionless intensity of the magnetic field inside the fluid. The value

of h_0^1 is defined from the second of transition conditions (7.2) in the case of the unperturbed surface $z = 0$. Namely we have

$$\mu_1 \frac{\partial u_1}{\partial n} = \frac{\partial u_2}{\partial n} \quad \text{on } z = 0 \quad \Rightarrow \quad \mu_1 \frac{\partial u_1}{\partial z} = \frac{\partial u_2}{\partial z} \quad \Rightarrow \quad \mu_1(h_0^1)h_0^1 = 1.$$

For computational purposes we define asymptotic boundaries $z = z_{bottom}$ and $z = z_{top}$. The distances of these boundaries from the free surface are finite and large enough, namely $z_{bottom} = -5$ and $z_{top} = 5$. Instead of conditions (7.5) we use the following ones

$$u_1 = h_0^1 z_{bottom} \quad \text{for } z = z_{bottom}, \quad u_2 = z_{top} \quad \text{for } z = z_{top}. \tag{7.6}$$

The magnetisation law is taken in the Langevin form

$$M(H_0|\nabla u_1|) = M_s P(\gamma|\nabla u_1|), \quad P(t) = \coth t - \frac{1}{t}, \quad \gamma = \frac{3\chi}{M_s} H_0,$$

which results that the fluid permeability μ_1 is expressed as

$$\mu_1 = 1 + 3\chi \frac{P(\gamma|\nabla u_1|)}{\gamma|\nabla u_1|}.$$

The other possibility is to define the magnetisation law by the Vislovich's interpolation formula, see [73]

$$M(H_0|\nabla u_1|) = M_s \frac{|\nabla u_1|}{|\nabla u_1| + h^T},$$

which results that the fluid permeability μ_1 is expressed as

$$\mu_1 = 1 + \frac{M_s}{H_0} \frac{1}{|\nabla u_1| + h^T}.$$

Here $h_T = H_T/H_0$ and H_T is the magnetic field intensity such that $M(H_T) = M_s/2$.

The dimensionless Young-Laplace equation (2.17) is reformulated as

$$\frac{\sigma}{a}\mathcal{K} = -a\rho g z + \mu_0 H_0 \int\limits_0^H M(H_0 H)dH + \frac{\mu_0}{2}\left(M(H_0 H)\frac{H_n}{H}\right)^2 + C \quad \text{on } \Gamma, \tag{7.7}$$

where ρ is the fluid density, g denotes the acceleration of gravity, $H = |\nabla u_1|$ and $H_n = -\nabla u_1 \cdot \mathbf{n}$. The difference to the equation (2.17), formulated for the magnetic-fluid drop problem, is that the gravity appears as an additional external force in the balance equation on the free surface.

Following the ideas of Chapter 4 we reformulates the Young-Laplace equation (7.7)

$$Z'' = R'F, \quad R'' = -Z'F, \quad F = \lambda^2 L^2 Z + f - \frac{Z'}{R} + C, \quad 0 < s < 1; \tag{7.8}$$

$$R(0) = 0, \ Z'(0) = 0; \quad R'(1) = 1, \ Z'(1) = 0. \tag{7.9}$$

where

$$f = f(H, H_n, L) = -\lambda \text{Si} L\left[\frac{2}{3\chi}\ln\frac{\sinh(\gamma H)}{\sinh(\gamma)H} + \left(P(\gamma H)\frac{H_n}{H}\right)^2\right], \quad \lambda = a\sqrt{\frac{\rho g}{\sigma}}, \ \text{Si} = \frac{\mu_0 M_s^2}{2\sqrt{\rho g \sigma}}.$$

The magnetisation law is taken in the Langevin form. For the Vislovich approximation of the magnetisation law see Section 4.5 in [41]. For more details about the reformulation of the problem we refer to equations (4.12), (4.13).

The dimensionless length of the free boundary $L = \ell/a$ is fixed by the relation

$$L = \frac{1}{R(1)}. \tag{7.10}$$

To fix the constant C we use the same idea as was applied for getting the formula (4.11). Due to the boundary conditions (7.9) and the volume constraint

$$\int_0^1 ZRR'ds = 0, \tag{7.11}$$

we get

$$C = -\frac{2}{R^2(1)} \int_0^1 RR'fds. \tag{7.12}$$

The initial susceptibility χ, the dimensionless field strength γ, the dimensionless wave length of the cell λ and the parameter Si are the dimensionless parameters representing the evolution of the layer surface described by the magnetostatic equations (7.1)-(7.3) and the free surface equations (7.8)-(7.9)

$$\chi, \quad \gamma = 3\chi H_0/M_s, \quad \lambda = a\sqrt{\frac{\rho g}{\sigma}}, \quad \mathrm{Si} = \frac{\mu_0 M_s^2}{2\sqrt{\rho g \sigma}}.$$

7.2   Numerical solution strategy

The problem under consideration is a coupled system of the magnetostatic equations (7.1)-(7.5) and the free surface equations (7.8)-(7.9). A solution of the magnetostatic problem (7.1)-(7.5) depends on the position of the free surface Γ, because the surface separates media of different magnetic properties. The position of the free surface as a solution of the equations (7.8)-(7.9) depends on the magnetic field configuration on it. The coupled problem (7.1)-(7.5), (7.8)-(7.9) should be solved simultaneously.

Due to the coupled statement of the problem we apply an iterative decoupling strategy, see for details Section 2.4. Each iteration consists of two steps. At the first step we solve the magnetostatic problem (7.1)-(7.5) for the fixed free surface Γ, as the second step we find a solution of free surface equations (7.8)-(7.9) for the given field configuration. When the applied magnetic field is slowly increased, an initial free surface configuration Γ^0 is assigned in the form of a plane surface with a small perturbation (the amplitude is around 1% of the wavelength) satisfying the volume conservation condition (7.11). For the decreasing field, the initial surface approximation Γ^0 for the calculations with the new value of the applied field H_0 is defined as the calculated equilibrium shape corresponding to the preceding value H_0. Damping out of the perturbation during the iterative process was interpreted as a stability of the plane surface. Realisation of the solution with a curved surface was considered as an illustration of instability, as a result of which the initial perturbation evolves to a stationary configuration of a finite amplitude. The result of the iteration, starting from a given interface position Γ^k, calculating the magnetic field, and determining a new position of the interface Γ^{k+1}, depends strongly on the initial surface deformation Γ^0. In the bistability regime of the Rosensweig instability two

stable configurations can be resolved - a flat surface and a developed pattern. Which of these two states is numerically found, depends on the amplitude of the initial surface perturbation.

To solve the magnetostatic problem (7.1)-(7.5) numerically we apply the finite element method, see Section 3.3. An advantage of the boundary element method over the finite element method is not presented for the layer problem. A boundary element technique is impossible to use in the half-space occupied by the air, when the whole computation domain is given by $\mathbb{R}^3$. The complement of the infinite domain in $\mathbb{R}^3$ is necessarily to be bounded in order to reformulate the Laplace equation in the form of the boundary integral equation.

To solve the free surface equations (7.8)-(7.9) numerically we apply the finite-difference scheme, see Section 4.2.

7.3   Numerical results

The main numerical results of this Section are published in [11, 12, 40, 41].

By the linear stability analysis, see [63, Section 7.1], the critical wave length is estimated as

$$\lambda_c = 2\pi \sqrt{\frac{\sigma}{\rho g}}.$$

We set a radius a of a circular cell as $a = \lambda_c/2$ and get the dimensionless wave length as

$$\lambda = \pi.$$

A typical equilibrium shape of the free surface at a supercritical value of the magnetic field intensity and the corresponding structure of the magnetic field are shown in Fig. 7.2.
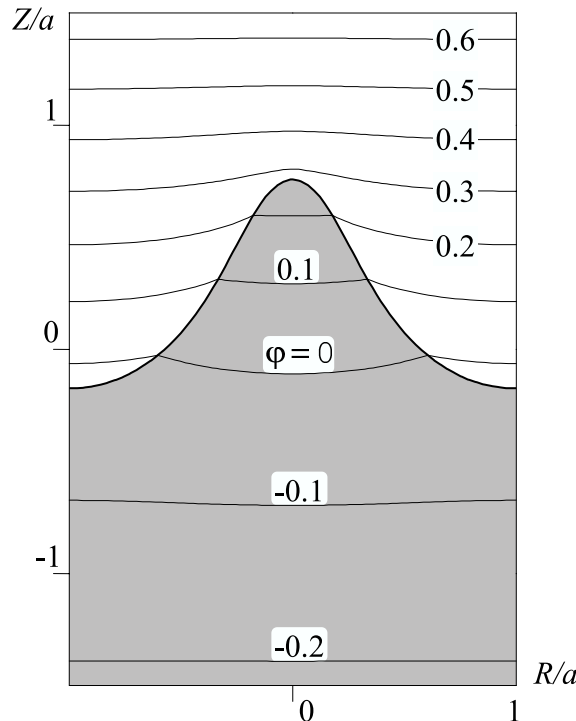

Figure 7.2: Shape of the free surface and isolines of the dimensionless magnetic potential φ at a supercritical value of the magnetic field intensity: Vislovish magnetisation law, $\chi = 2.5$, $h_T = 2.2$, $\lambda = \pi$, Si $= 100$; $\varphi = u/h_T$.

Fig 7.3 presents the dependence of the critical magnetic field intensity on the parameter Si for different values λ of the dimensionless wavelength of the pattern. At the critical magnetic

field the transition from the flat surface to the pattern of peaks appears. Numerical results are presented for the plane problem formulation, which was analysed in [40]. Fig 7.3 shows that the critical magnetic fields obtained numerically for plane perturbations are in agreement with theoretical results obtained by the linear stability analysis in [63, Section 7.1].
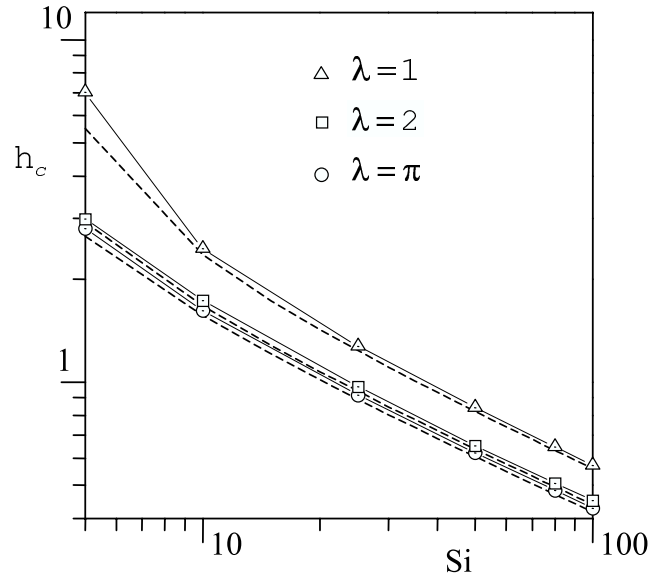

Figure 7.3: Logarithmic dependence of the critical magnetic field intensity on the parameter Si: Vislovich magnetisation law, $\chi = 2.5$. Dashed lines - theory data corresponding to $\lambda = 1$, 2 and π (from above to below). Markers present numerical results for the plane problem.

Figs. 7.4, 7.5 show the dependencies which can not be obtained within the linear theory and determine the basic characteristics of surface shapes, appearing after occurrence of instability.
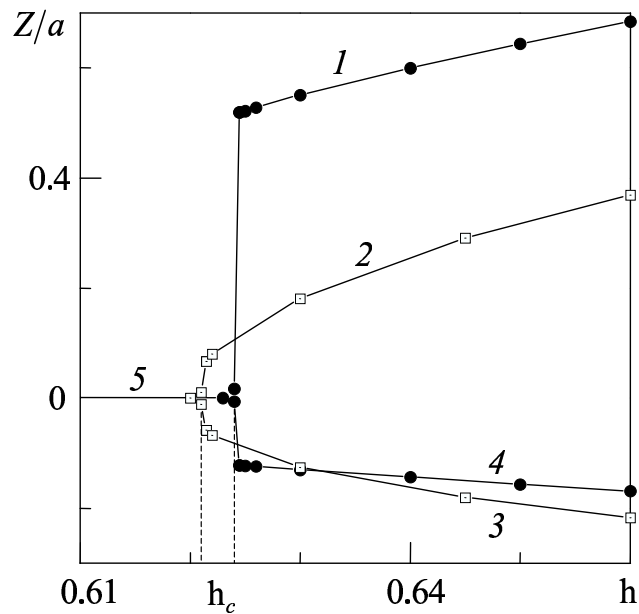

Figure 7.4: Amplitude of the perturbed surface versus the magnetic intensity $h = H_0/H_T$: Vislovich magnetisation law, $\chi = 2.5$, $\lambda = \pi$, Si $= 50$. 1, 2 - peak top coordinate, 3, 4 - peak foot coordinate, 5 - horizontal surface position in the subcritical region $h < h_c$. 1, 4 - axisymmetric problem, 2, 3 - plane problem.

As Fig. 7.4 shows, perturbations of finite amplitude arise on the free surface when magnetic field intensity exceeds its critical value and then their amplitude increases monotonically with the field increasing. The peak top develops more intensively than the peak foot. This distinction is expressed much more for the axially symmetric disturbances (peaks) than for the plane ones (rollers). Under the same conditions the amplitude of the axially symmetric perturbations of the surface (peaks) is significantly greater than that of the plane ones (rollers).

An amplitude of the perturbed surface near the stability threshold is of particular interest. The amplitude dependence on the fluid properties is illustrated in Fig. 7.5. From Fig. 7.5 we see that with the strengthening of magnetic properties of the fluid (with increasing saturation magnetisation M_s) the amplitude of initial surface perturbations increases considerably. Fig. 7.5 illustrates also the well-known experimental fact: if the fluid magnetisation is less than a limiting value (Si < 2 for considered problems) the instability of the fluid surface does not arise at any values of the magnetic field intensity.
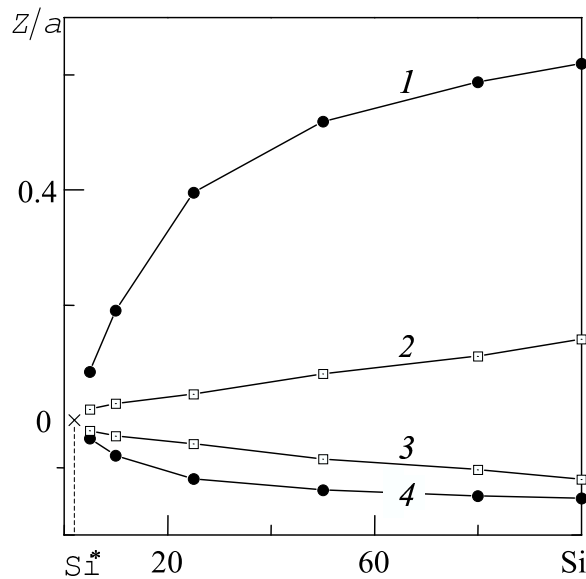

Figure 7.5: Amplitude of the perturbed surface near the stability threshold ($h_c < h < h_c+0.002$) versus the parameter Si: Vislovich magnetisation law, $\chi = 2.5$, $\lambda = \pi$; $h = H_0/H_T$. 1, 2 - peak top coordinate, 3, 4 - peak foot coordinate. 1, 4 - axisymmetric problem, 2, 3 - plane problem. $\mathrm{Si}^* = 2$ is critical value.

Comparison of axisymmetric and three-dimensional numerical results

The numerical study of the problem on equilibrium shapes of the magnetic-fluid layer in a full three-dimensional case with surfaces of the graph type were fulfilled in [46, 47]. A comparison between the numerical results for the axisymmeric and the 3D models were realised in [41]. The choice of the magnetisation law and the correlation between wave lengths of axisymmetric and 3D surface perturbations play an important role for the quantitative comparison of numerical results. The Vislovich's interpolation formula was used in both models. The wave length of the axisymmetric perturbation was specified as $a = \lambda_c/\sqrt{3}$ and not as $a = \lambda_c/2$, defined at the beginning of the Section.

The critical magnetic field, predicted by the axisymmetric and 3D models, nearly coincides, see Fig. 7.6. An axisymmetric surface profile is very close to a 3D profile of a single peak, see Fig. 7.7. The profile shapes of both models nearly completely coincides, but an amplitude of an axisymmetric peak is smaller at around 10 % of those for a 3D peak. The difference appears due to the different geometries of the cell (circular for the axisymmetric model and hexagonal

for the 3D model) and, as a consequence, different volumes of the isolated peak, which should be preserved in both models.
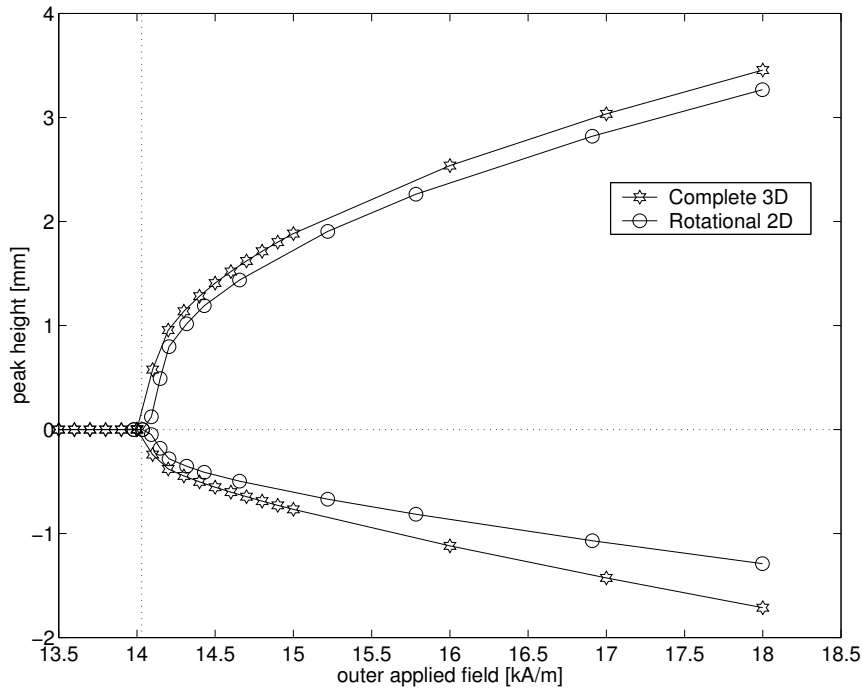

Figure 7.6: Peak height of the perturbed surface versus the magnetic field intensity H_0: Vislovich magnetisatioin law, magnetic fluid EMG 909. The vertical line corresponds a critical magnetic field predicted by the linear stability theory $H_0 = 14.03$ kA/m.
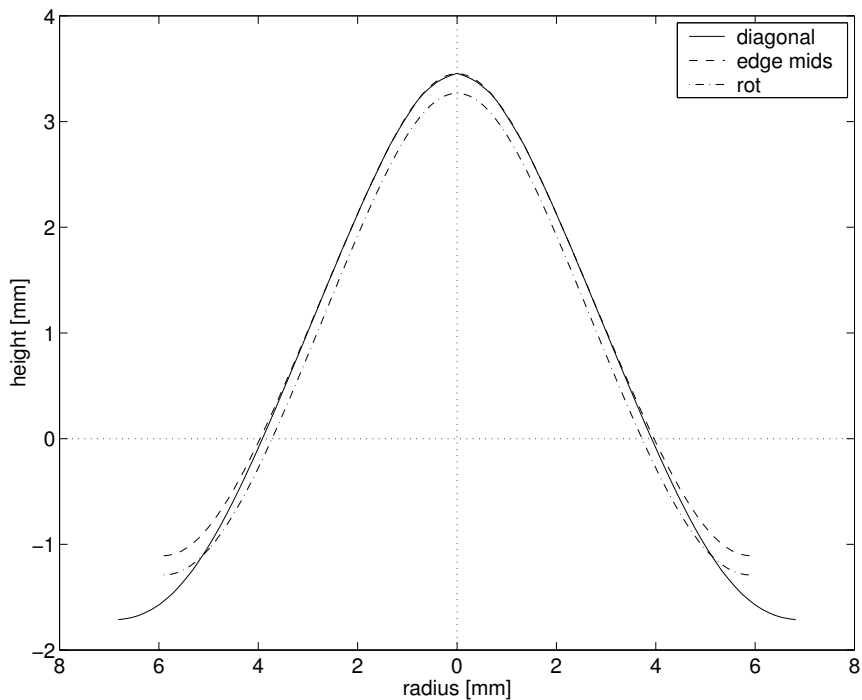

Figure 7.7: Axial sections of a three-dimensional peak along a line, connecting two vertices of the hexagonal base (diagonal) and along a line, connecting midpoints of two opposite edges of the hexagon (edge mids), and an axisymmetric peak shape (rot).

7.4   Solitary surface pattern

A solitary surface pattern (soliton) was recently experimentally uncovered in the bistability interval of the Rosensweig instability, see [61]. A single stationary peak was generated by a local field perturbation in the hysteretic regime of the Rosensweig instability and observed to be stable after turning off the locally applied field. A solitary surface configuration can be interpreted as an additional stable state in the hysteretic regime beside the flat surface and the fully developed pattern, analysed in this Chapter.

Aspects of modeling

In the case of a fully developed pattern we restrict the computational domain to a single cell and specify symmetry boundary conditions at the cell boundaries, see Section 7.1. For resolving a single peak, we consider an enlarged computational domain and use boundary conditions corresponding to a flat surface. It means that the dimensionless form of the governing equations for equilibrium shapes of the magnetic-fluid layer stays without modifications. Namely, they are in the form of equations (7.1)-(7.5) for the field and equations (7.8)-(7.9) for the free surface. The only change now is that the dimensionless parameter $\lambda = a\sqrt{\rho g/\sigma}$ has no connection with the wavelength of the pattern, as it was predefined in Section 7.3. The value of λ should be specified large enough to prevent influence form the "artificial" boundary $r = 1$ to the region where a peak forms. Experimentally in [61] where observed that a shape of a soliton is very similar to a standard Rosensweig spike. Their wavelengths also nearly coincide. For our calculations we define a layer domain which covers a multiple of one wavelength

$$a = k\lambda_c, \quad k = 1, 2, \dots$$

where λ_c is the critical wavelength, estimated by the linear stability analysis, see Section 7.3.

The numerical strategy for solution of the coupled system (7.1)-(7.5), (7.8)-(7.9) was given in Section 7.2. It was mentioned there that results of calculations in the bistability interval of the Rosensweig instability depend strongly on the initial surface deformation Γ^0. A perturbation of a small amplitude results in a flat surface, whereas a strong perturbation produces a stable peak. Our aim now is to resolve an additional stable state in the hysteretic regime, a soliton. In numerical simulations we replace the initial local field perturbation of the experiment in [61] by an initial surface deformation. The deformation is taken in the form of a single peak in a pattern (corresponds $a = \lambda_c/2$) and extended by the surface $z = 0$ to the rest of the computational domain ($a = 2\lambda_c$).

Numerical results

The results of this Section are obtained for the magnetic fluid EMG 901 with the following parameters: $\chi = 2.2$, $\rho = 1406$ kg/m^3, $\sigma = 0.025$ kg/s^2, $M_S = 48$ kA/m. From a linear stability theory, see [63], we get a critical magnetic field $H_c = 9.104$ kA/m, a critical wavelength $\lambda_c = 8.457$ mm and a critical wavenumber $k_c = 0.743$ mm^{-1}.

At first we make calculations for the fully developed pattern to find a hysteretic regime of the Rosensweig instability, where two stable surface configurations exist. We get the bistability interval, see Fig. 7.8,

$$8.59 \pm 0.01 \leq H_0 \leq 9.12 \pm 0.01 \text{ kA/m}.$$

Within this range we resolve single peak configurations on the free surface of the magnetic fluid.

The lower stability boundary, defined numerically, appears for $H^* = 8.59 \pm 0.01$ kA/m. According to the numerical results the soliton exists in the subcritical region $H < H^*$ and reduces to the flat surface at $H = 8.54 \pm 0.01$ kA/m. This observation is in contradiction
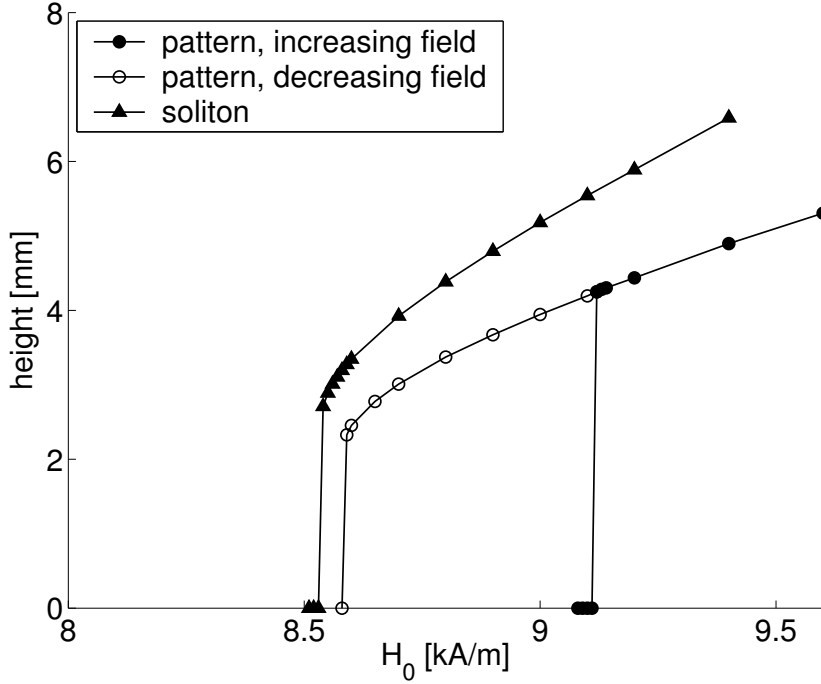
Figure 7.8: Height of the peak in the standard Rosensweig pattern and soliton height versus the applied magnetic field: $a = \lambda_c/2$ for the peak in the pattern and $a = 2\lambda_c$ for the soliton.

with the experiment in [61], where the transition from the soliton to the flat surface was observed for $H > H^*$. No configurations, except the flat surface, were experimentally found in the subcritical region. The contradiction in experimental and numerical results might be based on the assumption of the mathematical model for the peak in the pattern to have a fixed wavelength. In reality the wavelength changes with the field change, see [39]. The approximation $a = \lambda_c/2$ might be unsatisfactory for fields close to H^* and cause thereby quantitative difference between the experimental observations and the numerical results.

According to the experimental observations in [61], in the supercritical region $H_0 > H_c$ a pattern formation prevents a single peak configuration. A sudden transition from the soliton to the fully developed Rosensweig pattern is observed experimentally for the field $H_0 \approx H_c + 0.02$ kA/m, slightly stronger than the critical one. We realised that axisymmetric single peaks exist not only in the hysteretic regime but also for $H_0 > 9.12$ kA/m, see Fig. 7.8. This might be caused by the fact that the axisymmetric model does not allow a developed pattern as a solution of the equations when $a = 2\lambda_c$. In such a big region the developed pattern is not axisymmetric. Axial symmetry for the pattern can be assumed only in the case when the horizontal size of the computational domain matches the critical wavelength λ_c, i.e. $a \approx \lambda_c/2$. The developed pattern in the supercritical region might be energetically favourable and soliton configurations present an unstable state of the Rosensweig instability for $H_0 > H_c$.

Fig. 7.9 displays soliton shapes for different values of the applied magnetic field. A stronger intensity of the magnetic field results in a higher peak amplitude and a deeper circular hollow around a peak.

Fig. 7.10 shows, how the "artificially" vertical boundary of the computational domain $r = a$, where the surface flatness is specified by condition (7.3), influences to the soliton shaping. At the left picture of Fig. 7.10 a profile for $a = 0.5\lambda_c$ presents a peak in the pattern with a prespecified wavelength λ_c. All others shapes are solitons, calculated for different values of the domain size a. The results of calculations show that soliton shapes are very similar to the
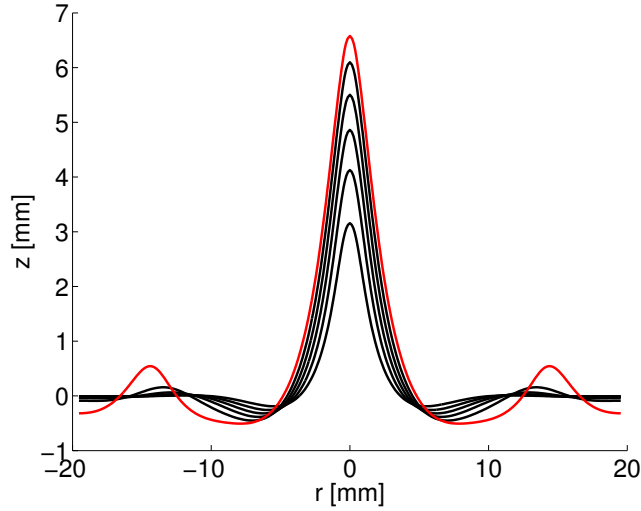
Figure 7.9: Soliton shapes: H_0={8.6, 8.8, 9, 9.2, 9.4, 9.6} kA/m, $a = 2\lambda_c$.

profile of the developed peak in the pattern. A vertical shift of shapes is due to the conservation of the fluid volume and as a consequence a higher soliton amplitude than those of the peak in the pattern. The left picture of Fig. 7.10 shows that for the applied field $H_0 = 9$ kA/m soliton shapes for $a = \{\lambda_c, 2\lambda_c, 2.5\lambda_c\}$ are very close to each other. The choice of the layer domain with $a = 2\lambda_c$ seems to be reasonable for soliton calculations. The right picture of Fig. 7.10 shows, however, that for $H = 9.6$ kA/m defining $a = 2\lambda_c$ results in a circular wave around a soliton. The wave appears due to the symmetry boundary condition at $r = a$ and vanishes when the vertical boundary of the domain is set far enough from the peak region.
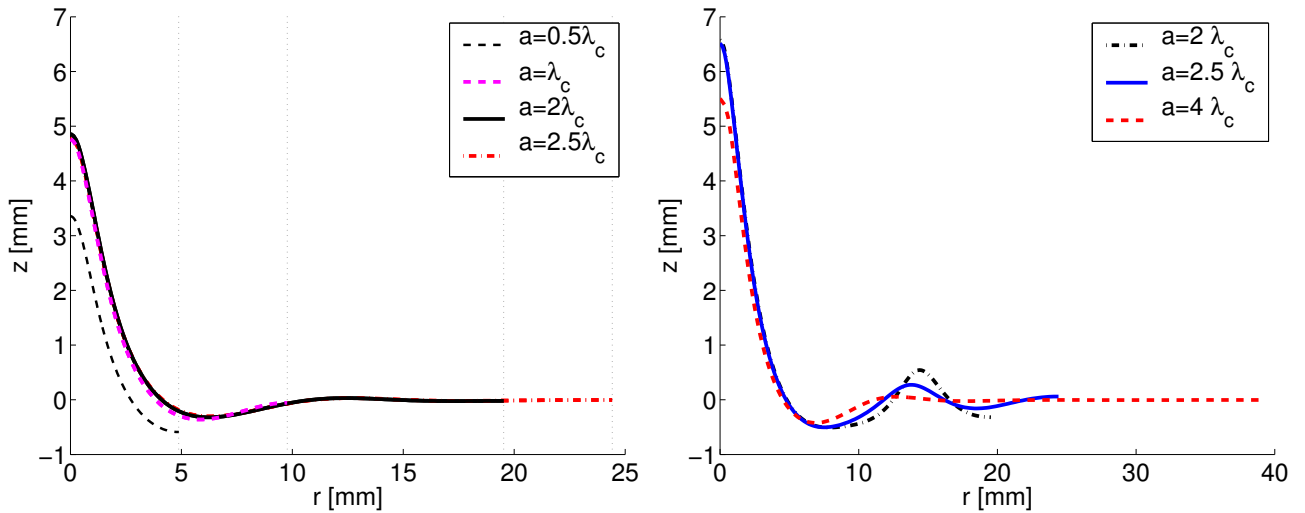

Figure 7.10: Soliton profiles for the different domain size a: $H_0 = 9$ kA/m (left) and $H_0 = 9.6$ kA/m (right).

Let us name a diameter of a peak's foot as a peak's wavelength. Figure 7.11 shows wavenumber of solitons versus the applied magnetic field. The deviation of the soliton wavenumber from the pattern wavenumber k_c, predicted by the linear stability analysis, (dashed line in Fig. 7.11) is more than 30 %. The numerical results in Fig. 7.11 predict monotonical decrease of the wavenumber with increasing field intensity and shows near linear dependence of the wavenumber from the field.
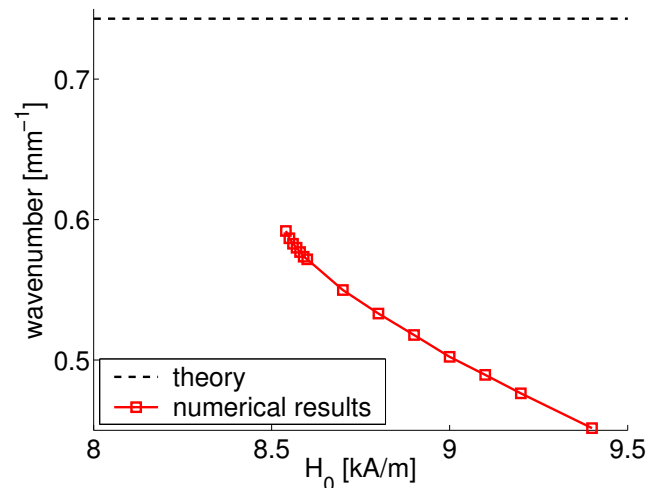
Figure 7.11: Wavenumber of solitons versus the applied magnetic field: $a = 2\lambda_c$.

Chapter 8

Final Remarks

A major goal of the thesis was to develop a numerical solution strategy for calculating axisymmetric equilibrium magnetic-fluid shapes subjected to a uniform applied magnetic field. The second important subject of the thesis was on the base of the developed numerical strategy to fulfil an accurate numerical modeling and simulation of problems on magnetic-fluid drop shapes, bubble configurations in a bulk of the magnetic fluid and on single peak formations on the surface of a magnetic-fluid layer.

The mathematical model on equilibrium magnetic-fluid shapes is formulated by a coupled system of Maxwell's equations inside the fluid and in the surrounding air and the Young-Laplace equation on the free surface boundary. A fluid-air interface is unknown a-priori and is defined by the magnetic field. A simultaneous solution of the equations is necessary. An iterative decoupling strategy allows to split equations into two subproblems: the Maxwell's equations for the given fluid-air interface and the Young-Laplace equation for the given magnetic field. For the approximation of the separated subproblems different numerical techniques were used.

A coupled strategy of boundary-element and finite-element methods is a powerful tool for the numerical treatment of the Maxwell's equations. A boundary element method was used in an unbounded air domain to fulfil the boundary condition for the magnetic field at infinity while with a finite element method we resolved the non-linearity of the magnetostatic equations inside a magnetic fluid. A direct formulation of boundary integral equations with their further discretisation by the collocation technique is a possible way to handle the Laplace equation. The numerical convergence of the piecewise-constant collocation boundary-element method with the exact boundary representation, its piecewise linear and cubic spline approximations were analysed. In numerical tests cubic splines have been proven to be sufficiently accurate for the boundary representation. The results for the exact boundary and for its cubic spline approximation nearly coincide. The coupling of the collocation boundary element method in the exterior air domain and the Galerkin finite element method in the interior fluid domain was realised. Piecewise linears for the potential approximation and piecewise constants for the normal derivative of the potential on the free boundary were taken. The numerical convergence of the second order for r-weighted L^2-norm was shown for the magnetostatic problem on a sphere. From the calculations we found that the boundary element discretisation of the axisymmetric Laplace equation shows a non-smooth behaviour of the discretisation error near the symmetry axis. We realised that the finite element method does not exhibit the same sensitive behaviour of the numerical solution.

An application of finite element methods requires a grid construction in a computational domain. Two methods for the grid generation, a harmonic extension approach and a Delaunay technique, were presented. They were compared with respect to the quality of the generated grids and the computational efficiency of the underlying algorithms in application to the coupled

magnetostatic and free surface problem. We found that the Delaunay approach allows to construct triangulations of a better quality compared to the harmonic extension approach. This fact can be essential for the iterative solving of the coupled equations, when the change of the computational domain during the iterative process is rather strong.

Surface shapes were parametrised with respect to the arc length. The parametric representation of the free surface results in the reformulation of the Young-Laplace equation as a system of nonlinear ordinary differential equations. The finite-difference method and the spline scheme can be applied for the discretisation of the resulting system. A test example was realised to examine the influence of a successive under-relaxation technique to the stability of the iterative algorithms for solving algebraic equations. The spline scheme showed a better stability property than the finite-difference method. We found that for axisymmetric problems at least one boundary condition should necessarily be specified at the "non-axis" end point. Otherwise, the scheme shows no convergence at all. A special algorithm of the surface grid generation was presented. It is based on the information about a surface curvature and allows to produce an accurate approximation for the shapes with high deformations.

The numerical results for the problem on axisymmetric equilibrium surface shapes of a magnetic-fluid drop under the influence of an external uniform magnetic field were presented. A comparison of numerical results with spheroidal equilibrium shapes, predicted theoretically by the energy minimisation technique, was given. Equilibrium shapes with pointed ends were resolved numerically, resulting in the strong deviation from spheroidal shapes of the theory. The transition from shapes with rounded ends to shapes close to conical were realised numerically. Equilibrium drop shapes were resolved in a wide range of field intensities till the saturation of magnetic fluids. The drop elongates monotonically under increasing field with tendency to take unchangeable configuration in the region of fluid saturation. Shapes, close to conical, appear after the first turning point of the hysteretic curve for the increasing magnetic field and preserve their acute configuration till the second turning point for the decreasing field. Increase in the applied field results in decrease of the cone angle.

The numerical results for the problem on axisymmetric equilibrium surface shape of a bubble inside a magnetic-fluid layer under the influence of a uniform magnetic field were presented. The behavior of magnetic-fluid drops and bubbles in the magnetic fluid were compared.

Under the assumption of axial symmetry, equilibrium states of the magnetic-fluid layer in the Rosensweig-instability phenomenon were numerically resolved. The numerically-obtained critical values of the magnetic field, when the transition from the flat surface to the pattern of peaks appears, found to be in agreement with the theoretically-predicted field values obtained by the linear stability analysis. Equilibrium surfaces were calculated for different magnetic intensities and magnetic-fluid parameters. A comparison of axisymmetric and three-dimensional numerical results were discussed. The quantitative comparison of axisymmetric and three-dimensional surface profiles justifies the axial symmetry assumption for a peak in the pattern.

A solitary surface pattern (soliton) was recently experimentally uncovered in the bistability interval of the Rosensweig instability. The numerical treatment of the Rosensweig-instability phenomenon allowed us to resolve soliton configurations as an additional stable state beside the flat surface and the fully developed pattern.

Bibliography

[1] M. Abramowitz and I. A. Stegun, *Handbook of mathematical functions*. Dover, New York, 1965.

[2] R. A. Adams, *Sobolev spaces*. Academic Press, London, 1978.

[3] J. H. Ahlberg, E. N. Nilson, J. L. Walsh, *The theory of splines and their applications*. Academic Press, New York, 1967.

[4] D. A. Anderson, J. C. Tannehil and R. H. Pletcher, *Computational fluid mechanics and heat transfer*. Hemisphere Publishing Corp., New York, 1984.

[5] V. I. Arkhipenko, Yu. D. Barkov and V. G. Bashtovoi, Study of a magnetized fluid drop shape in a homogeneous magnetic field, *Magn. Gidrodin.* 3 (1978), 131-134, in Russian; *Magnetohydrodynamics* 14 (3) (1978), 373-375.

[6] D. N. Arnold and W. L. Wendland, On the asymptotic convergence of collocation methods, *Math. Comp.*, 41 (1983), 349-381.

[7] D. N. Arnold and W. L. Wendland, The convergence of spline collocation for strongly elliptic equations on curves, *Numer. Math.*, 47 (1985), 317-341.

[8] J. C. Bacri and D. Salin, Instability of ferrofluid magnetic drops under magnetic field, *J. Phys. Lett.*, 43 (1982), 649-654.

[9] O. A. Basaran and F. K. Wohlhuter, Effect of nonlinear polarization on shapes and stability of pendant and sessile drops in an electric (magnetic) field, *J. Fluid Mech.*, vol. 244 (1992), 1-16.

[10] V. G. Bashtovoi, S. G. Pogirnitskaya and A. G. Reks, Determination of the shape of a free drop of magnetic fluid in a uniform magnetic field, *Magn. Gidrodin.*, 3 (1987), 23-26.

[11] V. G. Bashtovoi, O. A. Lavrova and V. K. Polevikov, Numerical modeling of stability of a horizontal magnetic-fluid layer, in Novel Smart Materials - Electro- and Magneto-Sensitive Fluids for Energy-Effective Technologies. Proceedings of the International Conference and Workshop, Minsk Sept. 11-13 2001, 33-40. In Russian.

[12] V. G. Bashtovoi, O. A. Lavrova, V. K. Polevikov and L. Tobiska, Computer modeling of the instability of a horizontal magnetic-fluid layer in a uniform magnetic field, *JMMM*, 252 (2002), 299-301.

[13] B. M. Berkovsky, V. K. Polevikov, *Computational experiment in convection*. Universitetskoe, Minsk, 1988. In Russian.

[14] B. Berkovsky, V. Medvedev and M. Krakov, *Magnetic fluids: engineering applications.* Oxford University Press, Oxford, 1993.

[15] B. Berkovski and V. Bashtovoy, ed. *Magnetic fluids and applications handbook.* Begell house, New York, 1996.

[16] C. Bernardi, M. Dauge, Y. Maday, Spectral methods for axisymmetric domains, in *Series in Applied Mathematics* ed. by P. G. Ciarlet and P.-L. Lions. Gauthier-Villars, Paris, 1999.

[17] E. Blums, A. Cebers and M. Maiorov, *Magnetic fluids.* De Gruyter, Berlin, 1997.

[18] J.P. Brancher and D. Zouaoui, Equilibrium of a magnetic liquid drop, *JMMM*, vol. 65 (1987), 311-314.

[19] C. A. Brebbia, J. C. F. Telles and L. C. Wrobel, *Boundary element techniques: theory and application in engineering.* Springer-Verlag, Berlin, 1984.

[20] A. M. Budnik and V. K. Polevikov, Numerical study of equilibrium forms of magnetic fluid including magnetic field disturbances, *JMMM*, 65 (1987), 335-338.

[21] J. E. Castillo, ed., *Mathematical aspects of numerical grid generation.* No. 8 in Frontier in Applied Mathematics, Society for Industrial and Applied Mathematics (SIAM), Philadelphia, PA, 1991.

[22] G. Chen and J. Zhou, *Boundary element methods.* Academic Press, London, 1992.

[23] P. Ciarlet, *The finite element method for elliptic problems.* North-Holland, Amsterdam, 1978.

[24] M. Cowley and R. Rosensweig, The interfacial stability of a ferromagnetic fluid, *J. Fluid Mech.*, 30 (1967), 671-688.

[25] H. B. Dwight, *Tables of integrals and other mathematical data.* Macmillan, New York, 1961.

[26] M. Feistauer, V. Sobotíková, Finite element approximation of nonlinear elliptic problems with discontinuous coefficients, *Modél. Math. Anal. Numér.* 24 (1990), 457-500.

[27] A. Gailitis, Formation of the hexagonal pattern on the surface of a ferromagnetic fluid in an applied magnetic field, *J. Fluid Mech.*, 82 (1977), 401-413.

[28] R. Friedrichs and A. Engel, Pattern and wavenumber selection in magnetic fluids, *Phys. Rev. E*, 64 (2001), 021406-021419.

[29] W. Hackbusch, *Multi-grid methods and applications.* Springer-Verlag, Berlin, 1985.

[30] W. Hackbusch, *Elliptic differential equations: theory and numerical treatment.* Springer-Verlag, Berlin, 1992.

[31] W. Hackbusch, *Integral equations: theory and numerical treatment.* Birkhauser, Basel, 1995.

[32] T. Iliescu, V. John, W. J. Layton, G. Matthies and L. Tobiska, A numerical study of a class of LES models, *Int. J. Comput. Fluid Dyn.*, 17(1) (2003), 75-85.

[33] V. John and G. Matthies, Higher order finite element discretizations in a benchmark problem for incompressible flows, *Int. J. Num. Meth. Fluids*, 37 (2001), 885-903.

[34] V. John, Higher order finite element methods and multigrid solvers in a benchmark problem for the 3D Navier Stokes equations, *Int. J. Num. Meth. Fluids*, 40 (2002), 775-798.

[35] V. John, *Large Eddy Simulation of Turbulent Incompressible Flows. Analytical and Numerical Results for a Class of LES Models.* Lecture Notes in Computational Science and Engineering 34. Springer-Verlag, Berlin, 2003.

[36] V. John and G. Matthies, MooNMD - a program package based on mapped finite element methods, *Comput. Visual. Sci.*, 6 (2004), 163-170.

[37] A. Kufner, A-M. Sändig, *Some applications of weighted Sobolev spaces.* Taubner, Leipzig, 1987.

[38] L. D. Landau and E. M. Lifshitz, *Electrodynamics of continuous media (Course of theoretical physics; Vol. 8).*

[39] A. Lange, B. Riemann and R. Richter, Wave number of maximal growth in viscous ferrofluids, *Magnetohydrodynamics*, 37 (3) (2001), 261-267.

[40] O. A. Lavrova and V. K. Polevikov, Numerical study od stability of a plane magnetic-fluid layer in an orthogonal magnetic field, *Materials 57th Student Scientific Conference*, Minsk, Belarusian State University (2000), 191-195. In Russian.

[41] O. Lavrova, G. Matthies, T. Mitkova, V. Polevikov and L. Tobiska, Finite element methods for coupled problems in ferrohydrodynamics, Vol. 35 in Lecture Notes in Computational Science and Engineering, Challenges in Scientific Computing - CISC 2002. Springer-Verlag, Berlin, 2003.

[42] O. Lavrova, G. Matthies, V. Polevikov and L. Tobiska, Numerical modeling of the equilibrium shapes of a ferrofluid drop in an external magnetic field, *PAMM Proc. Appl. Math. Mech*, 4(1) (2004), 704-705.

[43] O. Lavrova, V. Polevikov and L. Tobiska, Equilibrium shapes of a ferrofluid drop, *PAMM Proc. Appl. Math. Mech*, (2005), accepted for publication.

[44] H. Li, T. C. Halsey and A. Lobkovsky, Singular shape of a fluid drop in an electric or magnetic field, *Europhys. Lett.*, 27 (1994), 575-580.

[45] V. Liseikin, *Grid generation.* Springer-Verlag, Berlin, 1999.

[46] G. Matthies, *Finite element methods for free boundary value problems with capillary surfaces.* Shaker Verlag, Aachen, 2002. PhD thesis, Fakultät für Mathematik, Otto-von-Guericke-Universität Magdeburg.

[47] G. Matthies and L. Tobiska, Numerical simulation of normal-field instability in the static and dynamic case, *JMMM*, 289 (2005), 346-349.

[48] M. J. Miksis, Shape of a drop in an electric field, *Phys. Fluids*, 24 (1982), 1967-1972.

[49] T. Mitkova, *Solvability and finite element approximation of a flow model in magnetic fluid rotary shaft seals.* PhD thesis, Fakultät für Mathematik, Otto-von-Guericke-Universität Magdeburg, 2004.

[50] Q. Nie and G. Baker, Application of adaptive quadrature to axi-symmetric vortex sheet motion, *Journal of computational physics*, 143(1) (1997), 49.

[51] R. Piessens, E. de Doncker-Kapenga, C. W. Uberhuber and D. K. Kahaner, *Quadpack: a subroutine package for automatic integration*. Springer-Verlag, Berlin, 1983.

[52] V. K. Polevikov, Application of the relaxation method to solve steady difference problems of convection, *U.S.S.R. Comput. Maths. Math. Phys.*, 21(1) (1981), 126-137; translation from *Zhurnal vychislitelnoy matematiki i matematicheskoy fiziki*, 21(1) (1981) 127-138.

[53] V. K. Polevikov and V. M. Denisenko, Numerical study of equilibrium shapes of a drop rotating in gravitational field, *Vestn. Beloruss. Gos. Univ., Ser1, Fiz. Mat. Mech.*, 2 (1985), 37-41. In Russian.

[54] V. K. Polevikov, Application of adaptive grids to calculate the free surface in problems on statics of a magnetic fluid, *Differents. Uravneniya*, 30(12) (1994), 2146-2152.

[55] V. K. Polevikov, Stability of a static magnetic-fluid seal under the action of an external pressure drop, *Fluid Dyn.*, 32(3) (1997), 1973-1978; translation from *Izv. Akad. Nauk, Mekh. Zidk. Gaza*, 2 (1994), 2146-2152.

[56] V. K. Polevikov, *Numerical modelling of equilibrium capillary surfaces: some methods and results*. Preprint 98-10, Otto-von-Guericke-University Magdeburg, 1998.

[57] V. K. Polevikov, Methods for numerical modeling of equilibrium capillary surfaces, *Differ. Equations*, 35(7) (1999), 985-991; translation from *Differ. Uravn.*, 35(7) (1999), 975-981.

[58] V. K. Polevikov, Methods for numerical modeling of two-dimensional capillary surfaces, *Comput. Methods in Applied Math.*, 4(1) (2004), 66-93.

[59] A. Quarteroni, R. Sacco and F. Saleri, *Numerical mathematics*. Springer-Verlag, New York, 2000.

[60] A. Ramos, A. Castellanos, Conical points in liquid-liquid interfaces subjected to electric fields, *Physics Letters A*, 184 (1994), 268-272.

[61] R. Richter and I. Barashenkov, Two-dimensional solitons on the surface of magnetic fluids, *Phys. Rev. Lett.* 94 (2005), 184503-184506.

[62] G. O. Roberts, Computational meshes for boundary layer problems, Vol. 8 in Lecture Notes in Phycsics, Proc. Second Int Conf. Num. Methods Fluid Dyn. Springer-Verlag, New York, 1971.

[63] R. E. Rosensweig, *Ferrohydrodynamics*. Dover Pubns, 1998.

[64] Y. Saad, *Iterative methods for sparse linear systems*. PWS Publ., Boston, 1996.

[65] J. Saranen and W. L. Wendland, On the asymptotic convergence of collocation methods with spline functions of even degree, *Math. Comp.*, 45 (1985), 91-108.

[66] O. E. Sero-Guillaume, D. Zouaoui, D. Bernandin and J. P. Brancher, The shape of a magnetic liquid drop, *J. Fluid Mech.*, 241 (1992), 215-232.

[67] J. D. Sherwood, Breakup of fluid droplets in electric and magnetic fields, *J. Fluid Mech.*, 188 (1988), 133-146.

[68] J. R. Shewchuk, Triangle: engineering a 2D quality mesh generator and Delaunay triangulator, Vol. 1148 in Lecture Notes in Computer Science, *Applied computational geometry: towards geometric engineering*, selected papers / FCRC'96 workshop, WACG'96, Philadelphia, PA, May 27-28, 1996. Springer-Verlag, Berlin, 1996.

[69] H. A. Stone, J. R. Lister, M. P. Brenner, Drops with conical ends in electric and magnetic fields, *Proc. R. Soc. Lond. A*, 455 (1999), 329-347.

[70] A. H. Stroud and D. Secrest, *Gaussian quadrature formulas.* Prentice-Hall, New York, 1966.

[71] G. I. Taylor, Disintegration of water drops in an electric field, *Proc. R. Soc. A*, 280 (1964), 383-397.

[72] A. O. Tsebers, Virial method of investigation of statics and dynamics of magnetizable liquids, *Magnitnaya Gidrodinamika*, 21, 1 (1985), 25-34.

[73] A. N. Vislovich, Phenomenological equation of static magnetization of magnetic fluids, *Magnetohydrodynamics*, 2 (1990), 178-183.

[74] A. N. Vislovich and V. K. Polevikov, Effect of the centrifugal and capillary forces on the free surface shape of a magnetic liquid seal, *Magnetohydrodynamics*, 30(1) (1994), 67-74; translation from *Magn. Gidrodin.*, 1 (1994), 77-86.

[75] A. N. Vislovich and V. K. Polevikov, Concerning numerical simulation of the failure of a magnetic-fluid seal with a rotary outer profiled cylinder, *J. Eng. Phys. Thermophys.*, 70(1) (1997), 107-112; translation from *Inzh.-Fiz. Zh.*, 70(1) (1997), 105-110.

[76] W. L. Wendland, On some mathematical aspects of boundary element methods for elliptic problems, in *The mathematics of finite elements and applications V: MAFELAP 1984* ed. by J. R. Whiteman. Academic Press, London, 1985.

[77] W. L. Wendland, Asymptotic accuracy and convergence for point collocation methods, in *Topics in boundary element research, Vol.2* ed. by C. A. Brebbia. Springer-Verlag, Berlin, 1985.

[78] W. L. Wendland, On asymptotic error estimates for combined BEM and FEM, in *Finite element and boundary element techniques from mathematical and engineering point of view* ed. by E. Stein. Springer-Verlag, Wien, 1988, 273-333.

[79] F. K. Wohlhuter and O. A. Basaran, Shapes and stability of pendant and sessile dielectric drops in an electric field, *J. Fluid Mech.*, vol. 235 (1992), 481-510.

[80] L. C. Wrobel, *The boundary element method. Applications in thermo-fluids and acoustics.* Wiley, Chichester, 2002.

[81] A. Ženíšek, The finite element method for nonlinear elliptic equations with discontinuous coefficients, *Numer. Math.* 58 (1990), 51-77.

Lebenslauf

Olga Lavrova

geboren am 24.04.1979 in Minsk (Belarus)

09\1986-06\1996	Schule in Minsk
09\1996-07\2001	Studium an der Belarusische Staatliche Universität, Fakultät für angewandte Mathematik und Informatik, Minsk
2001	Diplom in Mathematik
10\2001-07\2002	Graduiertenstipendium an der Belarusische Staatliche Universität, Fakultät für angewandte Mathematik und Informatik, Institut für numerische Mathematik, Minsk
07\2002-12\2004	Graduiertenstipendium an der Otto-von-Guericke Universität, Fakultät für Mathematik, Institut für Analysis und Numerik, Magdeburg
seit 01\2005	Wissenschaftliche Mitarbeiterin am Projekt des DFG-SPP 1104 an der Otto-von-Guericke Universität, Fakultät für Mathematik, Institut für Analysis und Numerik, Magdeburg